Phonon hydrodynamic transport at elevated temperature

by

Zhiwei DING

B. Eng. National University of Singapore (2014)

Submitted to the Department of Materials Science and Engineering

in partial fulfillment of the requirements for the degree of

Doctor of Philosophy in Materials Science and Engineering

at the

MASSACHUSETTS INSTITUTE OF TECHNOLOGY

June 2021

Author ……..……..……..……..…….
Department of Materials Science and Engineering
May 24, 2021

Certified by ..……..……..……..……...
Keith Nelson
Haslam and Dewey Professor of Chemistry
Thesis Advisor

Certified by ..……..……..……..……...
Ju Li
Professor of Materials Science and Engineering
Thesis co-Advisor

Accepted by ……..……..……..……
Frances M. Ross
Chair, Departmental Committee on Graduate Studies

Phonon hydrodynamic transport at elevated temperature

by

Zhiwei DING

Submitted to the Department of Materials Science and Engineering
on May 7, 2021, in partial fulfillment of
the requirements for the degree of
Doctor of Philosophy in Materials Science and Engineering

Abstract

For over half a century, phonon hydrodynamic transport was deemed exotic and mattered only at extremely low temperatures. In this work, by combining the theoretical and experimental approach, we successfully predict and confirm the existence of phonon hydrodynamic transport in graphite above 200 K. More specifically, we introduce a direction-dependent definition of normal and Umklapp scattering, which gives an improved description of mode-specific phonon dynamics. By extending the classical Fuchs-Sondheimer solution, we developed a first-principles framework to study phonon hydrodynamics under the size effect with mode-by-mode phonon scattering details. We unambiguously revealed the Poiseuille heat flow by studying the variation of heat flow as the graphite ribbon width and identified for the first time the existence of phonon Knudsen minimum – an unusual phenomenon unique to hydrodynamic regime – which can be observed up to 90 K. Using a sub-picosecond transient grating technique, we directly observed second sound in graphite at record-high temperatures of 200 K. With the enlarged grating-period window, we firstly reported the dispersion of thermal wave, whose velocity increases with decreasing grating period. Our experimental findings are well explained with the interplay among "three fluids": ballistic, diffusive, and hydrodynamic phonons. We believe our study may stimulate further work into discovering more material systems possessing significant phonon hydrodynamic features, as well

as new research into understanding and manipulating the phonon transport in the hydrodynamic scheme.

Thesis Supervisor: Keith Nelson
Title: Haslam and Dewey Professor of Chemistry

Acknowledgements

I would sincerely thank my advisors, Prof. Gang Chen, Prof. Keith Nelson, and Prof. Ju li. Their scientific rigor and curiosity deeply impressed and excite me. I thank my committee members, Prof. Jeffrey Grossman and Prof. Elsa A. Olivetti for their critical insights in my thesis work. I want to thanks all my group members especially Jiawei Zhou, Ke Chen, Bai Song, Mingda Li, Te-huan Liu and Qichen Song, who has helped me a lot during my PhD studies and daily life. I would sincerely thanks Alexei Maznev, Samuel Cole Huberman and Vazrik Chiloyan. I benefit a lot from the collaboration with them. I would like to thanks my parents for their constant support and encouragement. I want to thanks all my friends who share painful and happy moments together during journey of PhD study.

Table of Contents

List of Figures

Chapter 1 Introduction

1.1 Phonon hydrodynamic transport

Phonon hydrodynamic transport is regime where phonons behaves like fluid molecules. Phonons are the majors heat carrier in non-metallic solids, whose transport is usually described by the Fourier laws:

$$J = -\kappa \nabla T \tag{1-1}$$

Where J is the heat flux, κ is the thermal conductivity and ∇T is the temperature gradient.

Similarly, molecular flow at the macroscale can be described by the Euler's equation:

$$\frac{d(\rho \mathbf{u})}{dt} = -\nabla \mathrm{p} \tag{1-2}$$

Where ρ and **u** are the density and velocity of the fluid element respectively, and p is the pressure.

Eq. (1-1) and (1-2) indicate that the thermoelectric driving force for heat and molecular flow are temperature and pressure gradient respective. Moreover, Eq. (1-1) predicts, a constant heat flux for a given temperature gradient, indicating an intrinsic damping in heat flow. However, Eq. (1-2) shows the acceleration of molecular under the pressure gradient without any damping effect.

The different behaviors of the damping in the phonons and molecular flows is dues to the interactions/scattering between them is different. More specifically, momentum is always conserved in the molecule-molecule collision process, while the phonon-phonon scattering process are not always momentum conserved. As suggested by Peierls[1], phonon-phonon scattering processes consist of momentum-conserving scattering and momentum-destroying scattering. As shown in Figure 1-1, if the wavevector of the newly-formed phonon is within the 1st Brillion zone (BZ) as shown in this picture, then it is a momentum conserving process called normal scattering

(N-scattering). If it is outside of the first BZ, momentum if not conserved, and it is called Umklapp scattering (U-scattering). Though not rigorous, it is generally accepted that U-scattering is the origin of thermal resistance. Intuitively, if N-scattering dominates, then phonon flow, will behave similar to fluid flow. However, in most materials, at room temperature, it is actually U-scattering is much stronger, leading to the large damping effect in solid materials. Further discussion on this analysis is provided in Chapter 2.

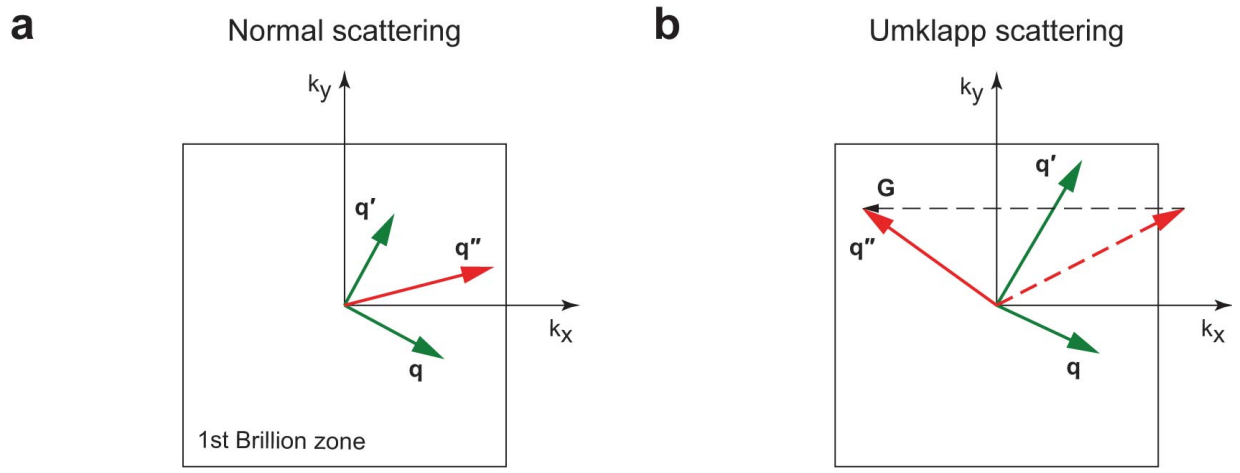

Figure 1-1 Schematic illustration of normal scattering (**N**-scattering) and Umklapp scattering (**U**-scattering) processes, as conventionally defined. (a) **N**-scattering, (b) **U**-scattering.

One unique feature of the phonon hydrodynamic transport is the collective motion. As in the case of the fluid flow, all the molecules share the same drift velocity. The equilibrium distribution of phonons with strong N-scattering rate is the displaced Bose-Einstein distribution:

$$f_d = \frac{1}{\exp\left[\frac{\hbar(\omega - \mathbf{q}\cdot\mathbf{u})}{k_b T}\right] - 1} \tag{1-3}$$

Where $\hbar$, ω, $\mathbf{q}$, k_B and T denote the reduced Planck constant, phonon frequency, phonon wavevector, the Boltzmann constant, and temperature, respectively. $\mathbf{u}$ is constant for all phonon modes in the hydrodynamic regime.

Associated with the drift motion of phonons, there are three signature transport phenomena that are unique to hydrodynamic regimes: phonon Poiseuille flow (Figure 1-2a) and phonon Knudsen Minimum and second sound (Figure 1-2c), which are analogous to Poiseuille flow Knudsen Minimum and ordinary sound in a fluid respectively. For an infinity long sample under a steady temperature gradient, the heat flux is uniform in the diffusive regime (Figure 1-2b), while heat flux is gradually decrease from the center to boundary in the hydrodynamic regime. The difference lies in the source of thermal resistance. In the diffuse regime, the dominating thermal resistance is the phonon-phonon scattering occurring everywhere. However, the diffusive boundary scattering accounting for major thermal resistance in Poiseuille flow. Base on the source thermal resistance, we could deduce geometric condition for Poiseuille flow to occur. Intuitively, the width of the sample need be greater than the mean free path of the N scattering, but smaller than mean free path of the R-scattering (including U-scattering and E-scattering). A detailed analysis is provided in Chapter 3. The conclusion here is that there is a requirement in the width of the sample, and the size of the allowed window depends on the difference between N-scattering and R-scattering rates. In addition, due to the difference in the origin of resistance, distinguished size and temperature dependence is expected for the hydrodynamic regime. More specifically, a superlinear width dependent and larger temperature dependent thermal conductivity is expected in the hydrodynamic regime. As the ribbon width keeps decreasing, phonon transport eventually transitions from the hydrodynamic to the ballistic regime, where N-scattering suppress the thermal conductivity. A sublinear width dependent thermal conductivity is expected in this regime. Combined together, the existence of both a sublinear and a superlinear width-dependent thermal conductivity dictates the existence of a phonon Knudsen minimum. Second sound refers to the propagation of a temperature wave (or phonon density wave) provoked by a heat pulse, analogous to pressure wave propagation in a fluid. In the diffusive regime, the temperature wave will be damped by the momentum destroying R-scattering. (Figure 1-2d). In the hydrodynamic regime, the pulse could be transmitted by many N-scatterings. (Figure 1-2c).

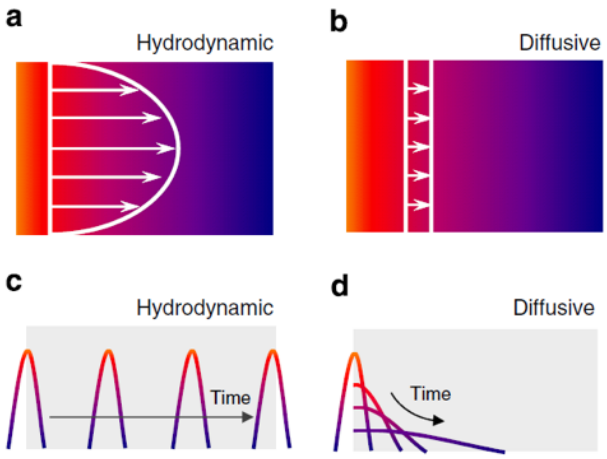

Figure 1-2 (a,b) The steady-state heat flux profiles in hydrodynamic and ballistic regimes, respectively, under a temperature gradient. (c,d) The propagation of a heat pulse in the hydrodynamic and diffusive regimes, respectively. Figures are adapted from Fig. 1 in [2]

1.2 Boltzman transport theory

Boltzman transport theory is a powerful tool to study weakly-interacting[3], and it describes the time evolution of the distribution functions:

$$\frac{\partial f}{\partial t} + \mathbf{v}_g \cdot \nabla f = \left(\frac{\partial f}{\partial t}\right)_c \tag{1-4}$$

where $f(\mathbf{r}, t, \mathbf{q})$ is the phonon distribution function, which is the number of phonons at position $\mathbf{r}$, at time t, with wavevector $\mathbf{q}$ per unit solid angle, per unit wave number interval, per unit volume. $\mathbf{v}_g$ and $\mathbf{q}$ are the phonon group velocity and wavevector respectively. Eq. (1-4) indicates that phonon distribution could change due to phonon convection in the real space. The collision term on the right-hand side of the equation denotes the change in the phonon distribution function due to collisions between phonons. In general, the collision term is a function of all the phonon distribution functions, as a result, solving BTE is usually a not trivial problem.

Under the relaxation time approximation (RTA), one can approximate the collision terms as:

$$\left(\frac{\partial f}{\partial t}\right)_c = -\frac{f - f_o}{\tau} \tag{1-5}$$

Where $f_o = \frac{1}{\exp\left(\frac{\hbar\omega}{k_b T}\right)-1}$ is the equilibrium Bose-Einstein distribution function. RTA much simplified the problem and make the BTE easily solvable and demonstrate certain predictive power in thermal conductivity calculation[4–6]. However, treating all the phonon scattering processes as U-scattering, the RTA significantly underestimates the thermal conductivity when strong N-scattering is present[7]. Moreover, it cannot be used to study phonon hydrodynamic transport, where N-scattering process plays critical roles.

To correct for this discrepancy, Callaway proposed a new model to separate the effects of N-scattering and U-scattering on the heat transport[8], and write the collision term as:

$$\left(\frac{\partial f}{\partial t}\right)_c = -\frac{f - f_o}{\tau_U} - \frac{f - f_d}{\tau_N} \tag{1-6}$$

Where $f_d = \frac{1}{\exp\left[\frac{\hbar(\omega - \mathbf{q}\cdot\mathbf{u})}{k_b T}\right]-1}$ is the displaced Bose-Einstein distribution function and **u** is the collective drift velocity shared by all the phonon modes. Its effectiveness was first demonstrated for modeling thermal conductivities at low temperatures[8,9], especially for phonon hydrodynamics[10,11], such as phonon Poiseuille flow[12], Knudsen minimum[12,13], and second sound[11].

The exact collision operator could be written with the full scattering matrix:

$$\left(\frac{\partial f^i}{\partial t}\right)_c = -\sum_j W_{ij}(f^j - f_o^j) \tag{1-7}$$

The matrix **W** has the dimension of number of phonons modes. Its construction and relation with the usually three-phonon coupling matrix are discussed in Ref. [14]. Calculation with the full matrix is of high accuracy while computationally expensive.

1.3 First-principles simulation

The recent development of density functional theory (DFT)[15] and density functional perturbation theory (DFPT)[16] enables one to predict the physical properties without fitting parameters. In this section, we are not intending to introduce the development of the first-principles simulation, while focusing on specifying the package used and necessary modifications we made.

The formulation and procedure to perform phonon transport calculation is presented in Ref. [17]. In addition, we have added in the following two features:

1) Distinguish N-scattering rate and U-scattering process.
2) Construct the full scattering matrix from the three-phonon scattering matrix.

All the DFT calculation are performed with Vienna Ab Initio Package (VASP) [18–20] or Quantum ESPRESSO package [21]. The Phonopy package[22] was used to obtain the second-order force constants. The thirdorder.py and ShengBTE packages[17] were used to obtain the third-order force constants and the exact solution to BTE respectively.

The in-house developed code will be released: https://github.com/dingzhiwei007

1.4 Thermal transient grating

Several optical experimental approaches have been developed and utilized to measure thermal transport including flash[23], pump-probe transient thermoreflectance (TTR)[24] and thermal transient grating (TTG)[25–27]. In TTG, two crossed laser pulse created a spatially sinusoidal temperature profile (thermal grating) in the sample and the dynamic of the acoustic and thermal response are monitored via the diffraction of the prove laser beam (Figure 1-3). TTG measurements can be greatly enhanced by optical heterodyne detection after resolving the ambiguities in the interpretation of transient thermal grating signals[28–30].

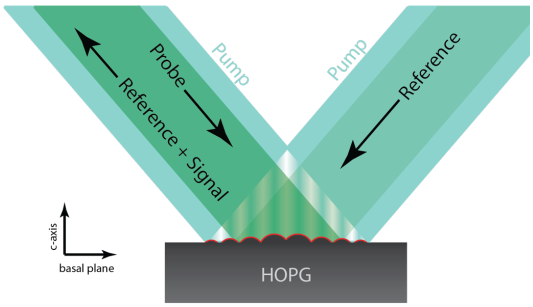

Figure 1-3 Schematic illustration of the experiment. A thermal grating is produced by two crossed pump pulses. Thermal expansion gives rise to a surface modulation that is detected via diffraction of the probe beam, and the reference beam is used for optical heterodyne detection.

To briefly discussed TTG signal, while the details could in found in Ref. [30]. When two short excitation pulses of wavelength λ with incidence angle θ are crossed at the surface of the sample. Optical interference results in a periodic intensity profile with spacing L given as:

$$L = \frac{2\pi}{q} = \frac{\lambda}{2\sin(\frac{\theta}{2})} \tag{1-8}$$

Where q is the grating wavevector magnitude.

Optical fields of the probe and reference beams could be written as:

$$E_p = E_{0p} \exp\left[i\left(k_p^2 - \frac{q^2}{4}\right)^{\frac{1}{2}} z - i\left(\frac{q}{2}\right)x - i\omega_p t + i\phi_p \right] \tag{1-9}$$

$$E_R = t_r E_{0p} \exp\left[i\left(k_p^2 - \frac{q^2}{4}\right)^{\frac{1}{2}} z + i\left(\frac{q}{2}\right)x - i\omega_p t + i\phi_R \right] \tag{1-10}$$

Where E_{0p} is the original amplitude of the probe, k_p is the optical wavevector, ω_p is the optical frequency, ϕ_p and ϕ_R are the phase of the probe and reference beam respectively, t_r is the attenuation factor for the reference beam. The diffracted signal can be written as:

$$t^*(t) = r_0\{1 + \cos(qx)\left[r'(t) + i\left(r''(t) - 2k_p u(t) cos\beta_p\right)\right]\} \tag{1-11}$$

Where $u(t)$ is the vertical surface displacement, β_p is the incidence angle of the probe beam on the surface, and the dynamic complex reflection coefficient is given by $r^*(t) = r_0[1 + r'(t) + ir''(t)]$.

The first order diffraction field of the probe by multiplying Eq. (1-9) with Eq. (1-11):

$$E_{p(+1)} = \frac{1}{2} E_{0p}\, \mathrm{r}_0 \exp\left[i\left(k_p^2 - \frac{q^2}{4}\right)^{\frac{1}{2}} z - i\left(\frac{q}{2}\right)x - i\omega_p t + i\phi_p\right] \tag{1-12}$$

And the reflection reference field is simply obtained as:

$$E_{R(0)} = r_0 t_r E_{0p} \exp\left[i\left(k_p^2 - \frac{q^2}{4}\right)^{\frac{1}{2}} z + i\left(\frac{q}{2}\right)x - i\omega_p t + i\phi_R\right] \tag{1-13}$$

The two beams are colinear and their interference gives an intensity:

$$\begin{aligned} I_s = \frac{1}{2} I_{0p} R_0 \Big\{ & t_r^2 + r'^2(t) + \left[r''^2(t) + 2k_p^2 u^2(t) cos\beta_p\right]^2 \\ & + 2t_r\left[r'(t)\cos\phi - \left(r''(t) - 2k_p u(t) cos\beta_p\right) sin\phi\right]\Big\} \end{aligned} \tag{1-14}$$

Where I_{0p} is the intensity of the probe beam, $R_0 = |r_0|^2$ is the surface reflectivity, and $\phi = \phi_p - \phi_R$ is the heterodyne phase. If the intensity of the reference beam is much greater than that of the diffracted probe, then the time dependent signal is dominated by the heterodyne term

$$I_{het} = 2I_{0p}R_0\left[r'(t)\cos\phi - \left(r''(t) - 2k_p u(t) cos\beta_p\right) sin\phi\right] \quad (1\text{-}15)$$

Eq. (1-15) indicates that the TTG signal have both the reflectivity and displacement.

1.5 Thesis outline

In this thesis, we will focus on the phonon hydrodynamic transport in graphite with a combine theoretical and experimental approach.

In Chapter 2, we discuss the wisdom of N-scattering and U-scattering process. By introducing a direction-dependent definition of normal and Umklapp scattering, we can model thermal transport in anisotropic materials using the Callaway model accurately. This accuracy is physically rooted in the improved description of mode-specific phonon dynamics. Finally, we demonstrate the necessity of the new definition in the phonon hydrodynamic transport regime by computing the propagation length of second sound.

In Chapter 3, by extending the classical Fuchs-Sondheimer solution, we developed a first-principles framework to study phonon hydrodynamics under the size effect with mode-by-mode phonon scattering details. We identify graphite as a three-dimensional material for high-temperature phonon hydrodynamics, thus generalizing a range of 2D materials with strong hydrodynamic characteristics to its bulk van der Waals (vdW) material family. We unambiguously revealed the Poiseuille heat flow by studying the variation of heat flow as the graphite ribbon width. Especially, we identified for the first time the existence of phonon Knudsen minimum – an unusual phenomenon unique to hydrodynamic regime – which can be observed up to 90 K. A thorough microscopic explanation for the phonon Knudsen minimum is elaborated based on the concept of momentum-conserved scattering processes.

In Chapter 4, sub-picosecond transient grating technique was employed to enable direct observation of second sound at a record-high temperature of over 200 K. In addition, with the enlarged grating-period window, we firstly reported the dispersion of thermal wave, whose

velocity increases with decreasing grating period due to the increasing contribution of thermal zero sound—the thermal wave due to ballistic phonons. Our experimental findings are well explained with the interplay among "three fluids": ballistic, diffusive, and hydrodynamic phonons. All the results and analyses are qualitatively supported by first-principle-based solutions of the Peierls-Boltzmann transport equation, which further predicts a large isotope effect on thermal waves and the existence of second sound at room temperature in isotopically pure graphite.

In the last Chapter, we will conclude with our main findings and suggest possible future directions along the path.

Chapter 2 Umklapp Scatterings Are Not Necessarily Resistive

Phonons are the major heat carriers in semiconductors and dielectrics. Since Peierls' pioneering work, it is generally accepted that phonon-phonon scattering processes consist of momentum-conserving normal scatterings and momentum-destroying Umklapp scatterings, and that the latter always induce thermal resistance. Peierls' theory is written into textbooks and used without discrimination. In this chapter, we show that Umklapp scattering processes cause thermal resistance only when they destroy phonon momentum projected along the heat transport direction. This new insight is important for anisotropic materials such as 2D materials and graphite. By introducing a direction-dependent definition of normal and Umklapp scattering, we can model thermal transport in anisotropic materials using the Callaway model accurately. This accuracy is physically rooted in the improved description of mode-specific phonon dynamics. Finally, we demonstrate that second sound might persist over much longer distance than previously thought.

2.1 Background

Phonons are major heat carriers in semiconductors and dielectrics. In crystalline solids, Peierls[1,31] attributed the origin of thermal resistance to the combination of anharmonicity and the discrete nature of crystal lattice. Anharmonicity results in interactions between the lattice vibrational waves, referred to as phonon-phonon scattering processes. However, anharmonicity alone cannot induce resistance as discussed by Peierls[1]—an infinite thermal conductivity is expected if all the phonon scattering processes conserve momentum. To explain the finite thermal conductivity, Peierls proposed that from the perspective of momentum, phonon-phonon scattering could be divided into two categories: normal scattering (N-scattering)[32] and Umklapp scattering (U-scattering). A N-scattering process conserves the phonon momentum and induce no thermal resistance by itself, and it merely redistributes momentum among different phonon modes. In comparison, U-scattering is a momentum-destroying process that leads to thermal resistance[1,3,33–35]. More specifically, for a three-phonon absorption scattering process, the wavevectors of the three phonons satisfy the following constraint:

$$\mathbf{q}+\mathbf{q}'=\mathbf{q}''+\mathbf{G} \tag{2-1}$$

where **q** and **q′** are the wavevectors of the interacting phonons, **q″** is the wavevector of the newly created phonon, and **G** represents a reciprocal lattice vector or zero vector. The conventional definition of N-scattering and U-scattering is illustrated in Figure 2-1, where the first Brillouin zone (BZ) is depicted as a square for simplicity. If the wavevector of the new phonon **q″** is within the first BZ, the three-phonon interaction conserves momentum and is considered as N-scattering (Figure 2-1(a)). However, if **q″** is outside the first BZ (Figure 2-1(b)), the phonon momentum is not conserved ($\mathbf{G} \neq \mathbf{0}$) and the process is categorized as U-scattering. Proper treatment of N-scattering and U-scattering holds the key to model phonon transport, especially to capture the collective drift motion of phonons, which characterizes phonon hydrodynamic transport[36,37]—in analogy to the hydrodynamic flow of molecules[38]. Many exotic phenomena of fundamental importance emerge in the hydrodynamic transport regime, such as phonon Poiseuille flow[12,39], Knudsen minimum[3], and second sound [40–44].

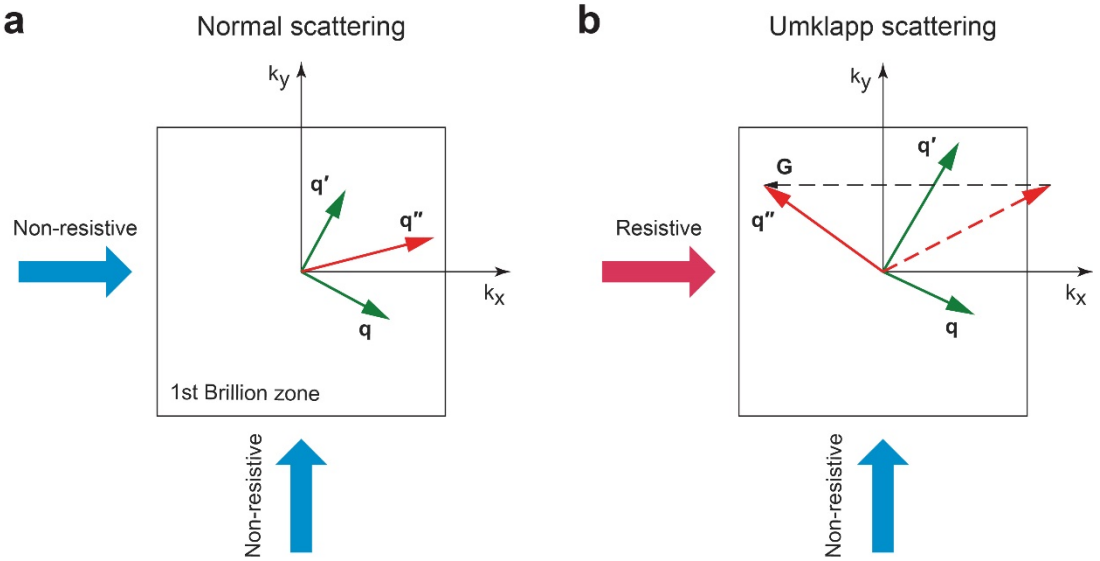

Figure 2-1 Schematic illustration of normal scattering (**N**-scattering) and Umklapp scattering (**U**-scattering) processes, as conventionally defined. (a) **N**-scattering does not induce thermal resistance in either *x*- or *y*-direction, while (b) **U**-scattering induces resistance in *x*-direction but not in *y*-direction.

Major advances in first-principles computations over last decade have enabled solving the phonon Boltzmann transport equation (BTE) numerically without the distinction between N-scattering and U-scattering processes[5,14,45]. However, the high computational cost limits the applicability of such exact solution processes to simple materials, where the number of atoms in a unit cell is within computational resource limits. A more affordable approach appropriate for mesoscale structures is to model phonon-phonon interactions using the relaxation time approximation (RTA), which treats all the phonon scattering processes as U-scattering and represents them with a single lifetime[4–6]. However, the RTA significantly underestimates the thermal conductivity when strong N-scattering is present[7]. To correct for this discrepancy, Callaway proposed a new model to separate the effects of N-scattering and U-scattering on the heat transport, which can be written as:

$$\mathbf{v}_g \cdot \nabla f = -\frac{f - f_o}{\tau_U} - \frac{f - f_d}{\tau_N} \tag{2-2}$$

where f and $\mathbf{v}_g$ denote the phonon distribution function and group velocity, and τ_U^{-1} and τ_N^{-1} represent the U-scattering and N-scattering rates, respectively. While the U-scattering processes relax the phonon distribution to the equilibrium Bose-Einstein distribution f_0, the N-scattering processes facilitate the establishment of a displaced distribution f_d, which can be written as:

$$f_d = \frac{1}{\exp\left[\frac{\hbar(\omega - \mathbf{q}\cdot\mathbf{u})}{k_B T}\right] - 1} \tag{2-3}$$

Here, $\hbar$, ω, $\mathbf{q}$, k_B and T denote the reduced Planck constant, phonon frequency, phonon wavevector, the Boltzmann constant, and temperature, respectively. The collective phonon drift velocity $\mathbf{u}$ is discussed in ref.[46] and can be determined from the conservation of momentum in N-scattering processes:

$$\sum \frac{f - f_d}{\tau_N} \hbar \mathbf{q} = \mathbf{0} \tag{2-4}$$

where the summation is over all phonon modes (same below unless specified). The displaced distribution function is analogous to the BGK approximation for rarefied gas flow.[47]

The Callaway model preserves the efficiency of the RTA while significantly approaches the accuracy of the exact solution schemes and has been truly instrumental to phonon transport studies since it was proposed in 1959. Its effectiveness was first demonstrated for modeling thermal conductivities at low temperatures[8,9], especially for phonon hydrodynamics [10,11], such as phonon Poiseuille flow[12], Knudsen minimum [12,13], and second sound [11]. In past studies, all U-scattering processes are grouped into τ_U, i.e., assumed to create resistance to heat flow.

However, not all U-scatterings as conventionally defined (Figure 2-1) create thermal resistance. In fact, a U-scattering process does not really cause any thermal resistance if the projection of the phonon momentum involved in the scattering is conserved in the heat flow direction. For example, the U-scattering event shown in Figure 2-1(b) only induces resistance to heat flow in the *x*-direction, but not in the *y*-direction. We will show later that this distinction is especially important for anisotropic materials. We hereby propose that a proper classification of N-scattering and U-scattering should be based on the projected phonon momentum in the heat flow direction. A scattering process should be considered N-scattering as long as the phonon momentum is conserved in the direction of heat flow. With this understanding, Eq. (2-1) should be rewritten as:

$$\mathbf{q}_j + \mathbf{q}_j^{'} = \mathbf{q}_j^{''} + \mathbf{G}_j \tag{2-5}$$

where ***j*** represents the heat transport direction, $\mathbf{q}_j$ and $\mathbf{G}_j$ represent the projections of vectors **q** and **G** along ***j*** . A scattering event is N-scattering as long as $G_j = 0$, which holds when $\mathbf{G} = \mathbf{0}$ or **G** is a reciprocal lattice vector orthorgonal to ***j***. Therefore, all the conventional N-scattering processes

remains N-scattering with the new definition, but some scattering processes originally catergorized as U-scatteirng are now classified as N-scattering. To avoid confusion, we denote the heat transport direction-dependent N- and U-scattering processes as N_j- and U_j-scattering. In what follows, by comparing with the exact solutions of the phonon BTE, we demonstrate that the proposed new classification of N-scattering and U-scattering processes leads to much more accurate predictions of thermal conductivity using the Callaway model. We then conclude with a discussion of the significant consequence of the new definition on the propagation length of second sound in the phonon hydrodynamic transport regime.

2.2 Thermal conductivity

We use black phosphorus (BP) and graphite as the prototypical materials to demonstrate how our new definition can improve the performance of Callaway model. These two materials are chosen because they are representative of anisotropic two-dimensional (2D) and 3D materials with one primitive vector orthogonal to the others. The atomic structures of the two materials are shown as insets of Figure 2-2. The computed thermal conductivity of BP along the zigzag (ZZ) direction and graphite in the basal plane direction are plotted in Figure 2-2 as a function of temperature. We focus on transport in these directions because the transport property in the armchair (AM) direction of BP and the cross-plane direction of graphite is insensitive to the treatment of N- and U-scattering (Figure 2-3). Here we compare the thermal conductivities predicted using four different methods: <1> iterative numerical soluton to the BTE which is exact and serves as the reference, <2> Callaway model with the new definition of N- and U-scattering, i.e. N_j- and U_j-scattering, <3> Callaway model with the original definition of N- and U-scattering, and <4> RTA. All the scattering rates were obtained from first-principles calculations. The details for computing thermal conductivity using RTA, Callaway, and the iterative method can be found in Ref. [48]. One can see that both the RTA and the Callaway model with the original definition of N- and U-scattering rates underestimate the thermal conductivity across the wide temperature range considered (100 K - 500 K). With the new definition, the performance of the Callaway model improves significantly at all temperatures. For graphite in particular, the calculated thermal conductivity using Callaway model with the new definition is less than 3% smaller than the exact value.

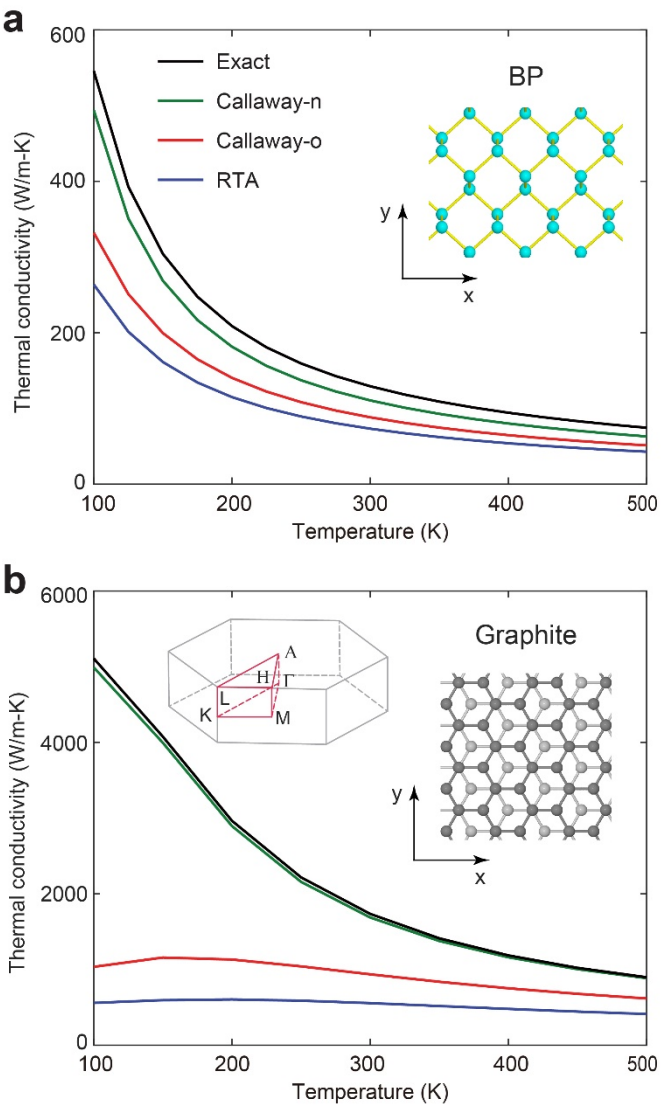

Figure 2-2 Thermal conductivity of (a) BP in the zigzag direction and (b) Graphite in the basal direction. Insets show atomic structures of BP and graphite, as well as the reciprocal space for graphite.

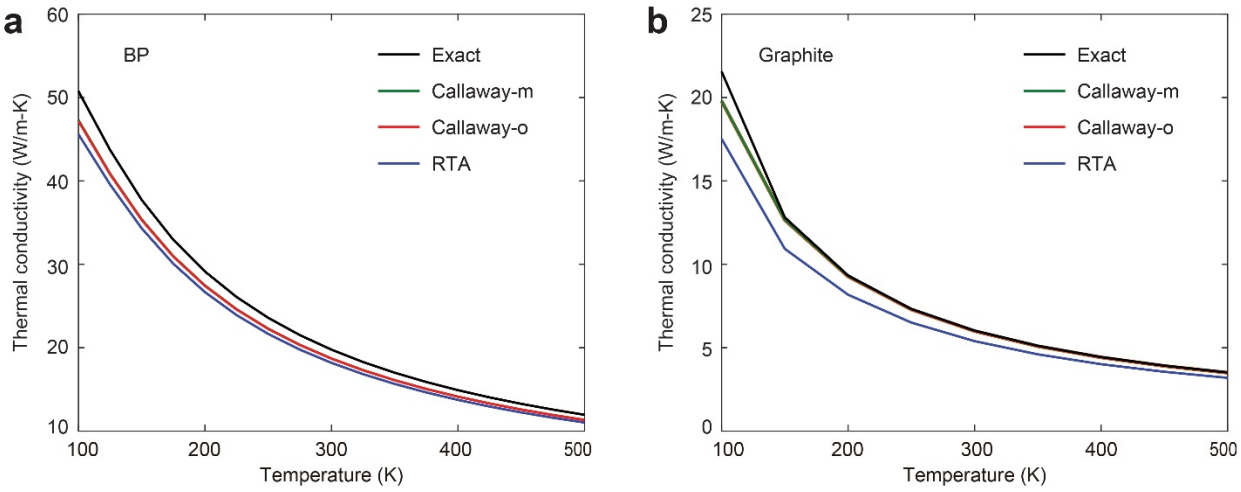

Figure 2-3 Variation of thermal conductivity of BP in the y direction (a) and graphite in the cross-plane direction with temperature

2.3 Effective phonon lifetime

For a more detailed picture, we define an effective phonon lifetime as

$$\tau = \frac{f - f_o}{\frac{\partial T}{\partial x}\frac{\partial f_o}{\partial T} v_x} \tag{2-6}$$

where f is the phonon mode distribution obtained by solving BTE with a temperature gradient $\partial T/\partial x$ in the x-direction. With this effective lifetime, one can readily obtain thermal conductivity via the phonon gas model. In Figure 2-4, we can see that the RTA and the Callaway model with the original definition of N- and U- scattering not only underestimate the effective phonon lifetime, but also leads to effective lifetime distributions that are dramatically different from the exact solution. In contrast, the performance of the Callaway model substantially improves when combined with the N_j- and U_j-scattering rates. In particular, we highlight the region enclosed by the white semi-circle. Phonons in this region is most strongly affected by our modification of the definition of N- and U-scattering. Based on the conventional definition of U-scattering, phonons

with wavevectors near the zone boundary are prone to U-scattering with $\mathbf{G} \neq 0$ in Eq. (2-6). However, our new definition treats a phonon scattering event as N_j-scattering as long as the projection of **G** in the heat transport direction *j* is zero. For example, in BP a phonon with large q_y is prone to U-scattering with $\mathbf{G} = \mathbf{G_y}$ in Eq. (2-1), where $\mathbf{G_y}$ is the lattice vector in the reciprocal space along the k_y-direction. However, this process should be considered as N_j-scattering if heat transport along the *x*-direction is of interest, as the momentum in the *x*-direction is conserved [$\mathbf{G}_j = 0$ in Eq. (2-5)]. Such difference is clearly observed in the distribution of U-scattering percentage in the reciprocal space shown in Figure 2-5. For phonons with small q_y, the percentage of U-scattering rates remains almost unchanged with the modification of definition, while the percentage of U-scattering rates significantly reduces for phonons with large q_y (Figure 2-5). A similar analysis was also performed in graphite for phonons with large q_z [Figure 2-4 (e-h) and Figure 2-6)].

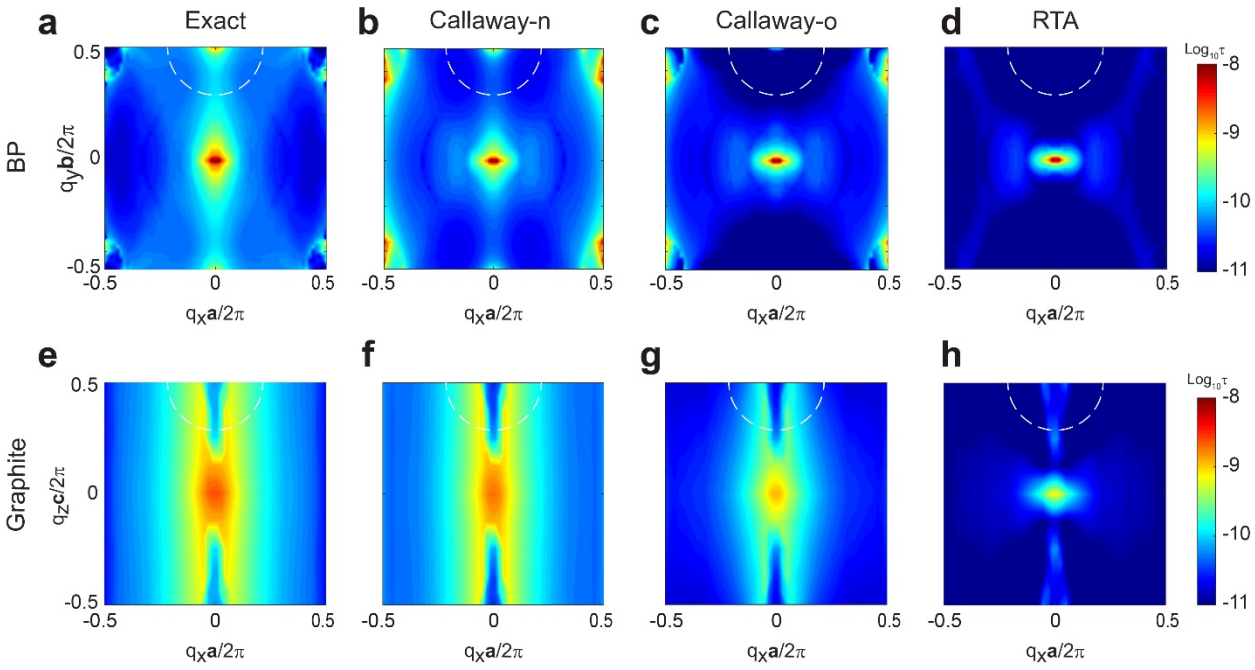

Figure 2-4 Effective lifetime at 300 K under a tempearature gradient in the *x*-direction obtained for BP (a-d) and graphite (e-h) based on (a,e) exact iterative solution; (b,f) the Callaway model with new definition of N- and R-scattering rates; (c,g) the Callaway model with orignal definition; and (d,h) the RTA model. For phonons enclosed by the white semi-circle at the zone boundary in the *y*-direction, conventional U-scattering events can readily take place. However, these scatterings are considered N-scatterings based on the new definition.

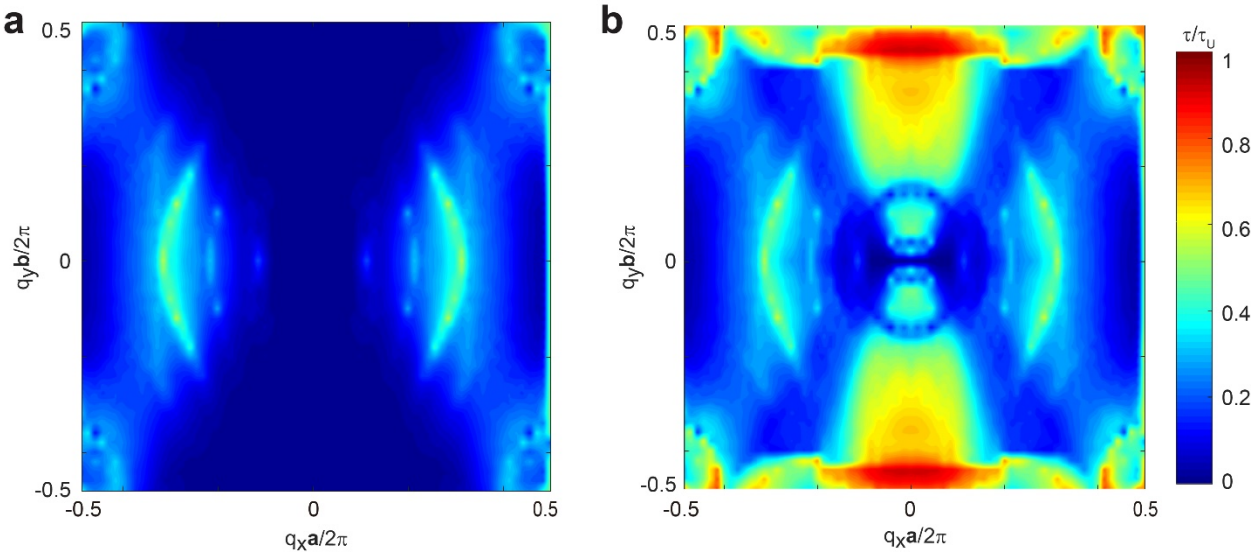

Figure 2-5 Distribution of U-scattering percentage in the reciprocal space for BP with (a) new definition and (b) original definition of N- and U-scattering at 300 K, under a temperature gradient in the x-direction.

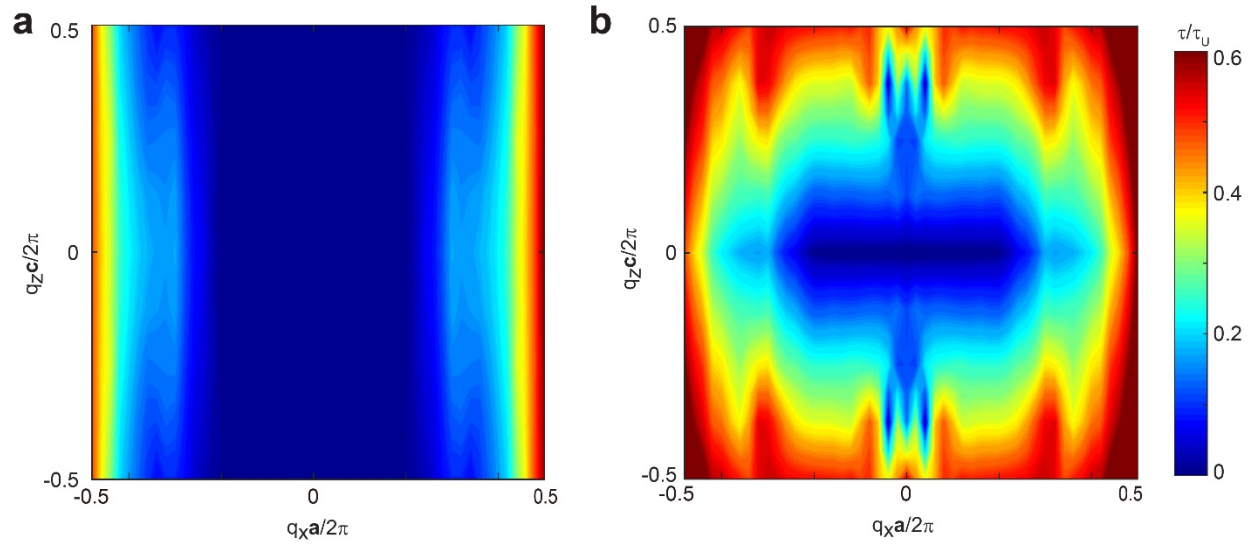

Figure 2-6 Distribution of U-scattering percentage in the reciprocal space of in graphite (a) with modified definition and (b) original definition of N&U-scattering at 300 K under a temperature gradient in the x direction.

2.4 Second sound propagation length

Beyond diffusive transport, phonon hydrodynamic transport has been of great fundamental interest for decades and has recently drawn much revived attention [2,10,49,50]. The Callaway model has been widely employed to investigate many of the characteristic phenomena in hydrodynamic transport such as phonon Poiseuille flow [2,12], second sound [10,11,50], phonon Knudsen minimum [12,13] and phonon viscous flow [51]. Second sound refers to the propogation of heat in a phonon gas, in analogy to the propogation of ordinary sound waves in solids [52,53]. Second sound is of particular interest[53] in thermal transport since it is the most direct demonstration that heat can travel as waves, in contrast to the diffusion process underlying the Fourier heat conduction law. This phenomenon results from the collective phonon motion established by N-scattering when it dominates over U-scattering. Second sound has been experimentally observed at cryogenic temperatures by first applying a heat pulse on one end of a sample then measuring the transient temperature response on the opposite end [42,44,54,55]. The velocity and propagation length of second sound are two critical characteristics for experimental observations.

Following Ref. [56,57], we derive the second sound velocity and propagation length from the energy and momentum-balance equation derived from Boltzmann transport equation (BTE) and Callaway model. The linearized BTE can be written as: (here we assume temperature gradient is along the x direction, but it can be easily extended to higher dimension)

$$\frac{\partial f}{\partial t} + v_x \frac{\partial f}{\partial x} = -\frac{f - f_o}{\tau_U} - \frac{f - f_d}{\tau_N} \tag{2-7}$$

where $\hbar$,ω, $\mathbf{q}$, k_B and T denote the reduced Planck constant, phonon frequency, phonon wavevector, the Boltzmann constant, and temperature, respectively. τ_U^{-1} and τ_N^{-1} are the U-scattering and N-scattering rates respectively and u is the collective drift velocity as discussed in ref.[46]

Denote the background reference temperature as T_o, and following Ref.[56], when τ_N^{-1} is much larger than τ_U^{-1}, we can linearize the distribution function in terms of the deviation temperature $T-T_o$ and drift velocity u:

$$f(T,u) = f_o(T_o) + \frac{C_q}{\hbar\omega}\bar{T} + \frac{T_o q_x}{\omega}\frac{C_q}{\hbar\omega}u \tag{2-8}$$

where $\bar{T}$ is the deviation temperature $T-T_o$

The energy and momentum conservation can be derived by multiplying Eq. (2-7) by $\hbar\omega$ and $\hbar q_x$ respectively and sum over all the modes.

For the energy conservation, as the phonon-phonon scattering process are always energy conserved, the right side of the equation is zero, i.e. $\langle\frac{\hbar\omega(f-f_0)}{\tau_R}\rangle = 0$, we get,

$$\left\langle C_q \right\rangle \frac{\partial \bar{T}}{\partial t} + \left\langle \frac{C_q T_o q_x v_x}{\omega} \right\rangle \frac{\partial u}{\partial x} = 0 \tag{2-9}$$

where <> means summation over all the phonon mode, C_q is mode heat capacity.

Similar for momentum conservation, N-scattering process are momentum-conserved, i.e. $\langle\frac{\hbar q_x(f-f_d)}{\tau_N}\rangle = 0$, thus

$$\left\langle \frac{C_q q_x^2 T_o}{\omega^2} \right\rangle \frac{\partial u}{\partial t} + \left\langle \frac{C_q q_x v_x}{\omega} \right\rangle \frac{\partial \bar{T}}{\partial x} = -\left\langle \frac{C_q q_x^2 T_o}{\omega^2 \tau_U} \right\rangle u \tag{2-10}$$

Combining the above two equations, we get the damped wave equations of the same form as in ref.[58]

$$\frac{\partial^2 \overline{T}}{\partial t^2} + \frac{1}{\tau_{ss}} \frac{\partial \overline{T}}{\partial t} - v_{ss}{}^2 \frac{\partial^2 \overline{T}}{\partial x^2} = 0 \tag{2-11}$$

with the second sound velocity v_{ss} and relaxing time τ_{ss} given as:

$$v_{ss}{}^2 = \frac{\left\langle \frac{C_q q_x v_x}{\omega} \right\rangle^2}{\left\langle \frac{C_q q_x^2}{\omega^2} \right\rangle \langle C_q \rangle} \tag{2-12}$$

$$\frac{1}{\tau_{ss}} = \frac{\left\langle \frac{C_q q_x^2}{\omega^2 \tau_U} \right\rangle}{\left\langle \frac{C_q q_x^2}{\omega^2} \right\rangle} \tag{2-13}$$

The effective mean free path l of the damped wave is given by[59]:

$$l = 2 v_{ss} \tau_{ss} \tag{2-14}$$

The propagation lengths of second sound in BP and graphite predicted using both the original and the new definition are shown in Figure 2-7. One can see that using our new definition, the predicted propagation lengths in both BP and graphite are almost an order of magnitude larger, which indicates the necessity of our new definition in studying phonon hydrodynamic transport

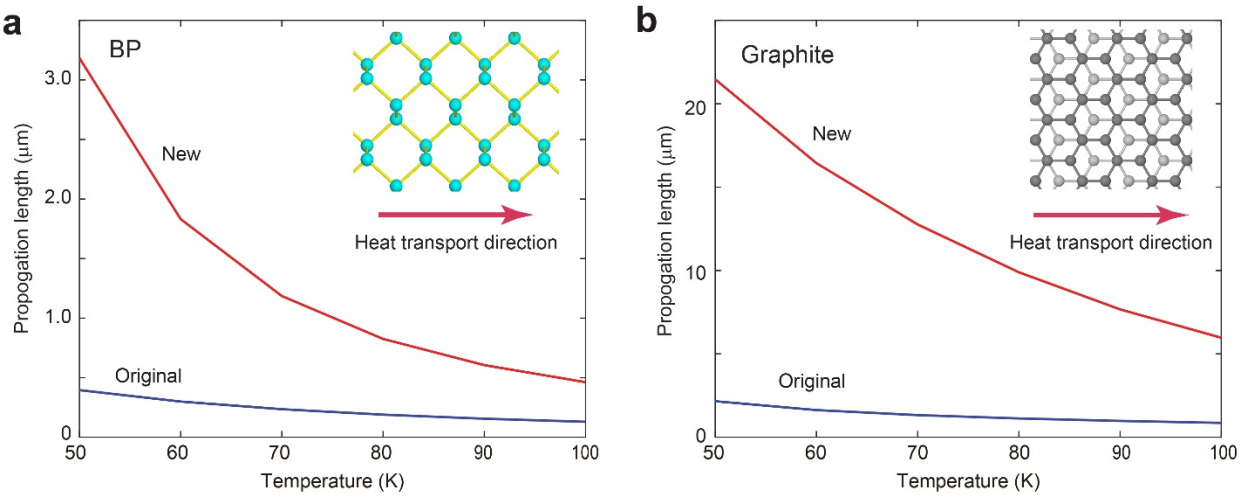

Figure 2-7 Propagation length of second sound as a function of temperature computed using the Callaway model with different definitions of N-scattering and U-scattering in (a) BP and (b) graphite.

2.5 The role of anisotropic

The new interpretation regarding whether a phonon scattering process should be viewed as a U-scattering process is particularly critical in anisotropic materials, where phonons dispersion along one direction (denoted as "soft" axis) is much softer than the other directions ("stiff" directions). For example, in graphite, the weak inter-layer Van der Waals interactions lead to nearly flat dispersion along the cross-plane direction. In such case, if one consider heat flow along stiff axis (e.g. in-plane direction for graphite), there will be significant phonon scatterings involving phonons along the "soft" axis, due to the large scattering phase space provided by the flat phonon band along this axis and their high phonon occupations resulting from the low phonon frequencies. Therefore, phonons as shown in Figure 2-8 (b), suffer from a large amount of scatterings with $\mathbf{G} = \mathbf{G}_{cross}$ (see Eq. (2-1), where $\mathbf{G}_{cross}$ is the lattice vector in the reciprocal space along the cross-plane direction), which are regarded as a Umklapp scattering process based on the conventional wisdom, but have no effect on heat flow along the "stiff" direction in our revised picture.

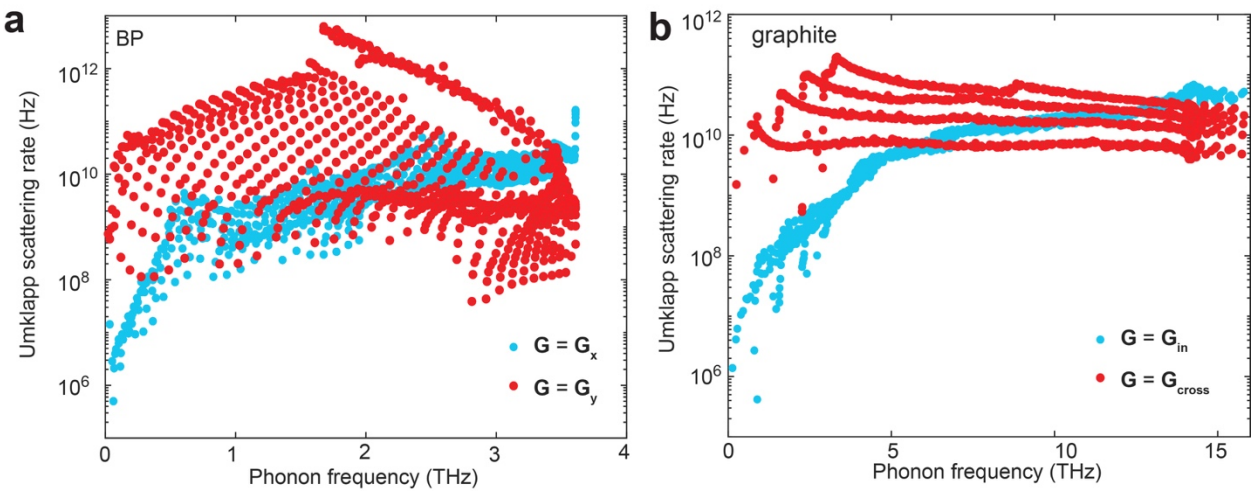

Figure 2-8 Variation of U-scattering rate of the first phonon brantch in (a) BP and (b) graphite due to the breakdown of the momentum conservation in different directions at 300 K, where G = Gx implies that the scattering process is specified by G = Gx as in Eq. (1). $G_{x(y)}$ represents the lattice vector in the reciprocal space in BP along k_x (k_y) directions, and $G_{in(cross)}$ represents the lattice vector in the reciprocal space in graphite along the in-plane (cross-plane) direction.

2.6 Conclusion

In summary, we have shown that, contrary to conventional wisdom pioneered by Peierls, not all U-scattering processes are resistive. Whether or not a U-scattering event contributes to thermal resistance depends on its projection to the heat flow direction. A U-scattering process causes thermal resistance only when the projected momentum is not conserved. This distinction is crucial in anisotropic materials. Using the new definition of N-scattering and U-scattering, we show that the Callaway model combined with the first principles calculations gives a much more precise prediction of the total thermal conductivity and the mode-specific properties as well. By showing its substantial effects on second sound propagation length, we also demonstrate the necessity of our new definition in studying phonon hydrodynamic transport.

Chapter 3 Phonon Hydrodynamic Heat Conduction and Knudsen Minimum in Graphite

In the hydrodynamic regime, phonons drift with a nonzero collective velocity under a temperature gradient, reminiscent of viscous gas and fluid flow. The study of hydrodynamic phonon transport has spanned over half a century but has been mostly limited to cryogenic temperatures (~1 K) and more recently to low-dimensional materials. In this chapter, we identify graphite as a three-dimensional material that supports phonon hydrodynamics at significantly higher temperatures (~100 K) based on first-principles calculations. In particular, by solving the Boltzmann equation for phonon transport in graphite ribbons, we predict that phonon Poiseuille flow and Knudsen minimum can be experimentally observed above liquid nitrogen temperature. Further, we reveal the microscopic origin of these intriguing phenomena in terms of the dependence of the effective boundary scattering rate on momentum-conserving phonon-phonon scattering processes and the collective motion of phonons. The significant hydrodynamic nature of phonon transport in graphite is attributed to its strong intralayer sp^2 hybrid bonding and weak van der Waals interlayer interactions. More intriguingly, the reflection symmetry associated with a single graphene layer is broken in graphite, which opens up more momentum-conserving phonon-phonon scattering channels and results in stronger hydrodynamic features in graphite than graphene. As a boundary-sensitive transport regime, phonon hydrodynamics opens up new possibilities for thermal management and energy conversion.

3.1 Background

Phonons are the dominant heat carriers in most dielectric materials. Phonon transport is usually diffusive and follows Fourier's law of heat conduction, which originates from momentum-destroying phonon scattering processes (R-scattering) such as Umklapp scattering (U-scattering), isotope scattering and impurity scattering. However, collisions between phonons are not necessarily momentum-destroying. Phonon-phonon normal scattering (N-scattering) indeed conserves the total momentum of phonons. If normal scattering is dominant, phonons can develop

a nonzero drift velocity when subjected to a temperature gradient, very much like the viscous flow of a fluid driven by a pressure gradient. In analogy, such a heat conduction regime is called hydrodynamic phonon transport.[36] In general, at sufficiently small length scales and low temperatures, Fourier's law breaks down while hydrodynamic[36] and ballistic[61] transport of phonons emerge. Hydrodynamic transport has been widely studied in diverse systems such as viscous electron flow,[62,63] cold atoms[64] and quark-gluon plasmas.[65] However, for phonons, compared to the extensive studies on its ballistic transport,[66–68] phonon hydrodynamics has drawn much less attention. For decades in the 20th century, it was believed that phonon hydrodynamics occurs only at very low temperatures (~1 K).[42,69–71] More recently, investigations into low-dimensional (1D and 2D) materials have predicted that phonon hydrodynamic transport can also occur at significantly higher temperatures and over a wide temperature range.[2,10,11,72] However, it remains a long-standing challenge to identify bulk materials in which phonon hydrodynamics can take place at relatively high temperatures.

In the hydrodynamic regime, the collective drift of phonons leads to quite a few intriguing phenomena, such as second sound and phonon Poiseuille flow.[2,40,73] The former refers to the wave motion of heat in a phonon gas, which is similar to the propagation of sound waves in ordinary matter; while the latter is analogous to Poiseuille flow of a viscous fluid in a pipe, and is characterized by a phonon thermal conductivity that increases superlinearly with channel width.[37] Further, due to the presence of hydrodynamic effect, a phonon Knudsen minimum is expected near the transition from ballistic to Poiseuille heat conduction. The concept of Knudsen minimum was first introduced in the kinetic transport of rarified gases.[38] It refers to the phenomenon that the normalized flow rate in a channel with respect to the channel width (d) experiences a minimum when d becomes comparable to the mean free path (λ) of the fluid particles, i.e., when the Knudsen number $Kn = \lambda / d$ is around 1. Such a Knudsen minimum was first observed experimentally by Knudsen[38] in 1909 and explained numerically by Cercignani[74] in 1963 by solving the fluid Boltzmann transport equation (BTE). Recently, a similar transport minimum was predicted for viscous electron flow[75,76] and in dilute granular systems.[77,78] The observation of phonon Knudsen minimum was reported many decades ago for heat flow in liquid helium between 0.25 K and 0.7 K.[79] However, its existence in solids above cryogenic temperatures remains an open question.[3]

Hydrodynamic transport is especially sensitive to boundary conditions, and thus offers new opportunities for controlling heat flow via size effect, which is key to efficient thermal management of electronics and thermoelectric energy conversion.[80] Despite past progress in modeling thermal transport in nanostructures,[81–85] studies of various size effects on heat flow were mostly based on the relaxation time approximation (RTA), which considers all phonon-phonon interactions as momentum-destroying and therefore is not suitable for discussing hydrodynamic transport. Description of phonon Poiseuille flow requires proper inclusion of normal scattering processes and phonon drift. Although full BTE solutions with mode-dependent phonon-phonon interactions have been obtained for single crystals, incorporating the size effect imposed by the heat flow boundaries still presents a significant challenge.

In this chapter, we develop a first-principles framework to study phonon hydrodynamics based on mode-specific phonon-phonon scattering details. In particular, we identify graphite as a remarkable three-dimensional material for high-temperature phonon hydrodynamic transport based on a recursive solution to the phonon BTE. This generalizes a range of 2D materials with strong hydrodynamic characteristics to bulk van der Waals (vdW) materials. Combining the relaxation times obtained from first-principles simulations with the Callaway model,[8,86] we solve the linearized BTE for graphite ribbons of different widths. Here, the classical Fuchs-Sondheimer solution[87–89] for the thermal conductivity of a thin film is extended to include phonon drift. We unambiguously reveal the existence of Poiseuille heat flow and superlinear size-dependent thermal transport – a non-trivial signature inherent to the hydrodynamic regime – in graphite ribbons at temperatures up to 90 K. In contrast, Poiseuille heat flow has only been previously observed in liquid helium below 1 K.[39] Further, we predict that the phonon Knudsen minimum – an unusual phenomenon that marks the crossover from ballistic to hydrodynamic transport – can be observed up to 90 K. The microscopic origin of these intriguing phenomena is elaborated based on the interplay between phonon-phonon normal scattering and boundary scattering in a pseudo material.

3.2 Collective phonon drift

A defining signature of hydrodynamic phonon transport is the collective drift motion of phonons, which mathematically manifests itself in the phonon distribution function. As bosons, phonons follow the Bose-Einstein distribution at thermal equilibrium. However, in the presence of a temperature gradient and when N-scattering dominates over R-scattering, phonons would equilibrate towards a displaced Bose-Einstein distribution[46] which is written as:

$$f_d = \frac{1}{\exp\left[\frac{\hbar(\omega + \mathbf{q}\cdot\mathbf{u})}{k_B T}\right] - 1} \tag{3-1}$$

where $\hbar$, ω, $\mathbf{q}$, k_B and T denote the reduced Planck constant, phonon frequency, phonon wavevector, the Boltzmann constant, and temperature, respectively. The drift velocity, $\mathbf{u}$, is constant for all phonon modes regardless of polarization and wavevector. Assuming a small temperature gradient and drift velocity, Eq. (3-1) can be linearized as:

$$f_d = f_0 - f_0(f_0 + 1)\frac{\hbar}{k_B T}\mathbf{q}\cdot\mathbf{u} \tag{3-2}$$

where f_0 is the Bose-Einstein distribution.

Here, using a first-principles calculation framework[5,14,45,90] implemented by the ShengBTE package,[17] the phonon distribution function in an infinitely large graphite crystal under a constant temperature gradient in the zigzag (x) direction is calculated under a steady temperature gradient in the x direction (zigzag) is calculated. To intuitively demonstrate the existence of phonon drift, we define a normalized deviation of the distribution function[2] from the equilibrium Bose-Einstein distribution as $\overline{df} = (f - f_0)/f_0(f_0 + 1)$, where f is the exact solution to the phonon BTE

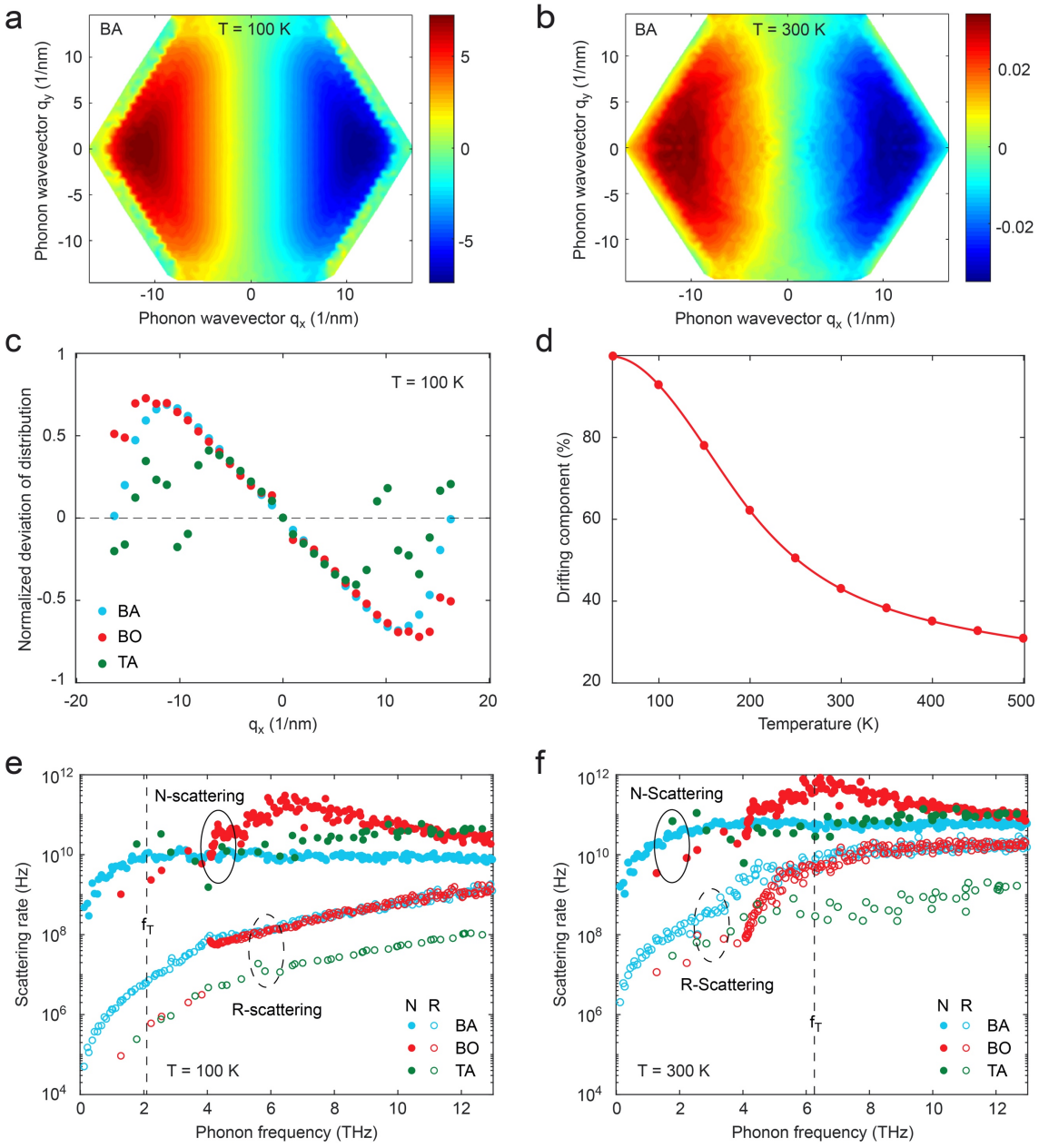

Figure 3-1 Signatures of phonon hydrodynamics in graphite (with 0.1% 13C) under a constant temperature gradient along the zigzag (x) direction. The normalized deviation of distribution function for the bending acoustic (BA) phonon mode in graphite at (a) 100 K and. Signatures of phonon hydrodynamics in graphite (with 0.1% ^{13}C) under a constant temperature gradient along the zigzag (x) direction. The normalized deviation of distribution function for the bending acoustic (BA) phonon mode in graphite at (a) 100 K and (b) 300 K. (c) The normalized deviation for the three lowest-frequency phonon branches (BO and TA stand for bending optical and transverse acoustic, respectively) along the x direction with $q_y = q_z = 0$ at 100 K. (d) Projection of the out-of-equilibrium phonon distribution onto the drifting distribution. Comparison of N-scattering and R-scattering rates with $q_z = 0$ at (e) 100 K and (f) 300 K, where a characteristic frequency $f_T = kT / 2\pi\hbar$ is marked.

Figure 3-1 a-b presents a map of the normalized deviation for the bending acoustic (BA) phonons, where $\overline{df}$ appears linear with **q** along the temperature gradient direction (q_x) at 100 K but the linearity disappears at 300 K (see also Figure 3-2). Moreover, we observe in Figure 3-1c that, at 100 K, $\overline{df}$ is linearly proportional to q_x actually with the same slope for the first three phonon branches, indicating according to Eq. (3-2) a common drift velocity shared by all three branches. Our computation suggests that these three phonon branches contribute more than 90% of the total thermal conductivity (Figure 3-3). With the dominant phonon branches sharing a common drift velocity, we conclude that phonon transport in graphite is in the hydrodynamic regime even at 100 K. Note that the deviation from linearity for high frequency phonons (Figure 3-1c) is exaggerated due to the small values of f_0.

To quantify how close the calculated phonon distribution f is to the ideal displaced distribution f_d, we follow Ref. [10] and define a phonon drifting component as:

$$\rho_d = \frac{\sum C\overline{df}q_x}{\sqrt{\sum C\overline{df}^2}\sqrt{\sum Cq_x^2}} \tag{3-3}$$

where C is the specific heat and the summation is over all phonon modes (same below unless specified). It is easy to see that $\rho_d = 1$ when $f = f_d$. We plot the drifting component for graphite at different temperatures in Figure 3-1d, and reveal that more than 90% of the phonon distribution comes from the collective drift motion at temperatures below 100 K. At room temperature, the drift component reduces to about 40%.

As mentioned earlier, the establishment of a collective phonon drift requires that N-scattering processes dominate over R-scattering. Quantitatively, we plot the mode-specific scattering rates at 100 K and 300 K in Figure 3-1e-f. A characteristic frequency, $k_B T / 2\pi\hbar$, is also marked, below which phonons can be readily activated at a given temperature. Based on these scattering details, we reveal two mechanisms responsible for the suppression of hydrodynamic phonon transport at high temperatures. First, we observe that the significant dominance of N-

scattering over R-scattering rates is reduced at higher temperatures, due to a generally steeper temperature dependence of R-scattering. Moreover, higher temperatures allow phonons of higher frequencies to be populated and contribute to heat flow. However, these high frequency phonons tend to have larger R-scattering rates.

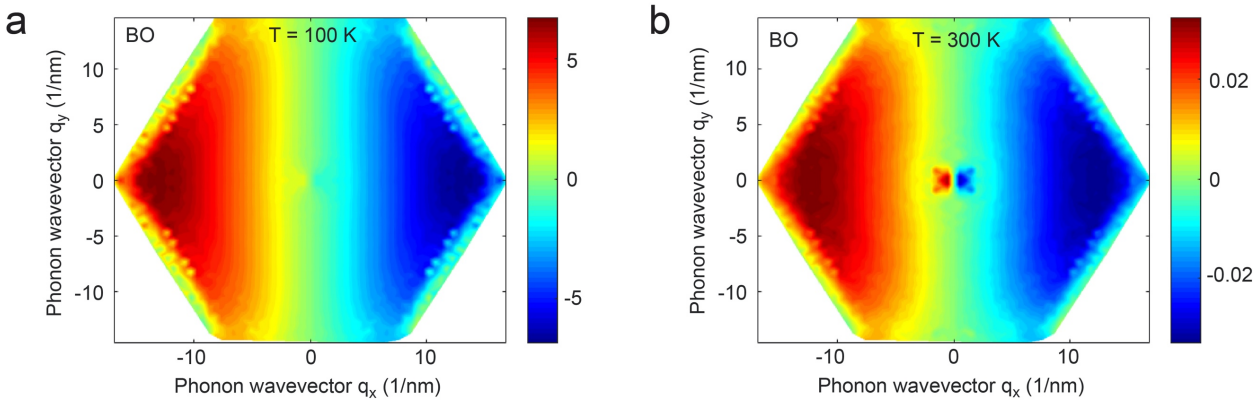

Figure 3-2 The normalized deviation of distribution function for the bending optical (BO) phonon mode in graphite at (a) 100 K and (b) 300 K

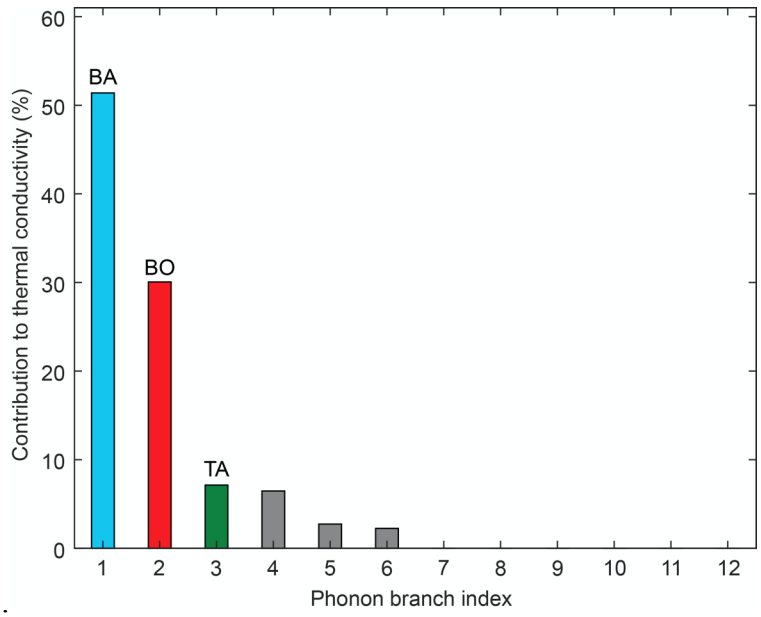

Figure 3-3 Contributions of different phonon branches to the thermal conductivity of graphite at 100 K. The first three braches (BA, BO and TA) contribute to more than 90% of the total thermal conductivity.

3.3 Solving BTE for graphite ribbons under the Callaway model:

We have demonstrated that at 100 K heat transport in graphite is hydrodynamic in nature, as it is dominated by drifting phonons (Figure 3-1d). To further explore the regime of hydrodynamic phonon transport, we consider a graphite ribbon instead of a bulk crystal. In analogy to fluid flow in a pipe, phonon Poiseuille flow and Knudsen minimum become possible with the addition of the flow boundaries.[2,37]

We begin by discussing some general features of heat flow in an infinitely long graphite ribbon (Figure 3-4a). When the sample width is much larger than the R-scattering mean free path (MFP), the transport is in the diffusive regime, and a uniform heat flux profile develops across the ribbon width (Figure 3-4b) because phonon diffusion is dominated by R-scattering throughout the sample. In comparison, ballistic transport occurs when the sample is much narrower than the N-scattering MFP, which is also characterized by a nearly uniform heat flux profile since there is no scattering within the medium. Hydrodynamic transport takes place when the sample width is larger than the N-scattering MFP and but smaller than the R-scattering MFP. Here a quadratic heat flux profile is expected and the phenomenon is thus called phonon Poiseuille flow, analogous to viscous fluid flow.[2,37] The resistance to phonon Poiseuille flow comes mainly from an interplay between diffuse boundary scattering and phonon normal scattering. Briefly, under a temperature gradient a collective phonon drift develops via N-scattering. Since R-scattering is too weak, phonons near the center of the ribbon rarely experiences momentum loss. However, at the ribbon boundaries phonons scatter diffusely and lose a considerable amount of momentum. This leads to a decrease of heat flux from the center to the boundary of the ribbon. Due to the collective phonon drift, the effective boundary scattering rate differs from the Casimir limit.[61,91] Such difference underlies the pronounced size dependence of phonon Poiseuille flow as detailed below.

To accurately calculate the thermal conductivity and heat flux profile in the zigzag graphite ribbon (Figure 3-4a), we have incorporated the Callaway model into the phonon BTE. As demonstrated in a previous study[10] and in Figure 3-5, Callaway model can capture the thermal conductivity of a bulk crystal with good accuracy in the presence of collective phonon drift, since it properly separates the momentum-conserving N-scattering from the resistive scattering processes. Here we further extend this framework to take into account the existence of flow boundaries.

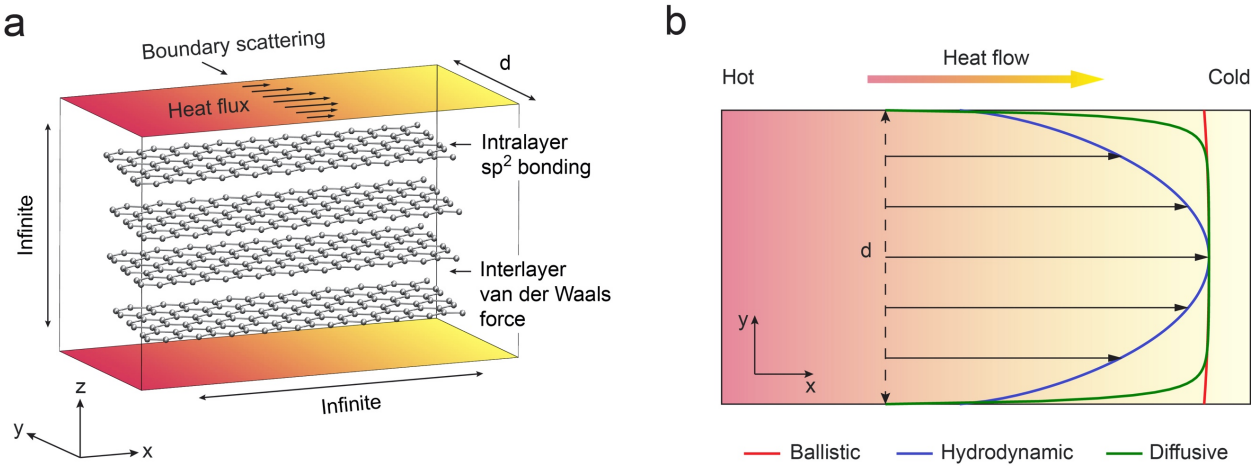

Figure 3-4 Schematic illustration of heat flow in a zigzag graphite ribbon. (a) Modeled graphite ribbon highlighting the finite width and phonon boundary scattering. (b) Heat flux profile in the ballistic, hydrodynamic and diffusive transport regime. The heat flux is essentially uniform in the diffusive and ballistic regimes, while a quadratic profile is expected in the hydrodynamic regime.

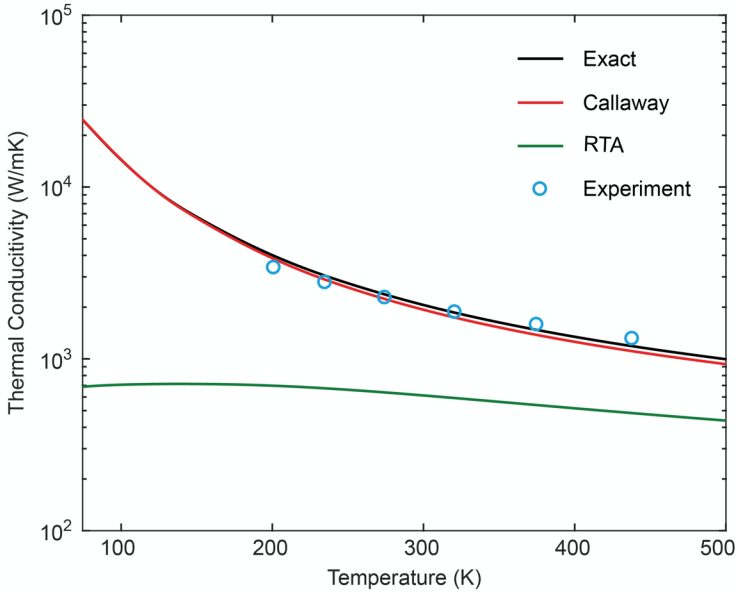

Figure 3-5 Comparison of calculated and measured lattice thermal conductivity of graphite as a function of temperature. The experimental data are extracted from Ref. 6.

For the steady state, the BTE can be written as:

$$v \cdot \nabla f = -\left(\frac{\partial f}{\partial t}\right)_c \tag{3-4}$$

where the term on the right side represents changes in the distribution due to collisions between phonons.

With a temperature gradient applied in x direction, the sample has a finite width in the y direction but an infinite thickness in the z direction. Thus the system is invariant in the z direction. With the Callaway model, the BTE can be written as:

$$v_x \frac{\partial f}{\partial x} + v_y \frac{\partial f}{\partial y} = -\frac{f - f_0}{\tau_R} - \frac{f - f_u}{\tau_N} \tag{3-5}$$

Denote the deviational distribution functions from f_0 and f_u as:

$$f_1 = f - f_0 \tag{3-6}$$

$$f_2 = f - f_u \tag{3-7}$$

Assume that there is no temperature variation in the y direction and the variation of f_1 is much smaller than that of f_0, i.e. $\frac{\partial f_o}{\partial y} \approx 0$ and $\frac{\partial f_1}{\partial x} \approx 0$

In addition, f_2 can be expressed using f_1

$$f_2 = f - f_u = (f - f_0) + (f_0 - f_u) = f_1 + \frac{T}{\hbar\omega}\frac{\partial f_0}{\partial T}u_x q_x \tag{3-8}$$

where u_x is drift velocity in the x direction and other components of the drift velocity are zeros

Also from the Matthiessen's rule[92], the total scattering rate can be written as:

$$\frac{1}{\tau_T} = \frac{1}{\tau_N} + \frac{1}{\tau_R} \tag{3-9}$$

Substituting in Eq. (3-7)(3-8)&(3-9), Eq. (3-4) can be simplified as:

$$v_y \frac{\partial f_1}{\partial y} + \frac{f_1}{\tau_T} = -(v_x \frac{\partial T}{\partial x} + \frac{T}{\hbar\omega}\frac{u_x q_x}{\tau_N})\frac{\partial f_0}{\partial T} \tag{3-10}$$

The general solution to Eq. (3-10) can be written as:

$$f_1(y, v_y \neq 0) = e^{-\frac{y}{\tau_T v_y}}(C + \int_0^y -\frac{1}{v_y}(v_x \frac{\partial T}{\partial x} + \frac{T}{\hbar\omega}\frac{u_x(t)q_x}{\tau_N})\frac{\partial f_0}{\partial T}e^{\frac{t}{\tau_T v_y}}dt) \tag{3-11}$$

$$f_1(y, v_y = 0) = -\tau_T(v_x \frac{\partial T}{\partial x} + \frac{T}{\hbar\omega}\frac{u_x q_x}{\tau_N})\frac{\partial f_0}{\partial T} \tag{3-12}$$

where C is an arbitrary constant needs to be determined from the boundary conditions.

Diffusive boundary conditions are assumed at the top and bottom edges, which implies:

$$f_1(y=0, v_y>0)=0 \tag{3-13}$$

$$f_1(y=d, v_y<0)=0 \tag{3-14}$$

where d the width of the sample as is indicated in Figure 3-4(a)

The constant C in Eq. (3-11) can be evaluated accordingly from the boundary conditions. The general solution of the distribution function could be written as:

$$f_1(y, v_y>0)=-\tau_T v_x \frac{\partial T}{\partial x}\frac{\partial f_0}{\partial T}(1-e^{-\frac{y}{\tau_T v_y}})-e^{-\frac{y}{\tau_T v_y}}\frac{1}{v_y}\frac{T}{\hbar\omega}\frac{\partial f_0}{\partial T}\frac{q_x}{\tau_N}\int_0^y u_x(t)e^{\frac{t}{\tau_T v_y}}dt \tag{3-15}$$

$$f_1(y, v_y<0)=-\tau_T v_x \frac{\partial T}{\partial x}\frac{\partial f_0}{\partial T}(1-e^{\frac{d-y}{\tau_T v_y}})+e^{-\frac{y}{\tau_T v_y}}\frac{1}{v_y}\frac{T}{\hbar\omega}\frac{\partial f_0}{\partial T}\frac{q_x}{\tau_N}\int_y^d u_x(t)e^{\frac{t}{\tau_T v_y}}dt \tag{3-16}$$

Now we have obtained the distribution function in terms of the drift velocity.

The drift velocity can be determined from the local equilibrium condition, where the total crystal momentum is conserved during the normal scattering process as discussed in ref. [86]

$$\sum(f-f_\lambda)q_x=\sum(f_1+\frac{T}{\hbar\omega}\frac{\partial f_0}{\partial T}u_x q_x)q_x=0 \tag{3-17}$$

Define $\langle\ \rangle_q$ as summation over all the states, and $\langle\ \rangle_+, \langle\ \rangle_- \& \langle\ \rangle_0$ as summation over all the states with positive, negative and zero velocity in y direction respectively

Substitute Eq. (3-15) and (3-16) into Eq. (3-17), and eliminate f_1, we get an integral equation of the drift velocity u_x

$$u_x D - \int_0^d E(y,t) u_x(t) dt = F(y) \tag{3-18}$$

With

$$D = \left(\left\langle \tau_T \frac{\partial f_0}{\partial T} \frac{T}{\hbar \omega} \frac{{q_x}^2}{\tau_N} \right\rangle_0 - \left\langle \frac{T}{\hbar \omega} \frac{\partial f_0}{\partial T} {q_x}^2 \right\rangle_q \right) \tag{3-19}$$

$$F(y) = -\left\langle \tau_T v_x q_x \frac{\partial f_0}{\partial T} \frac{\partial T}{\partial x} \right\rangle_q + \left\langle \tau_T v_x q_x \frac{\partial T}{\partial x} \frac{\partial f_0}{\partial T} e^{-\frac{y}{\tau_T v_y}} \right\rangle_+ + \left\langle \tau_T v_x q_x \frac{\partial T}{\partial x} \frac{\partial f_0}{\partial T} e^{\frac{d-y}{\tau_T v_y}} \right\rangle_- \tag{3-20}$$

$$E(y,t) = \left\langle \frac{1}{v_y} \frac{T}{\hbar \omega} \frac{\partial f_0}{\partial T} \frac{{q_x}^2}{\tau_N} e^{\frac{t-y}{\tau_T v_y}} \theta(t-y) \right\rangle_- - \left\langle \frac{1}{v_y} \frac{T}{\hbar \omega} \frac{\partial f_0}{\partial T} \frac{{q_x}^2}{\tau_N} e^{\frac{t-y}{\tau_T v_y}} \theta(y-t) \right\rangle_+ \tag{3-21}$$

where θ is the step function, i.e. $\theta(x) = 1, x > 0$ and $\theta(x) = 0$, otherwise.

We notice that Eq. (3-18) is a Fredholm integral equation of the second kind which can be solved numerically[74].

After obtaining the drift velocity, the distribution function can be obtained by plugging the value of drift velocity into Eq. (3-12)(3-15)&(3-16),from which the heat flux and thermal conductivity can be calculated respectively as:

$$J = \frac{1}{N_p V} \sum f_1 \hbar w v \tag{3-22}$$

$$k = -\frac{1}{d \, \partial T / \partial x} \int_0^d J dy \tag{3-23}$$

where N_p is the number of mesh points and V is volume of unit cell.

In the above derivation, we have assumed a diffuse boundary condition. Now we demonstrate its justification. The specularity of the boundary can be quantified via the specularity parameter, which can be estimated using Ziman's formula:[35,93]

$$p(\varsigma) = \exp\left(-\frac{16\pi^2\eta^2}{\varsigma^2}\right) \tag{3-24}$$

where ζ and η are the phonon wavelength and root mean square of the edge roughness respectively. Diffuse boundary condition is specified by a specularity parameter p = 0, while specular boundary condition is given by p = 1.

Because the specularity depends on the phonon wavelength, we present the normalized accumulated thermal conductivity with respect to the phonon wavelength at 50 K and 90 K in Figure 3-6a, where the accumulated thermal conductivity is defined as:

$$\kappa(\varsigma_m) = \frac{\sum_{\varsigma} k_{\varsigma}\theta(\varsigma_m - \varsigma)}{\sum_{\varsigma} k_{\varsigma}} \tag{3-25}$$

The experimentally reported edge roughness η for graphene is around 3 nm[94], which is about 40% more than the edge roughness of bulk graphite[95]. We think a reasonable estimation for the edge roughness in graphite is 2 nm. The variation of specularity parameter with phonon wavelength for an edge roughness of 2 nm is presented in Figure 3-6b. The accumulated thermal conductivity plot suggests that phonons dominantly contributing to the thermal transport have wavelengths less than 10 nm. For 10 nm and below, the specularity plot then shows that these modes are mostly diffusely scattered at the boundary, with specularity parameters mostly <0.002. This justifies the assumption of fully diffuse boundary condition in our model within the temperature range we studied.

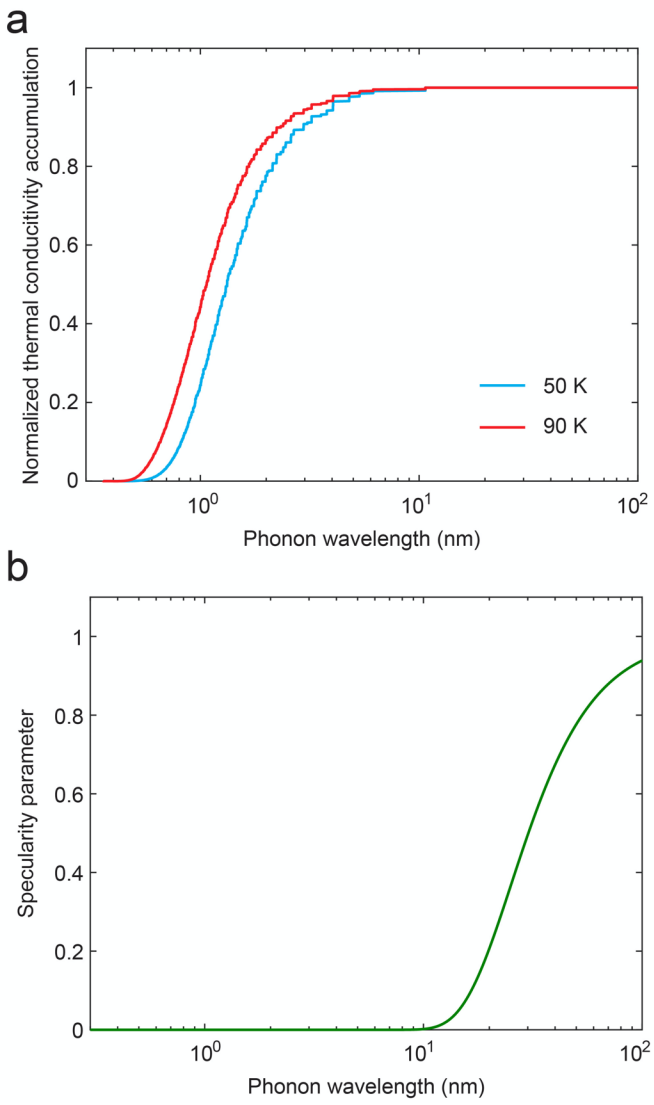

Figure 3-6 Diffuse boundary scattering in graphite at low temperature. (a) Normalized accumulation function. (b) Specularity parameter (p) estimated from Eq. (16) with edge roughness $\eta = 2$ nm.

This allows us to investigate phonon hydrodynamic transport in the context of size effect. Our calculation shows that the heat flux profiles in graphite ribbons of different widths at 70 K exhibit clear transitions between the ballistic, hydrodynamic and diffusive regime, when N-scattering dominates over R-scattering (Figure 3-7a). This is a direct consequence of the large phonon drift at low temperatures (Figure 3-1d). In comparison, at 300 K the hydrodynamic regime is missing because R-scattering dominates the phonon transport (Figure 3-7b).

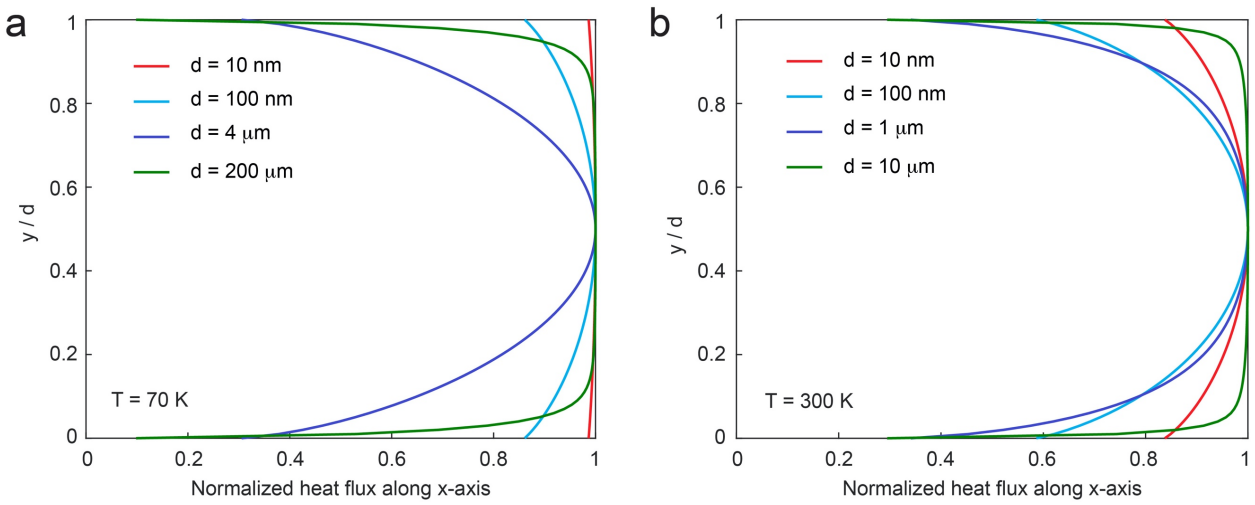

Figure 3-7 Calculated and normalized heat flux profile for different sample widths at (a) 70 K and (b) 300 K. Clear transitions between the ballistic, hydrodynamic and diffusive regime at 70 K are observed when N-scattering dominates over R-scattering. In comparison, the hydrodynamic regime is missing at 300 K, where R-scattering dominates.

3.4 Phonon Poiseuille flow and Knudsen minimum

We now explore how the thermal conductivity (k) of a graphite ribbon varies as a function of ribbon width (d) at different temperatures, as shown in Figure 3-8a. A finite sample width in general suppresses heat transport, but the width dependence of thermal conductivity may vary with temperature. To characterize the various transport regimes, we define a dimensionless scaling ratio α as $\alpha = \partial ln(k)/\partial ln(d)$ (Figure 3-8b), which suggests that around width d the thermal conductivity scales as $k \propto d^{\alpha}$. And $\alpha = 0$ relation is typical for diffusive transport (size-independent), while $\alpha > 1$ implies a superlinear size-dependence. At low temperature, where phonon hydrodynamic transport plays a critical role, we find that the scaling ratio with respect to the width increases first before reducing to zero eventually in the diffusive regime (Figure 3-8b). Intriguingly, at low temperatures (say 50 K) when drifting phonons dominate the transport, a superlinear ($\alpha > 1$) width dependence of thermal conductivity is clearly observed (Figure 3-8b), which is a direct consequence of the phonon Poiseuille flow.[2,37]

Such superlinear scaling can be understood based on the kinetic transport theory, in which the thermal conductivity k is expressed as:

$$k = \sum Cv^2\tau \tag{3-26}$$

where v is the phonon group velocity, and τ is the phonon lifetime due to resistive scattering processes which can be expressed using Matthiessen's rule:[92]

$$\frac{1}{\tau} = \frac{1}{\tau_U} + \frac{1}{\tau_I} + \frac{1}{\tau_B} \tag{3-27}$$

where the subscripts *U*, *I* and *B* denote Umklapp scattering, isotope scattering and boundary scattering, respectively. In the Poiseuille hydrodynamic regime, phonon scattering at the boundaries (τ_B) dominates, which is often described by the Casimir theory:[61]

$$\frac{1}{\tau_B} = \frac{2|v_y|}{d} \tag{3-28}$$

where *d* is the sample width and v_y is the phonon group velocity perpendicular to the boundary.

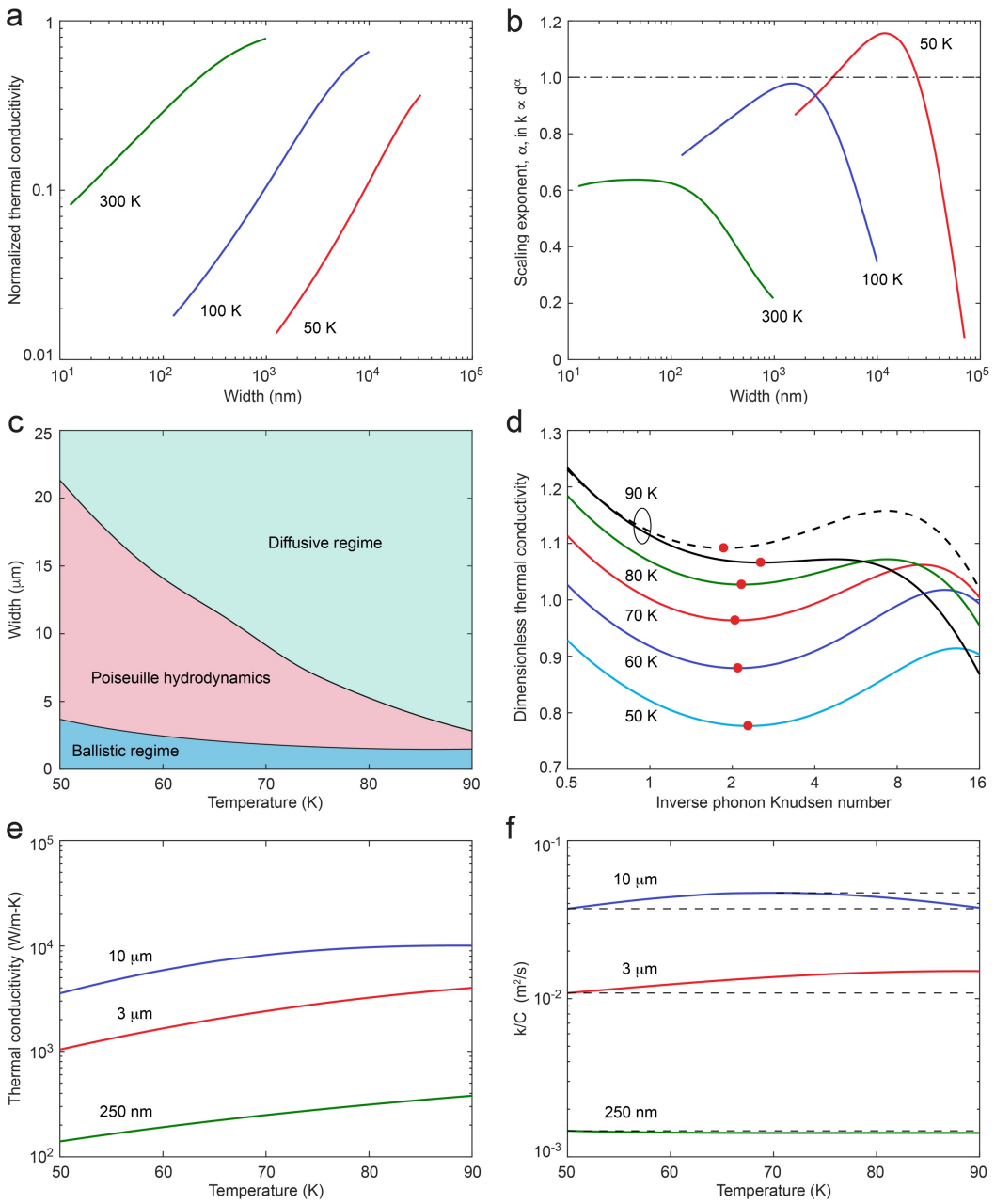

Figure 3-8 Thermal transport in graphite ribbons as a function of ribbon width and temperature. (a) Thermal conductivity variation with ribbon width at different temperatures. (b) Scaling of thermal conductivity with respect to ribbon width. A superlinear scaling scaling window is observed at 50 K. (c) A map of various heat transport regimes with respect to ribbon width and temperature, using the superlinear size-dependence as a signature of Poiseuille heat flow. (d) Variation of the dimensionless thermal conductivity with the inverse phonon Knudsen number at different temperatures. The solid lines are obtained for graphite with 0.1% ^{13}C and the dashed lines are for isotopically pure graphite. Thermal conductivity as a function of temperature for graphite ribbons of different widths. (e) Thermal conductivity, and (f) thermal conductivity normalized by heat capacity, k/C. Increasing k/C with rising temperature is an indicator of hydrodynamic Poiseuille heat flow. The horizontal dashed lines in (f) mark zero temperature dependence.

Although the Casimir theory indeed captures diffuse phonon scattering at the flow boundaries, it only leads to sublinear width dependence for the thermal conductivity. To explain the unusual superlinear width dependence, one has to re-think how boundary scatterings effectively destroy phonon momentum when there is collective drift motion. When explaining the temperature dependence of thermal conductivity in crystalline He^4,[96] Gurzhi[97,98] proposed that phonons in the hydrodynamic regime should experience an effective boundary scattering given by:

$$\frac{1}{\tau_B} = \left(\frac{2\lambda_N}{d}\right)^2 \frac{1}{\tau_N} \tag{3-29}$$

where λ_N is the N-scattering mean free path ($\lambda_N = v\tau_N$). Equation (3-29) relates phonon boundary scattering to N-scattering. Further, the boundary scattering rate is proportional to the inverse square of the ribbon width, rather than the inverse width as in Eq. (3-28). Compared to the Casimir theory, Gurzhi essentially suggests that phonons experience progressively less scatterings from the boundary in the hydrodynamic regime, as the ribbon width increases. The microscopic mechanism for this will be discussed in detail later. We note that although the relaxation time given by Eq. (3-29) is only an estimation for the effective boundary scattering, it does correctly capture the qualitative feature of the hydrodynamic regime – a superlinear width dependence of the ribbon thermal conductivity.

Using the superlinear scaling as a signature for phonon Poiseuille flow, we have further mapped out the different transport regimes with respect to sample width and temperature (Figure 3-8c). At 80 K, the phonon Poiseuille flow could be observed when the sample width is within 2.5 – 3.0 μm, and increasingly wider range is predicted at lower temperatures. We note that the maximum temperature to observe phonon Poiseuille flow can be further increased by reducing isotope scattering. Specifically, a width window of 1.7 – 2.7 μm is predicted for isotopically pure graphite ribbon at 90 K (Figure 3-8b).

As the ribbon width keeps decreasing, phonon transport eventually transitions from the hydrodynamic to the ballistic regime. At the transition width, the phonon Knudsen minimum is expected to occur. As discussed earlier, phonon Knudsen minimum for heat flow has only been

reported in liquid helium between 0.25 K and 0.7 K.[79] Here we predict that in graphite ribbons the Knudsen minimum in phonon transport can be observed at temperatures as high as 90 K. In analogy to the dimensionless flow rate in rarified gas flow, we define a dimensionless thermal conductivity as:[79]

$$\bar{k} = \frac{3k}{Cv_s d} \tag{3-30}$$

where v_s is the sound velocity in graphite.[99] The non-dimensionalization in Eq. (3-30) follows a definition traditionally used to describe Knudsen minimum in rarefied gas flow,[2,37] and differs from the normalized thermal conductivity plotted in Fig. 3a, which is the ratio of the ribbon thermal conductivity to the bulk value. Further, considering the broad distribution of phonon MFP, we define an average phonon MFP associated with N-scattering and weighted by the mode-specific contribution to the total thermal conductivity as: [100]

$$\langle \lambda_N \rangle = \frac{\sum Cv\lambda_N}{\sum Cv} \tag{3-31}$$

This allows us to use an effective phonon Knudsen number (defined as $Kn = <\lambda_N>/d$) to characterize the heat flow. The dimensionless thermal conductivity with respect to the inverse phonon Knudsen number at different temperatures is shown in Figure 3-8d, with the conductivity minima highlighted by the red dots. Strikingly, the phonon Knudsen minimum can be observed at temperatures up to 90 K, under the assumption of diffuse boundary scattering. The highest temperature to observe Poiseuille flow is expected to vary with respect to edge roughness as discussed in the dilute granular system.[77] Smoother boundary conditions facilitate the observation of Poiseuille flow and Knudsen minimum for relatively rough surfaces.[77] Therefore, employing diffuse boundary condition represents a conservative estimation for the temperature limit in practical cases.

Another evidence of phonon Poiseuille flow is found in the temperature dependence of the ribbon thermal conductivity,[96–98] which can be written as $k = Cv\lambda$ based on kinetic theory. Since

the group velocity v is essentially temperature independent, the heat-capacity-normalized thermal conductivity, k/C, should have the same temperature dependence as the phonon MFP, λ. In the ballistic regime, λ is limited by boundary scattering thus mostly temperature independent, leading to an almost constant k/C with varying temperature. In the diffusive regime, λ decreases with increasing temperature due to increased U-scattering rates. However, with Poiseuille phonon flow, λ is expected to increase as temperature rises. This is because in the hydrodynamic regime, the thermal resistance mainly comes from boundary scattering. As temperature increases, normal scattering between phonons becomes more frequent, effectively making the boundary scattering smaller [see Eq. (3-29)]. Therefore, an increase of k/C with temperature serves as an indicator of hydrodynamic heat flow. As shown in Figure 3-8 e-f, a clear increase of k/C with rising temperature is observed when the graphite ribbon width is about 3 μm, suggesting hydrodynamic thermal transport. When the ribbon width is 250 nm, k/C is essentially constant (slightly decreasing) with temperature, indicative of the ballistic regime. For a ribbon width of 10 μm, k/C first increases at low temperatures but starts decreasing at higher temperatures, demonstrating a transition from hydrodynamic to diffusive transport. All these observations are consistent with the regime map shown in Figure 3-8c.

At last we note that real samples are hardly perfect. In order to investigate the robustness of phonon hydrodynamics with respect to sample quality, we looked into the effect of vacancies as an example. We treat vacancy scattering as mass disorder,[101] and find that collective phonon drift motion is destroyed when the vacancy concentration is about 0.01%, but can still be observed when the concentration is about 0.001% (Fig. 4a-b). The regime map of graphite with 0.001% and 0.002% vacancy defects are shown in Fig. 4c-d. One can see that, in the presence of defects, phonon Poiseuille flow can become insignificant at low temperatures (Fig. 4d). This is because, at very low temperatures, both N-scattering and U-scattering are reduced, while defects scattering becomes dominant. Because phonon scatterings by defects are not momentum conserving, phonon hydrodynamic flow disappears at sufficiently low temperatures.

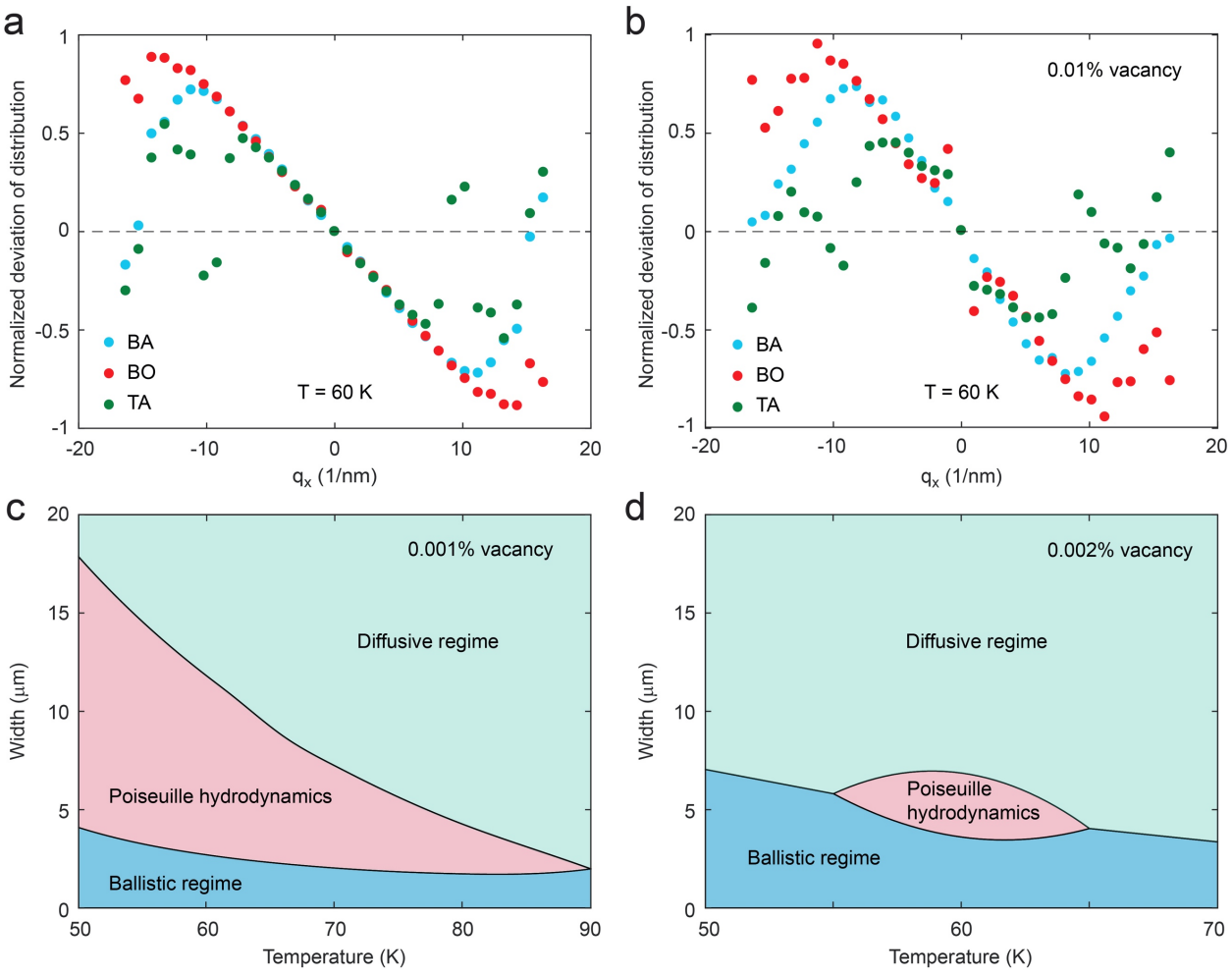

Figure 3-9 Thermal transport in graphite ribbons with defects. The normalized deviation of distribution function of the three lowest frequency phonon branches along the x-direction with qy = qz = 0 at 60 K in graphite with (a) 0.001% and (b) 0.01% vacancies. Maps of various heat transport regimes with respect to ribbon width and temperature, using the superlinear size-dependence as a signature of Poiseuille heat flow in graphite with (c) 0.001% (d) 0.002% vacancies

3.5 Microscopic origin of Knudsen minimum

The existence of phonon Knudsen minimum has been elusive in theory, particularly in solid materials. Here, we present a microscopic picture for the origin of the phonon Knudsen minimum. To elaborate on the effect of collective drift motion of the size effect, we constructed a pseudo material with adjustable scattering rates. More specifically, we consider a material with Debye temperature of 500K with a sound velocity 1 km/s. A sphere is assumed for the first Brillouin zone and a mesh grid $50\times50\times50$ is used. We vary the N-scattering: $\tau_N^{-1}=0$ Hz and $\tau_N^{-1}=10^{10}$ Hz for comparison. Further, we neglect R-scattering while only considering N-scattering and boundary scattering. For N-scattering, we compare cases with a scattering rate of 10^{10} Hz or zero, with zero indicating the absence of N-scattering. Before delving into the computational results, it may be instructive to note that in fluid flow, all scattering events are momentum-conserving and there is intrinsically no mechanism equivalent to phonon-phonon U-scattering. This means that the phonon flow in our pseudo material is actually a faithful analog of fluid flow. The existence of U-scattering will make the thermal conductivity eventually saturate at large width limit, as shown in Figure 3-10, which is an effect the fluid flow does not have.

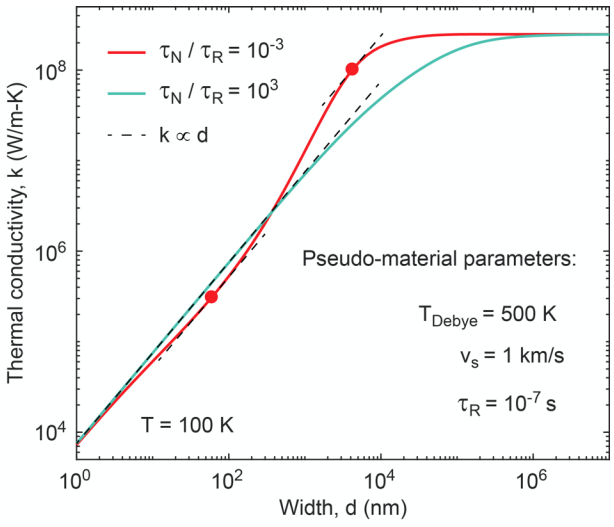

Figure 3-10 Calculated thermal conductivity of a pseudo-material as a function of sample width. Both N- and R-scattering are considered.

In Figure 3-11a we plot the calculated thermal conductivity of the pseudo material ribbon as a function of ribbon width, while Figure 3-11b shows the corresponding dimensionless thermal conductivity. When N-scattering is absent, phonons propagate ballistically until being diffusely scattered at the boundary, which translates to an effective MFP linearly proportional to the sample width. By writing Eq. (3-26) in terms of phonon MFP as $k = \sum Cv\lambda$, one can see that in ballistic transport the sample thermal conductivity linearly varies with the sample width. According to Eq. (3-30), this means that the dimensionless thermal conductivity remains constant with varying sample width. When N-scattering is added into the picture, however, the thermal conductivity can be suppressed or enhanced, depending on the sample width (Figure 3-11a). For small sample width, N-scattering serves mainly to increase boundary scattering, which reduces the sample thermal conductivity at a given width and leads to a smaller dimensionless thermal conductivity than the ballistic case. While for large sample width, N-scattering actually weakens boundary scattering, as previously pointed out by Gurzhi,[97,98] thereby leading to a larger dimensionless thermal conductivity than ballistic transport. These two considerations imply that there must be a minimum dimensionless thermal conductivity, that is, the phonon Knudsen minimum.

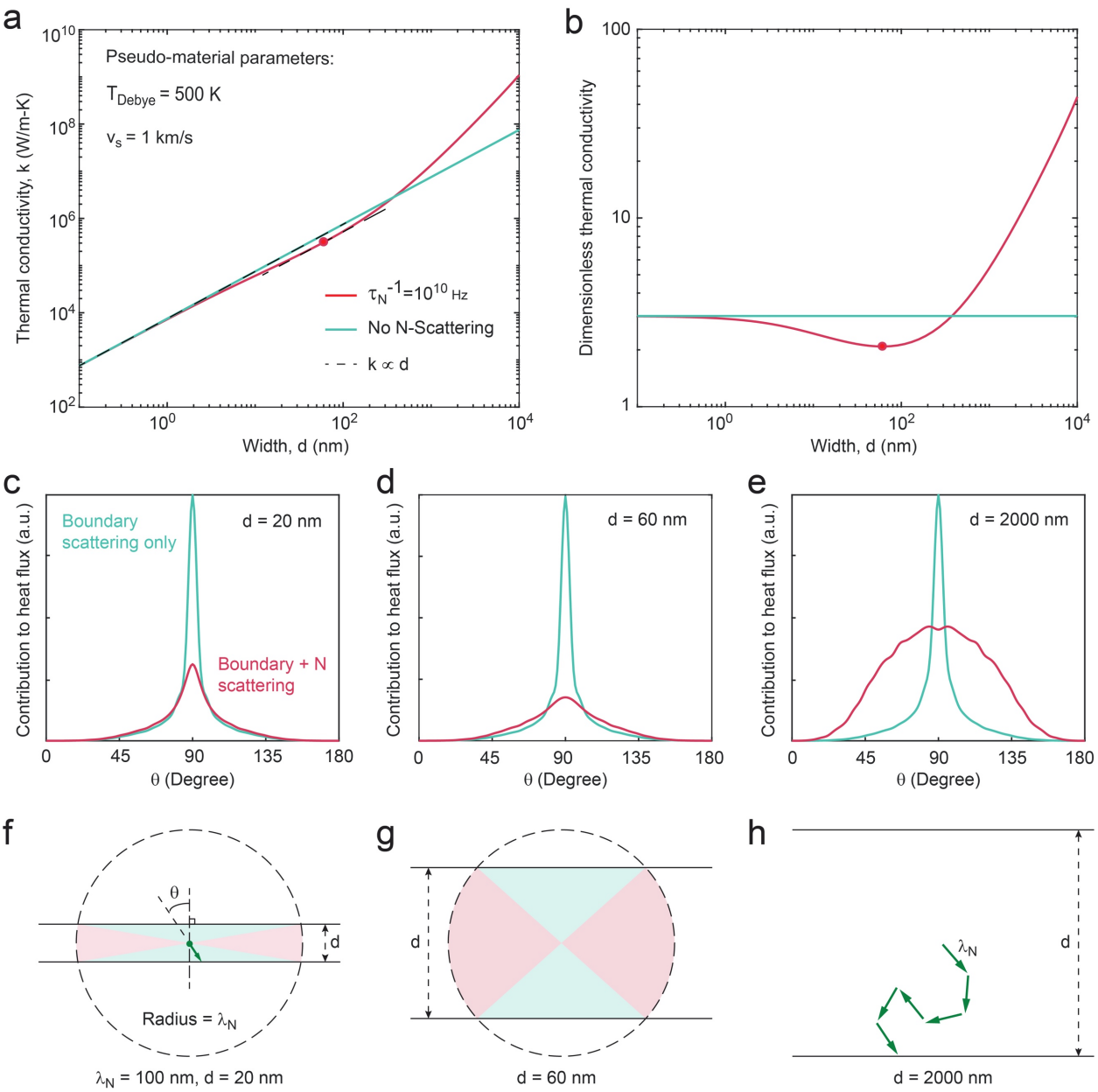

Figure 3-11 The microscopic origin of phonon Knudsen. (a) Calculated thermal conductivity of a pseudo material as a function of sample width. (b) Variation of the dimensionless thermal conductivity with sample width. Phonon angle-dependent heat flux contribution with/without N-scattering for selected sample widths: (c) d = 20 nm, (d) d = 60 nm, (e) d = 2000 nm, assuming a constant N-scattering MFP (λ_N) of 100 nm. Illustration of the effect of N-scattering on the effective boundary scattering for (f) d = 20 nm (g) d = 60 nm. The dashed circle represents the N-scattering MFP. Boundary scattering of phonons traveling along a direction in the red region is affected by N-scattering, while phonons in the green region are not affected. (h) A schematic of the random walk of phonons in a very wide (d = 2000 nm) sample.

To understand the microscopic mechanism of the effect of N-scattering on phonon transport, we compute and plot the contribution to the total heat flux by phonons moving in different directions at various sample widths (Figure 3-11c-e). In particular, we note that the MFP that affects the total thermal conductivity according to $k = \sum Cv\lambda$ should be regarded as the momentum-loss MFP, which characterizes the average distance that phonons travel before their momenta are randomized. In Figure 3-11c-e, θ is defined as the angle between the phonon propagating direction and the boundary normal direction, as indicated in Figure 3-11f. Phonons propagating parallel to sample boundaries are denoted by $\theta = 90^{\circ}$. When the sample width is much smaller than the dominant N-scattering MFP (Figure 3-11c), only phonons propagating almost parallel to sample boundaries are significantly affected by N-scattering, while most other phonons are not affected. More intuitively as shown in Figure 3-11f, for phonons starting from the center of the ribbon, if their propagating direction is within the green region, they are less affected by N-scattering because they reach the boundary before experiencing significant N-scattering (corresponding MFP denoted by the dashed circle). On the other hand, phonons propagating along the direction in the red region will be redirected by N-scattering. When they are redirected towards the boundary, the boundary scattering rate is effectively increased. In other words, their contribution to the sample thermal conductivity is suppressed due to N-scattering. Such suppression becomes more severe as the sample width becomes larger (Figure 3-11d), because more phonons (as indicated by the larger red region) are now affected by N-scattering before they reach the boundary (Figure 3-11g). This leads to the initial decrease of the dimensionless thermal conductivity with increasing sample width (Figure 3-11b). If we define the sample thermal conductivity without N-scattering as k^*, and the suppression ratio due to N-scattering as s, then the thermal conductivity with N-scattering can be expressed as $k = k^* / s$. As discussed earlier, k^* is proportional to d in the ballistic regime. Since s increases with increasing d based on the analysis of Fig. 5c-d, the thermal conductivity k should have a sublinear width dependence.

However, when the sample width becomes much larger than the N-scattering MFP, N-scattering processes can dramatically enhance the total thermal conductivity. Microscopically, this can be understood qualitatively from the picture of random walk.[37,98] When the sample width is much larger than the N-scattering MFP, each phonon experiences many N-scattering events before reaching the boundary. Because N-scattering conserves phonon momentum, the effective

momentum-loss MFP then corresponds to the summation of all the individual propagation paths that eventually lead the phonon to the sample boundary, since only at the boundary is the collective phonon drift momentum lost. During such a random walk, the velocity of a phonon is randomized at each N-scattering event. Consequently, the average time for phonons to traverse a certain distance then quadratically depends on the square of distance, leading to an effective relaxation time given by Gurzhi[97,98] as $\left(d/2\lambda_N\right)^2 \tau_N$. This is distinct from the ballistic regime, where the time needed for phonons to reach the boundary is linearly proportional to the sample size. Such a modified boundary scattering term underlies the superlinear width-dependent thermal conductivity, when sample is sufficiently wide and the transport is dominated by drifting phonons. Combined together, the existence of both a sublinear and a superlinear width-dependent thermal conductivity dictates the existence of a phonon Knudsen minimum.

3.6 From 2D to 3D

The noteworthy hydrodynamic feature in graphene has been attributed to its high Debye temperature, quadratic phonon band and diverging Grüneisen parameter.[2] Here, the Debye temperature can be interpreted as the maximum acoustic frequency and a high Debye temperature implies that, at typical temperatures of interest, most of the activated acoustic phonons are located near the Γ point, which tend to have high N-scattering rates. We found that all these three favorable features are preserved in graphite (Figure 3-12a-b), which contribute to its significant hydrodynamic behavior. This may be understood if we notice that the weak van der Waals interlayer interactions may not severely distort the lattice dynamics of individual graphene layers. However, we emphasize that the interlayer interactions do induce intriguing and unique features in graphite. First, the bending mode becomes stiffened in graphite (Figure 3-13) and opens up a gap at the long-wavelength limit. More importantly, the interlayer interaction breaks the reflection symmetry carried by a single graphene sheet.[102] This renders many originally forbidden phonon-phonon scattering channels in graphene (such as **BA** + **BA** <=> **BA**, due to the vanishing coupling matrix[102]) accessible in graphite, which accounts for the lower thermal conductivity of graphite compared to graphene at room temperature. However, at low temperatures, as the thermally activated phonons mostly have small in-plane wavenumbers, the newly opened scattering channels are mainly N-scattering processes and actually facilitate the hydrodynamic transport. This is observed in Figure 3-12 c-d and Figure 3-14, where comparisons between graphene and graphite

are made in terms of the average linewidths (Figure 3-12c), as well as the N- and R-scattering rates (Figure 3-14), with the average linewidths defined as

$$\langle \Gamma_i \rangle = \frac{\sum C\left(2\pi/\tau_i\right)}{\sum C} \quad (i = N, R) \tag{3-32}$$

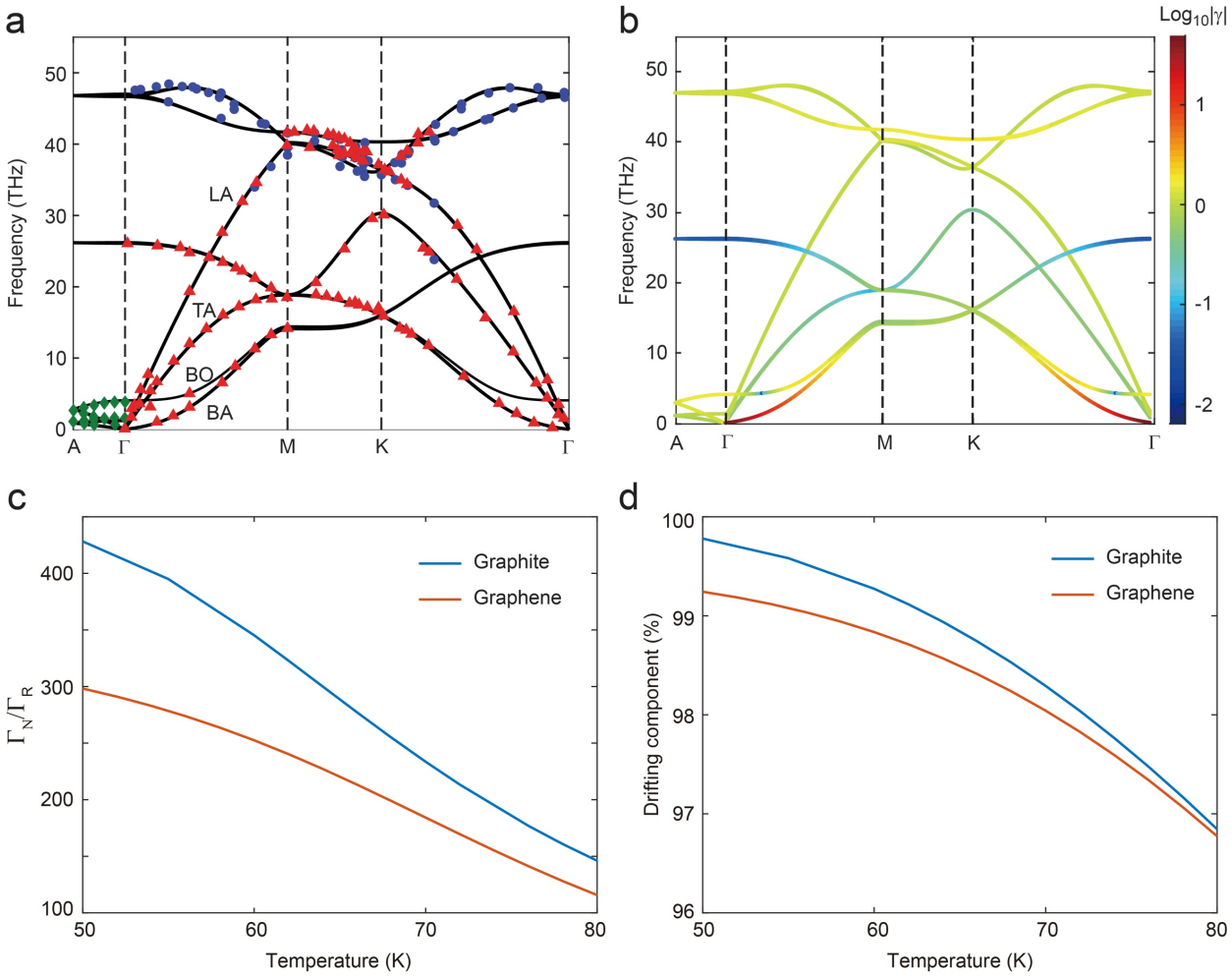

Figure 3-12 Comparison between graphite and graphene. Phonon band structure (a) and mode Grüneisen parameter (b) of graphite along the high symmetry lines. The blue circles are from Ref. [103], the red triangles are from Ref. [104], and the green squares are from Ref. [105]. (c) Ratio of average N-scattering and R-scattering linewidth. (d) Projection of the out-of-equilibrium phonon distribution onto the drifting distribution.

As a result, the collective phonon drift is more significant and accounts for a larger percentage of the total thermal conductivity in graphite

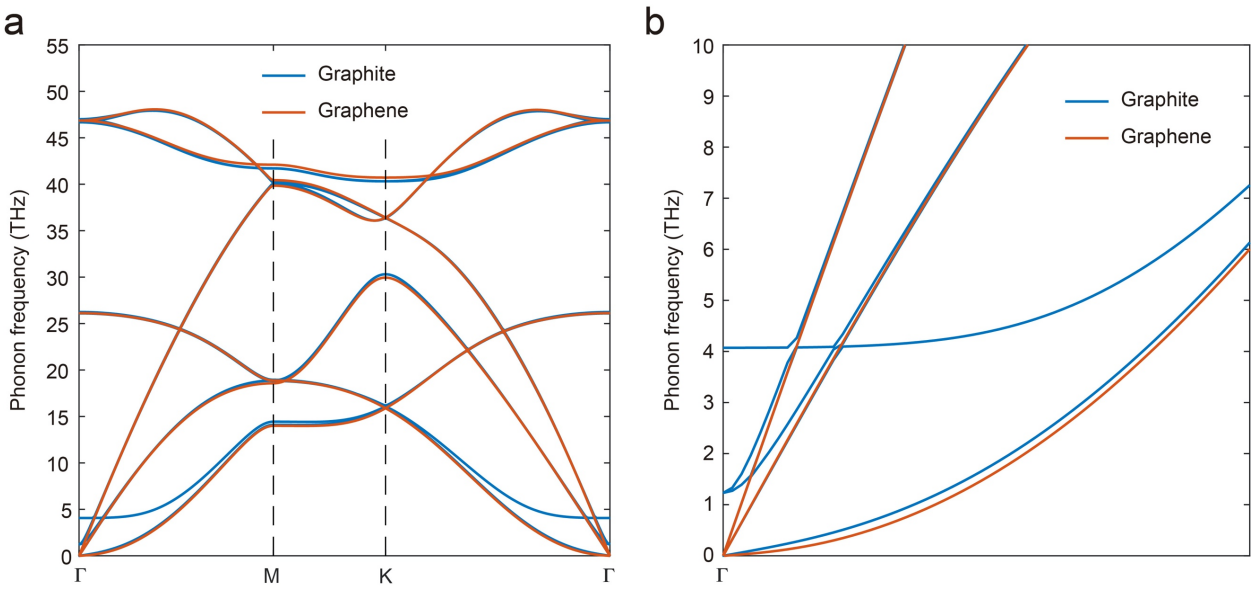

Figure 3-13 Comaprison of phonon band structure between graphene and graphite. (a) Phonon band structure. (b) Zoomed in near the Γ points

3.7 Concluding remarks

In conclusion, we predict that phonon hydrodynamic transport can occur in graphite at up to 100 K. As discussed in ref. [2], the significant hydrodynamic feature in graphene is attributed to its high Debye temperature, quadratic phonon band and diverging Grüneisen parameter. Here we predict that all the three favorable features are preserved in graphite due to the weak van der Waals interlayer interactions. More importantly, we demonstrate that the hydrodynamic nature of phonon transport in graphite can be even more pronounced than in graphene. This is because the interlayer interaction, although weak, breaks a selection rule on phonon-phonon scattering and creates more N-scattering channels, which facilitates hydrodynamic transport. Thus we extend the strong hydrodynamic transport in 2D materials[10] to its vdW layered family. By taking into consideration of phonon drift motion, we extend the classical size effect into the hydrodynamic regime. We found that though N-scattering does not induce resistance itself, it can enhance or reduce the

thermal conductivity by varying the effective boundary scattering rate. By solving the BTE for graphite ribbon, a superlinear size dependent thermal conductivity is predicted, which is a direct evidence of the phonon Poiseuille flow. Phonon Knudsen minimum in solids is predicted using a first principle calculation for the first time and a microscopic explanation is provided. Our results will hopefully stimulate further work into discovering novel material systems with significant phonon hydrodynamics, as well as new research into understanding and manipulating the phonon transport in the hydrodynamic regime.

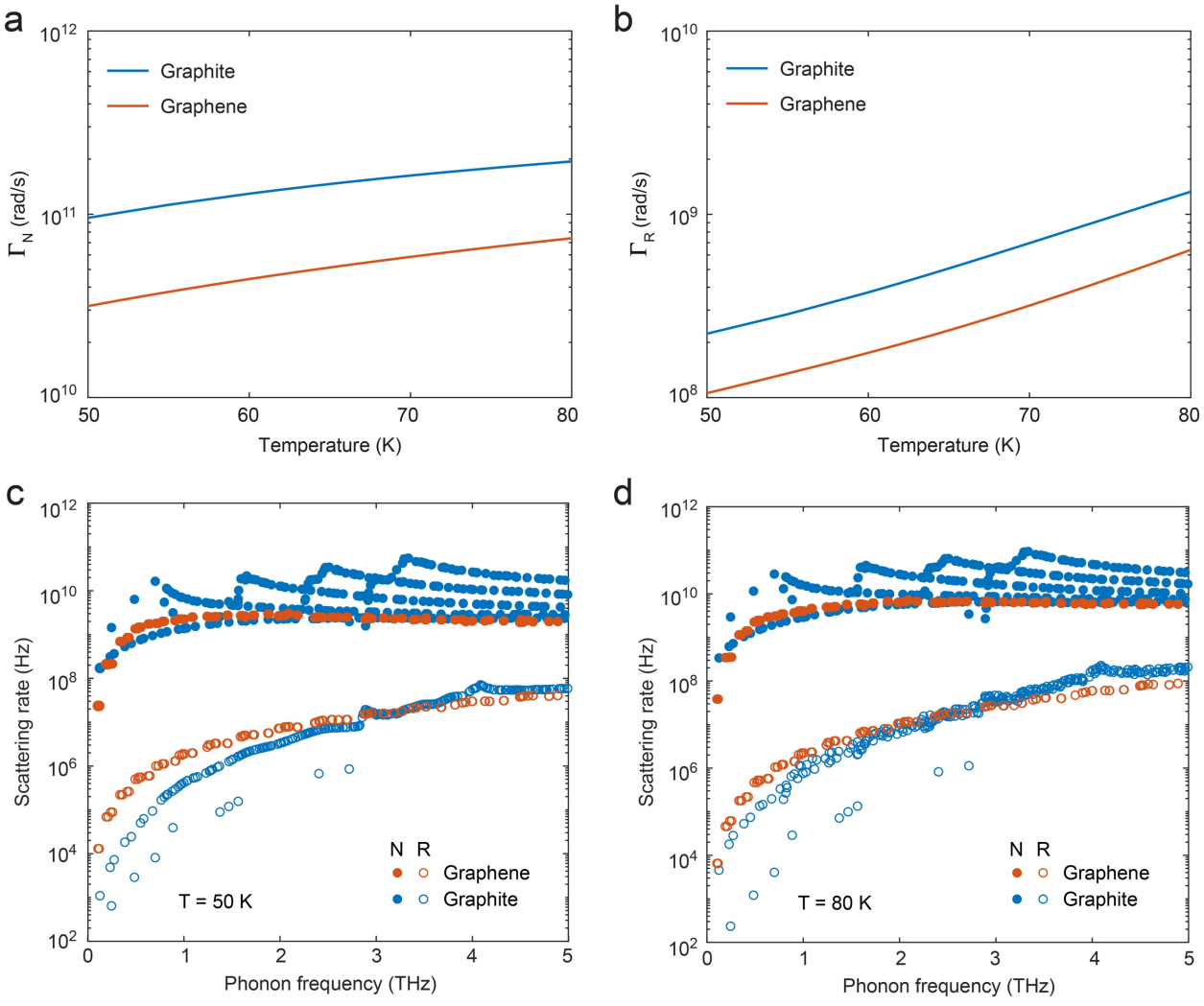

Figure 3-14 Comparison between graphene and graphite. Variation of average linewidth as a function of temperature in graphene and graphite: (a) N-scattering (b) R-scattering. Comparison of N-scattering rates and R-scattering rates in graphene and graphite at (c) 50 K and (d) 80 K

Chapter 4 Observation of Second Sound in Graphite over 200 K

Second sound refers to the phenomenon of heat propagation as temperature waves in the phonon hydrodynamic transport regime. Here, we directly observed second sound in graphite at record-high temperatures of over 200 K using a sub-picosecond transient grating technique. The experimentally determined dispersion relation of the thermal-wave velocity increases with decreasing grating period, consistent with first-principle-based solution of the Peierls-Boltzmann transport equation. Through simulation, we reveal this increase as a result of thermal zero sound—the thermal waves due to ballistic phonons. Our experimental findings are well explained with the interplay among "three fluids": ballistic, diffusive, and hydrodynamic phonons. Our ab initio calculations further predict a large isotope effect on the properties of thermal waves and the existence of second sound at room temperature in isotopically pure graphite.

4.1 Background

Thermal transport in dielectrics and semiconductors is often mediated by the random walk of phonons and follows Fourier's law of heat diffusion. However, Fourier's law breaks down at sufficiently small length scales and/or low temperatures, which lead to the unusual regimes of ballistic and hydrodynamic phonon transport. In the ballistic regime, phonons could travel a distance longer than the conduction length scale, leading to an effectively reduced thermal conductivity. Size effect in this regime has been studied extensively for its importance in applications such as electronics thermal management and thermoelectric energy conversion[66,68,106,107]. The hydrodynamic regime takes place when the momentum-conserving normal scattering (N-scattering) is stronger than the momentum-destroying resistive scattering (R-scattering), leading to a collective drift motion of phonons under a temperature gradient. This strongly correlated collective motion of phonons leads to peculiar thermal transport phenomena such as second sound[11,37,56,59,108–110], phonon Poiseuille flow[2,12,37] and Knudsen minimum[3,12], parallel to the hydrodynamic regime of strongly correlated electrons[63,111–113]. For over half a

century, phonon hydrodynamic transport was deemed exotic and mattered only at extremely low temperatures. However, phonon hydrodynamics at substantially higher temperatures in low-dimensional and van der Waals materials has recently been theoretically predicted and experimentally observed, stimulating renewed interest, especially in second sound[2,12,49,50,114–117].

Second sound is the wavelike propagation of heat as opposed to diffusion[118]. First observed by Peshkov in 1944 in superfluidic ^{3}He at 1.4~1.6 K[119] and explained with Landau's two-fluid model[120], it was later predicted to exist also in solids when phonon-phonon N-scattering dominates over R-scattering[56]. Experimentally, second sound in solids was initially observed via heat-pulse methods near liquid-helium temperatures, for example, at 1.2~4.0 K in Bi[121] and 10~18 K in NaF[122]. Some of us recently reported observation of second sound around 100 K in graphite using the transient thermal grating (TTG) technique[116]. However, the temporal resolution of our continuous-wave-laser-probed TTG system (0.5 ns) prevented further reduction of the grating period where second sound is expected at even higher temperatures.

Theoretically, phonon-mediated second sound is described as damped temperature waves derived either from the phonon Peierls-Boltzmann transport equation (PBTE)[11,37,59,109] or equilibrium correlation functions[40,110]. In particular, the dispersion of second sound has been discussed by applying a temperature perturbation to the PBTE[109] and analytically solving the transport equation for the quasi-momentum auto-correlation function[110]. However, all these efforts focus on the frequency windows to observe second sound, while the wavevector dependence of the second-sound velocity, i.e., the dispersion of the velocity, has not been discussed.

While second sound originates from phonons in local thermal equilibrium caused by strong normal scattering (a drifted equilibrium)[37], ballistic phonons can also generate a wavelike signal of heat flow, as was evident in past experiments on NaF and Bi[121,122], in which heat pulses due to the ballistic longitudinal and transverse phonons reach the detectors before the emergence of the second sound. These thermally excited phonons were mistakenly attributed to the first sound, but it was shown[123] that thermal excitation cannot excite a mechanical wave of large amplitude, and

vice versa. The mechanically excited first sound could be damped by phonons in local equilibrium via the Landau-Rumer[124] and the Akhiezer mechanisms[125], because the wavelength of the first sound is much larger than the phonon thermalization length. If the mean free path (MFP) of phonons is longer than the wavelength of the first sound, it was called zero sound, in analogy to the propagation of zero sound waves across a Fermi liquid in the ballistic limit[126–129]. In analogy to the zero sound for mechanical sound wave, we call the ballistic thermal wave the thermal zero sound. In the heat-pulse experiments[121,122], phonons are excited into all directions by the heater, but only those propagating within a small solid angle subtended by the detector are recorded, leading to thermal zero-sound velocities close to those of the longitudinal and transverse phonons. Oscillations due to thermal zero sound were also seen in solving PBTE under constant MFP approximation for the TTG experimental geometries[130].

In this chapter, we report the observation of second sound at record-high temperatures of over 200 K via pulsed-laser-probed TTG measurements at grating periods around 2 μm. However, this second sound also includes contributions from thermal zero sound of ballistic phonons. We show that the transport can be viewed as a mixture of "three fluids": the hydrodynamic phonons experiencing strong normal scattering contributing to the second sound, the ballistic phonons contributing to the thermal zero sound, and the resistive phonons diffusing along the temperature gradient. Using exact solutions of the PBTE, we demonstrate the increasing contributions of the thermal zero sound to the TTG signal with decreasing grating period. We also predict a large isotope effect on the second sound. Notably, room-temperature second sound is expected in isotopically enriched graphite.

4.2 Observation of second sound in graphite above 200 K

As discussed in Ref. [116], second sound can be observed in graphite via transient thermal grating (TTG) measurement at around 100 K. However, the time resolution of the continuous-wave (CW) probe laser prevents further reduction of the grating period where second sound is expected at much higher temperatures. In this work, we replace the CW-laser with a femtosecond pulsed-laser using standard pump-probe time-delay detection technique[131,132]. To capture the fast dynamics of

second sound at micrometer transport length, we employ femtosecond laser pump-probe spectroscopy. The schematic of our femtosecond laser thermal transient grating experimental setup is shown in Figure 4-1. Ultrafast laser pulses with 290 fs pulse width, 515 nm and 532 nm wavelength, are generated by a second harmonic generator and an optical parameter amplifier, respectively. The repetition rates of the laser pulses are both 25 KHz. The 515 nm laser is used as pump, the 532 nm one is use for detection. The pump laser is modulated by an optical chopper working at frequency around 2 KHz, and directed into a delay stage, which can cause up to 16 ns time delay between the pump and the detection pulses. Two laser beams cross vertically at a phase mask, which diffracts the laser into +1 and -1 orders. Lens 1 locates away from the phase mask by one of its focal length and collects the +1 and -1 order diffractions. The +1 order of the detection laser is taken as reference beam, and its intensity is reduced by an attenuator made of a 100 nm Au film coated on a 170 μm-thick glass slide. The -1 order of detection laser is taken as the probe beam. One 170 μm-thick glass slide mounted in a rotor is inserted in the light path of probe beam to adjust the heterodyne phase shift between the probe and the reference laser by rotating its angle. Two pumps, the reference, and the probe are collected by Lens 2 and focused onto the surface of a natural graphite sample sitting in a cryostat chamber, with spot size of 120 μm $1/e^2$ diameter for pumps and 105 μm $1/e^2$ diameter for probe and reference. The two pumps interfere with each other and generate transient thermal grating in the graphite sample. The probe pulse is diffracted by the transient thermal grating, and the diffraction coincides with the reflection of the reference pulse, both spatially and temporally. After passing through Lens 2, probe diffraction and reference reflection are directed by a mirror and collected by a photo detector as the heterodyned transient thermal grating diffraction signal. The output of the photo detector is analyzed by a lock-in amplifier which is synchronized with an optical chopper. Pump pulse energy is set at 70 nJ, while the probe pulse energy is set at 52 nJ. By the time the second sound signal is observed, the average temperature rise due to the pump is estimated to be less than 3 K.

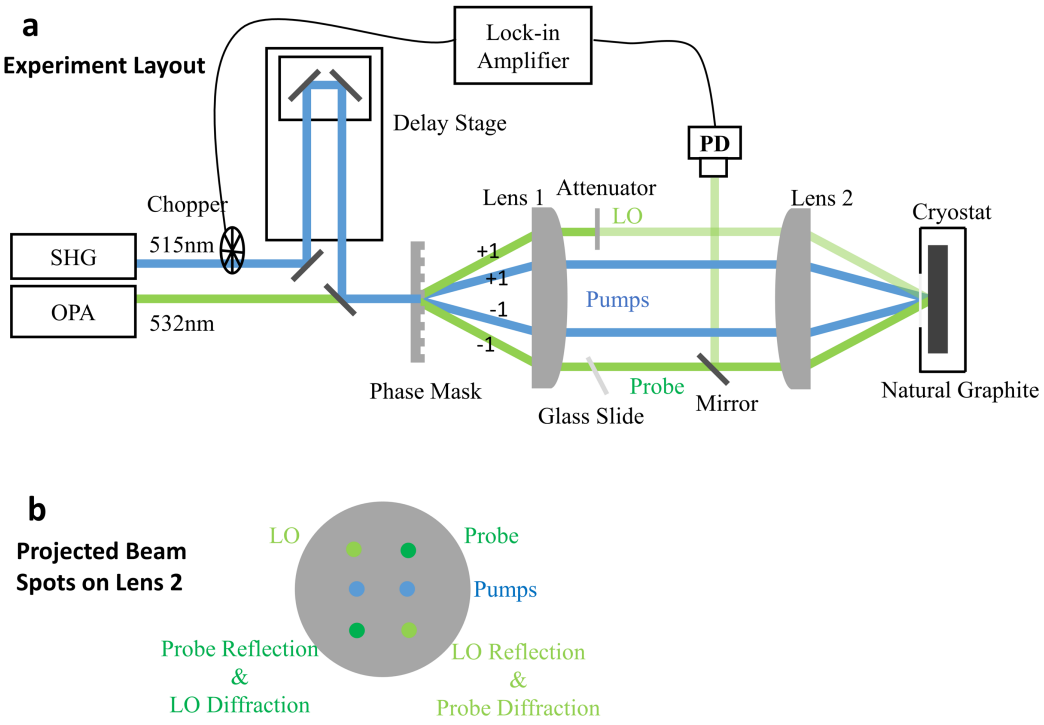

Figure 4-1 Schematic of the femtosecond laser TTG setup. (a) Top view. The difference in the diffracted angle after the phase mask between the 515 nm and the 532 nm laser beams is exaggerated for better drawing. (b) Side view

Following the Green function approach developed by Chiloyan et al.[133], we also simulate the TTG response using first-principle calculations with no fitting parameters. All the calculation are based on the temperature response with an arbitrary heating profile derived in Ref.[133]. Here we briefly recap its derivation.

Start with PBTE:

$$\frac{\partial f_\mu}{\partial t} + \overrightarrow{\mathbf{v}_\mu} \cdot \nabla f_\mu = Q_\mu \frac{N_v}{\hbar \omega_\mu} + \sum_\nu W_{\mu\nu}(f_\nu^0 - f_\nu) \tag{4-1}$$

where μ is a short hand index for a given phonon mode (branch and wavevector in the Brillouin zone), ω_μ is the frequency of the given phonon mode, f_μ is the non-equilibrium distribution. function, f_μ^0 is the equilibrium distribution function, which is given by the Bose-Einstein function. W is the phonon scattering matrix.

Write the Eq. in terms of deviational phonon energy density:

$$\frac{\partial g_\mu}{\partial t} + \overrightarrow{\mathbf{v}_\mu} \cdot \nabla g_\mu = Q p_\mu + \sum_\nu \frac{\omega_\mu}{\omega_\nu} W_{\mu\nu}(c_\nu \Delta T - g_\nu) \tag{4-2}$$

where $g_\mu = \frac{\hbar\omega_n}{N\nu}\left[f_\mu - f_\mu^0(T_0)\right]$ and the volumetric heat generation rate Q_μ, is replaced by Qp_μ, where Q is the macroscopic volumetric heat generation rate, and p_μ corresponds to how much a given mode is excited by the heating. We assume initial heating is thermally distributed, i.e. $p_\mu = c_u/C$, where $C = \sum_\mu c_\mu$ is the heat capacity.

Take the spatial and temporal Fourier transform of Eq. (4-2):

$$\widetilde{g_\mu} = \tilde{Q} A_{\mu\nu}^{-1} p_\nu + \Delta\tilde{T}\left(\delta_{\mu\nu} - i A_{\mu\gamma}^{-1} D_{\gamma\nu}\right) c_\nu \tag{4-3}$$

where dummy index indicates summation as in Einstein notation, i.e. $a_\mu b_\mu = \sum_\mu a_\mu b_\mu$, with $D_{\mu\nu} = \delta_{\mu\nu}\left(\Omega + \vec{k} \cdot \overrightarrow{v_\mu}\right)$ and $A_{\mu\nu} = \frac{\omega_\mu}{\omega_\nu} W_{\mu\nu} + i D_{\mu\nu}$. It should be noticed that Ω and $\vec{k}$ represent the frequency and wavevector from the Fourier transform

Sum the Eq. (4-3) over all the phonon modes and express the deviation temperature as:

$$\Delta\tilde{T} = \sum_\mu \frac{\widetilde{g_\mu}}{C} \tag{4-4}$$

We obtain a general expression for temperature response for heating with frequency Ω and wavevector $\vec{k}$ as:

$$\Delta\tilde{T}(\Omega,\vec{k}) = \tilde{Q}(\Omega,\vec{k})\frac{\mathrm{sum}[\mathbf{A}^{-1}\vec{p}]}{\mathrm{sum}[i\mathbf{A}^{-1}D\vec{c}]} \tag{4-5}$$

where we define the sum operation of a vector to add up the values of its elements, i.e. $\mathrm{sum}[\mathbf{a}] = \sum_{\mu} a_{\mu}$.

To obtained temperate response of TTG measurement with grating period l, we need to substitute the following heating profile and take inverse Fourier transform:

$$\tilde{Q}(\Omega,\vec{k}) = \delta\left(\frac{2\pi}{l}\right) + \delta(-\frac{2\pi}{l}) \tag{4-6}$$

As demonstrated in the simulated TTG signal (Figure 4-2a), second sound is characterized by the flip of sign in the grating response[116], which arises when the phase of the temperature wave differs from the reference by π. The strength of the wavelike feature can be measured by the ratio of the dip depth to the peak height. Using the normalized dip depth as the metric for the strength of the wavelike effect, the second-sound windows are shown in Figure 4-2b with the experimental observations indicated by the markers. Considering the limitation of sample quality and experimental challenge, the line of normalized depth 0.05 can be considered as the boundary to experimentally observe second sound. TTG signals often contain oscillations due to surface acoustic waves (SAWs), which have much lower damping rates. We found that the SAW signal could be mitigated by maximizing the signal peak height via adjusting the phase as discussed in SM1. At 250 K (Figure 4-2c), the sign flip is inundated by the SAW due to the relatively low signal-to-noise ratio. But the clear hallmark of second sound is observed at 200 K (Figure 4-2d) and 225K (Figure 4-4a). Second-sound windows (Figure 4-2b) indicates that second sound can be

observed at longer grating period at lower temperature, which is consistent with the experimental observation at 100 K (Figure 4-2e). A larger discrepancy between the experiment and simulation is observed at 100 K (Figure 4-2e) than 200 K (Figure 4-2f). This might result from the increased importance of impurity scattering at lower temperature compared with phonon-phonon scattering. At 100 K (Figure 4-2f), about 0.02% of vacancy defect could explain the discrepancy between simulation and experiments, while the simulated response with the same level of defect showed much smaller variation at 200 K (Figure 4-5).

4.3 Dispersion of measured thermal wave

For a damped wave, the propagation speed v_p and propagation length l_p could be estimated based on the dip position and depth as (Figure 4-2a):

$$v_p = \frac{l}{2t_d} \tag{4-7}$$

$$l_p = \frac{l}{-2\ln(-T_d)} \tag{4-8}$$

where l is the grating period and t_d is the dip position, which is the time duration it takes for the thermal wave to travel from the high temperature region to the low temperature region (half of the grating period); T_d is the temperature response at the dip bottom. For exponentially decaying wave, the amplitude after traveling $l/2$ is reduced to $\exp(-l/2l_p)$, which gives (4-8). Using (4-7), we can determine the thermal wave propagation velocity and propagation length from both experimental and simulated temperature responses.

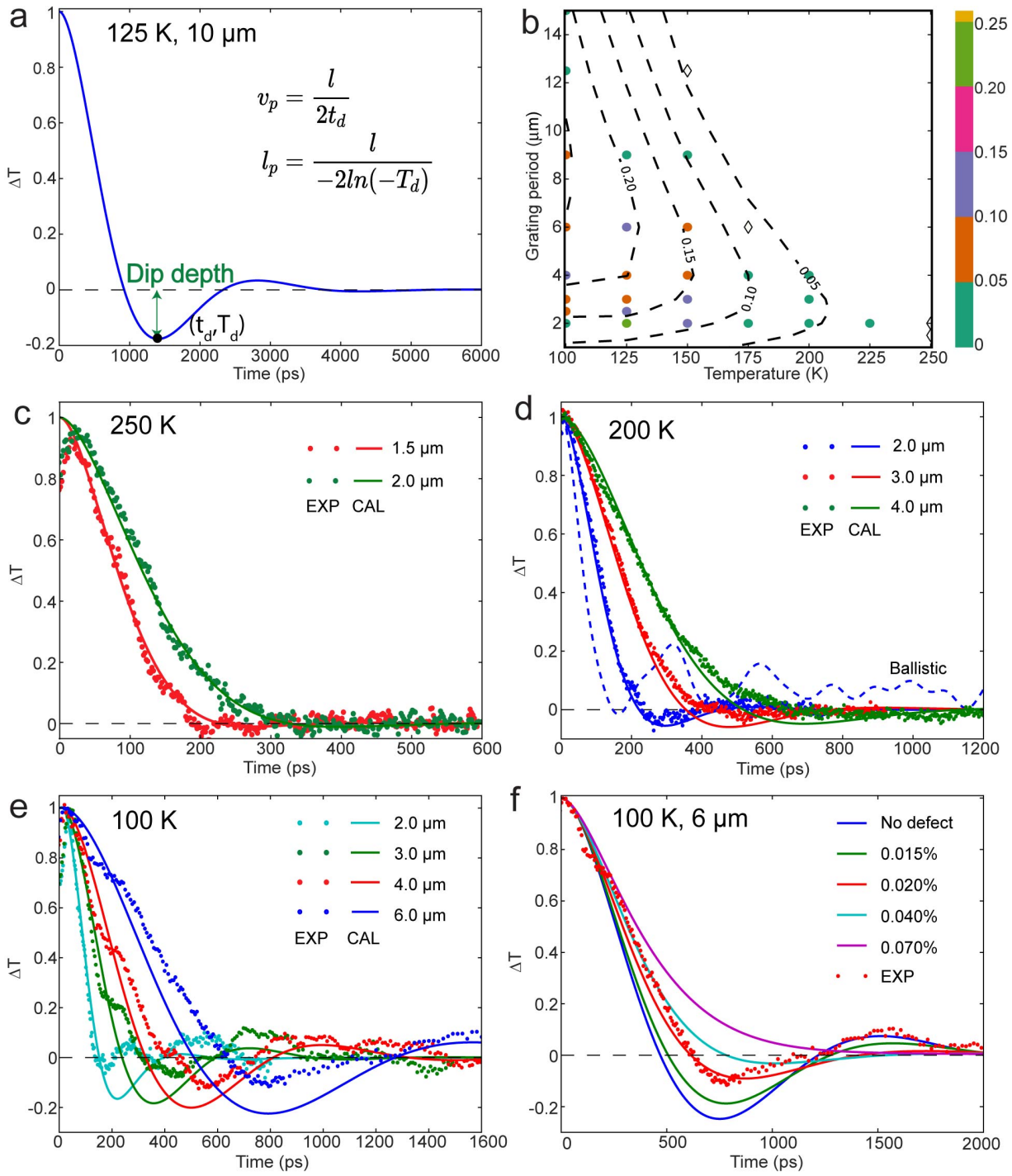

Figure 4-2 Measured (markers) and simulated (curves) TTG signals for graphite after normalization with respect to the peak height. (a) The simulated temperature response at 125 K with a 10 μm grating period. The negative dip is the hallmark of thermal wave and its depth represents second-sound strength. (b) Second-sound window. The color bar shows the normalized dip depth. The circles (diamonds) indicate success (failure) to observe thermal waves. TTG signals at (c) 250 K, (d) 200 K, and (e) 100 K for various grating periods. (f) The effect of vacancies on the TTG signal.

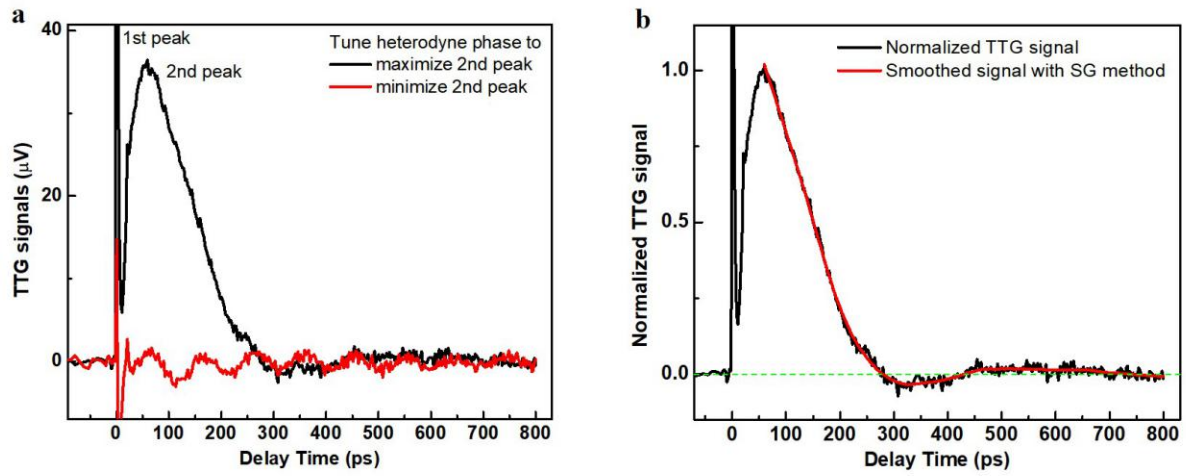

Figure 4-3 (a) Measured TTG signals at 200 K 2um grating period under two heterodyne phases. One phase is set to maximize the 1st peak, while the other phase is set to minimize the 2nd peak, corresponding to the phase grating signal and the amplitude grating, respectively. (b) Normalized phase grating signal and its smoothed data using the Savitzky-Golay method.

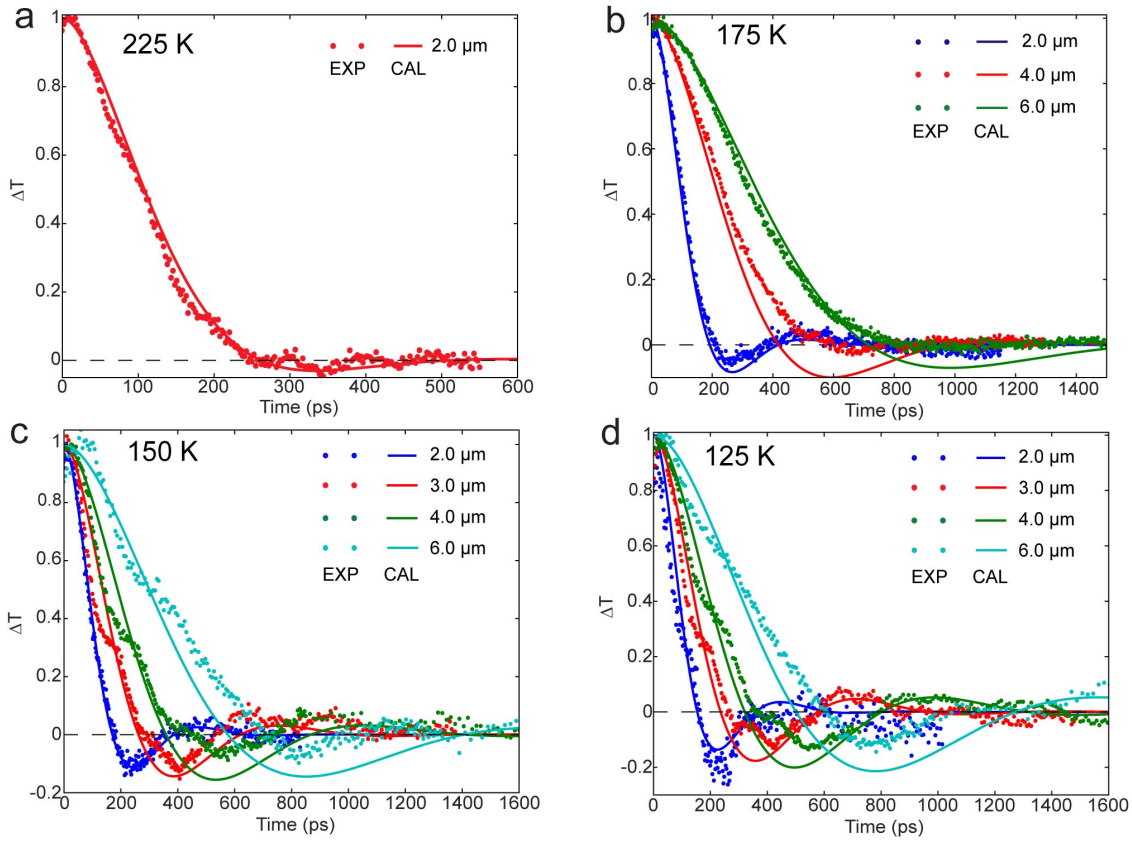

Figure 4-4 Temperature response of TTG at (a) 225K (b) 175K (c) 150K. (d) 125K.

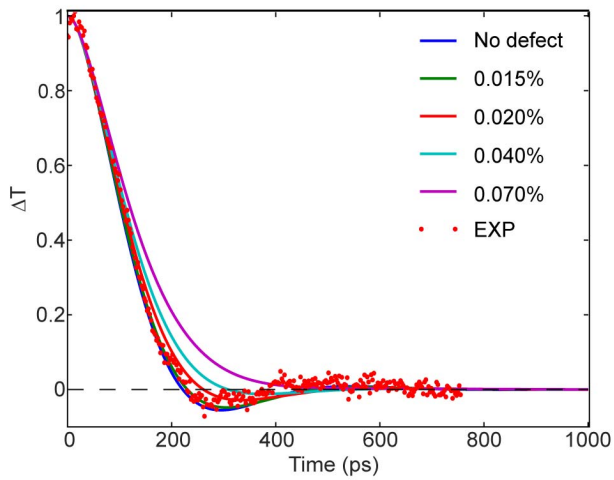

Figure 4-5 TTG temperature response with the existence of vacancy defects at 200 K with grating period 2μm. Dot are the experimental collected data and curves are the calculations.

The wave propagation velocity and propagation length at different temperatures and grating periods from TTG temperature response are shown in Figure 4-6a and Figure 4-6b, which show qualitative agreement between simulation and experimental results. We attribute the discrepancy between experiments and simulation to the defects in graphite. As discussed in Refs.[134], using the energy and momentum conservation equations derived from the PBTE with the Callaway model [8], the second sound velocity v_{ss} and propagation length l_{ss} in the x-direction can be written as:

$$v_{ss}^2 = \frac{\langle \frac{C_q q_x v_x}{\omega_q} \rangle^2}{\langle \frac{C_q q_x^2}{\omega_q^2} \rangle \langle C_q \rangle} \tag{4-9}$$

$$l_{ss} = \frac{2 v_{ss} \langle \frac{C_q q_x^2}{\omega_q^2} \rangle}{\langle \frac{C_q q_x^2}{\omega_q^2 \tau_{qR}} \rangle} \tag{4-10}$$

where < > means summation over all the phonon modes, C_q, q_x, v_x, ω_q, and τ_{qR}^{-1} are mode-specific heat capacity, wavevector, group velocity, frequency, and R-scattering rate, respectively.

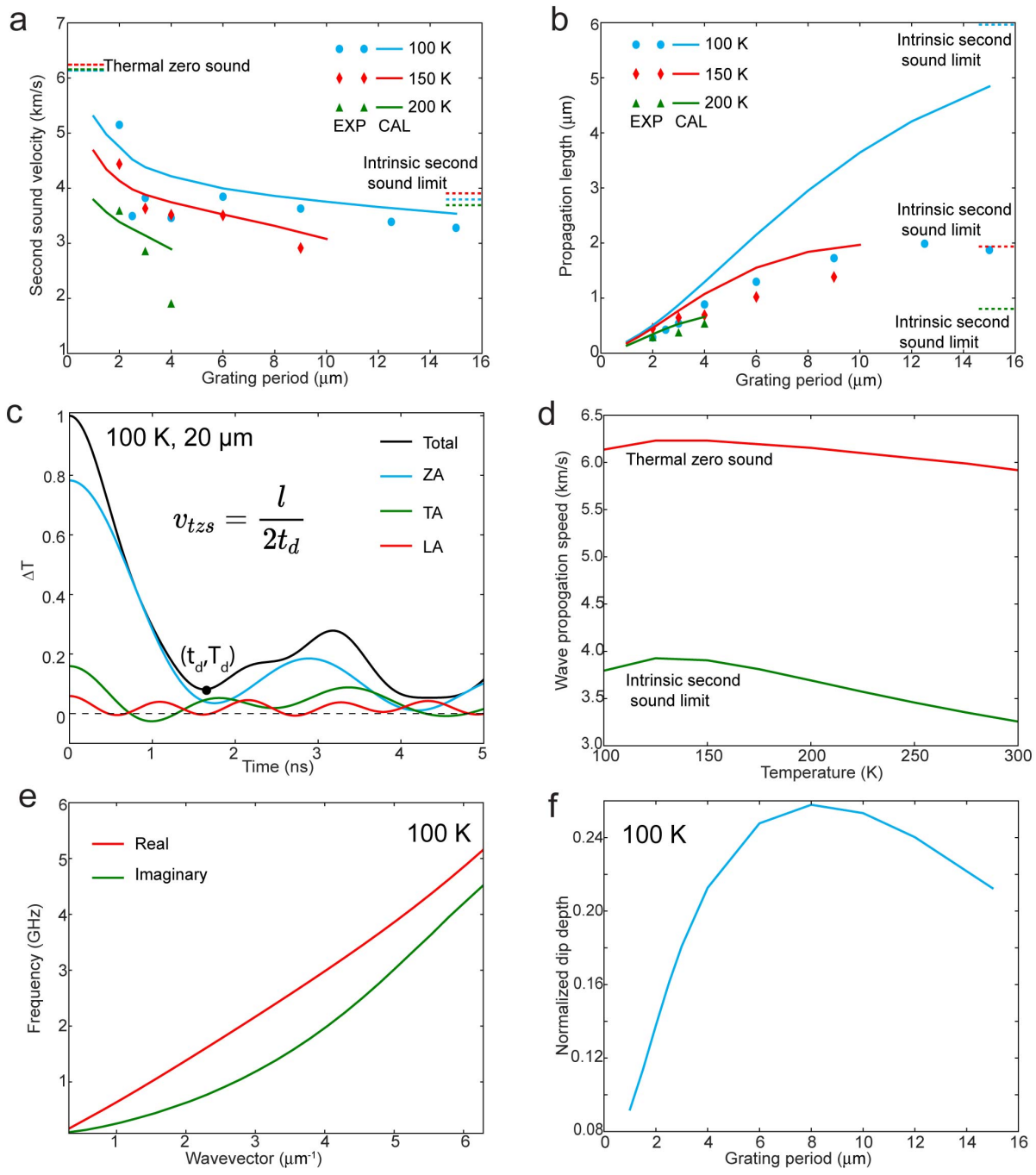

Figure 4-6 Dispersion of thermal waves. The measured and calculated data are represented by markers and curves, respectively. (a) Dependence of wave velocity on grating period. Also shown are the intrinsic second sound limit from Eq. (2) and the thermal zero sound limit as discussed in Methods. Damping reduces the second sound velocity below the intrinsic limit at large grating periods, while zero sound increases the measured wave velocity at small grating periods. (b) Propagation length variation with grating period at different temperatures. (c) Ballistic limit of the TTG signal at 100 K. (d) Variation of the ballistic and intrinsic second sound limits with temperature. (e) Dispersion of second sound. (f) Variation of the normalized dip depth with grating period.

We refer to the second-sound velocity and propagation length obtained from Eq. (4-7) and (4-8) as the intrinsic limits. To further understand the dispersion of the measured wave propagation velocity, we also simulated the TTG temperature response at the ballistic limit, where phonons propagate without interactions.

The 1D-PBTE at ballistic limit for TTG could be write as:

$$\frac{\partial \mathrm{f}}{\partial t} + v_x \frac{\partial f}{\partial x} = 0 \tag{4-11}$$

with initial condition:

$$f_o(x) = f_A \cos(qx) \tag{4-12}$$

where q=$\frac{2\pi}{l}$ with l being the grating period, f_A is the amplitude of the initial distribute due to the laser heating. If initial heat is thermally distributed, then $f_A = \frac{C_q Q}{\hbar\omega<C_q>}$, where Q is the total heating.

Then the distribution at $t \geq 0$ is:

$$f(x,t) = f_o(x - v_x t) = f_A \cos[q(x - v_x t)] \tag{4-13}$$

Then the measured TTG signal, i.e. the temperature difference between $T(x = 0)$ and $T(x = l/2)$, can be written as:

$$\Delta T = \frac{< f(0,t)\hbar\omega >}{< C_q >} - \frac{< f\left(\frac{l}{2},t\right)\hbar\omega >}{< C_q >} = 2Q\frac{\langle C_q \cos\left(\mathrm{qv_x t}\right)\rangle}{\langle C_q \rangle} \tag{4-14}$$

Wavelike behaviors due to the thermal zero sound are also observed in the investigated temperature range in the ballistic regime (Figure 4-6c and Figure 4-7), although the wave contains multiple frequencies from different polarizations. A similar wave propagation velocity could be defined based on the position of the first dip, which is referred as thermal zero sound velocity. The thermal zero sound is faster than the intrinsic second sound speed at all the investigated temperatures (Figure 4-6d) as expected, because the second sound involves mixing and scattering of different phonons to approach a local thermal equilibrium[37,59]. We can also consider longitudinal and transverse waves separately as these waves do not interact in the ballistic limit, as plotted in Figure 4-6c. At 100 K, the flexural mode dominates the signal and its superposition with longitudinal and transverse waves leads to higher thermal zero sound velocity. Both second sound velocity obtained from Eq. (4-9) and thermal zero sound velocity increase from 100 K to 125K first, and then start to decrease (Figure 4-6d). However, the group velocity of the measured thermal wave, which includes both second sound and thermal zero sound, at fixed grating period monotonically decreases with increasing temperature (Figure 4-6a and Figure 4-8a). As the grating period decreases, the measured wave propagation speed increases from the bulk second sound velocity to the thermal zero sound propagation speed (Figure 4-6a). On the other hand, the measured propagation length increases at longer grating period (Figure 4-6b) because of the reduced contributions of ballistic phonons with effective propagation lengths limited by the grating period.

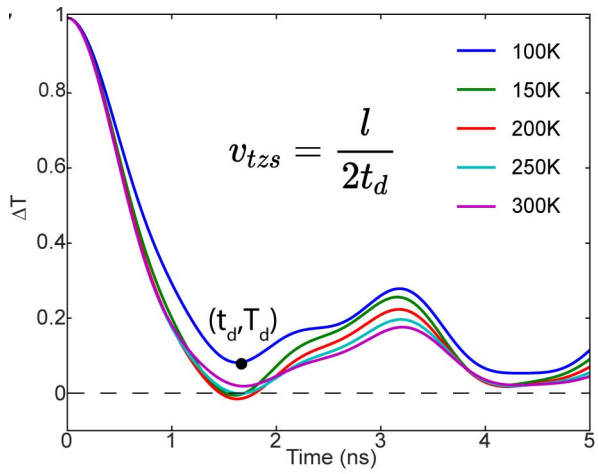

Figure 4-7 Ballistic limit of the TTG response signal at different temperatures.

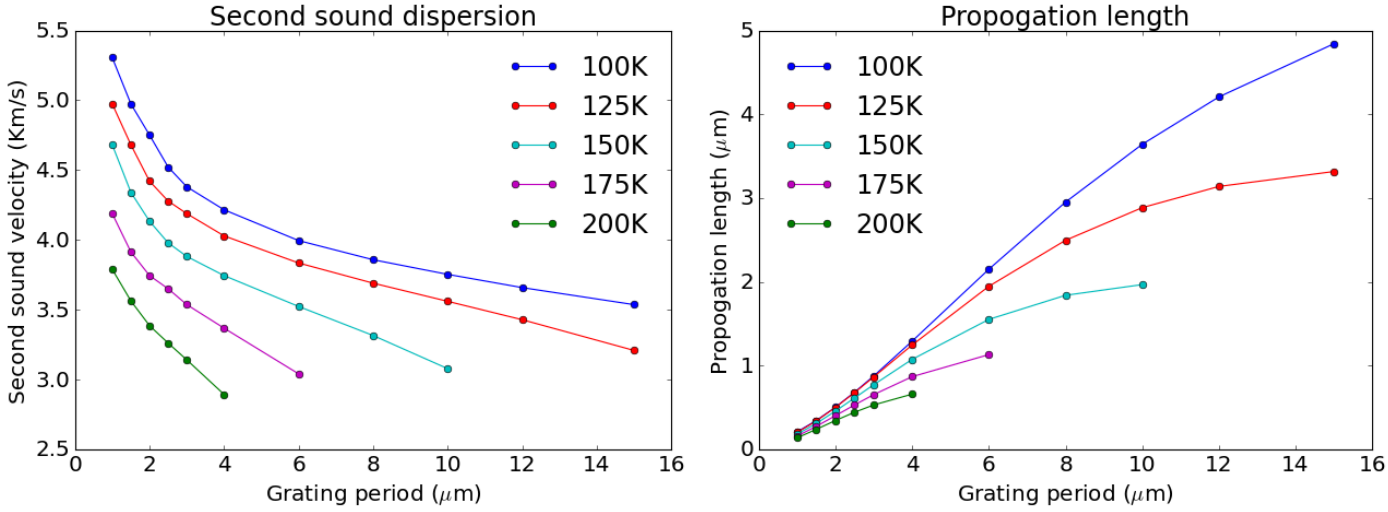

Figure 4-8 Variation of (a) second sound speed and (b) propagation length with grating period at different temperature.

For a damped temperature wave with wavevector $k = \frac{2\pi}{l}$ and frequency Ω_r and decay rate Ω_i, the temperature could be written as:

$$T(x,t) = \exp(-\Omega_i t)\cos(\Omega_r t - kx) \quad (4\text{-}15)$$

The TTG measure signal ΔT is proportional to the temperature difference between $T(0,t)$ and $T(l/2,t)$:

$$\Delta T(t) = \exp(-\Omega_i t)\cos(\Omega_r t) \tag{4-16}$$

The comparison of Eq. (4-16) with the measured TTG signal is shown in

The Fourier transform is:

$$\Delta T(\omega) = \frac{1}{\Omega_i + i(\omega - \Omega_r)} + \frac{1}{\Omega_i + i(\omega + \Omega_r)} \tag{4-17}$$

This is sharply peaked near Ω_r; near this frequency, we could ignore the second term in Eq. (4-17) as its magnitude is much smaller than the first term, frequency spectrum can be approximated as:

$$|\widetilde{\Delta T}(\omega)|^2 \approx \frac{1}{\Omega_i^2 + (\omega - \Omega_r)^2} \tag{4-18}$$

Therefore, the frequency of the temperature wave could be obtained by Lorentzian fitted with the temperature response function at certain wavevector given by Eq. (4-5) as shown in Figure 4-9.

The measured grating-period-dependent wave propagation speed indicates a convex dispersion, which is consistent with the calculated dispersion. In addition, the gap between the real and imaginary part of the frequency is maximized at mid-wavevector, which is consistent with the trend of the second-sound strength metric (i.e. normalized dip depth) we defined (Figure 4-6f).

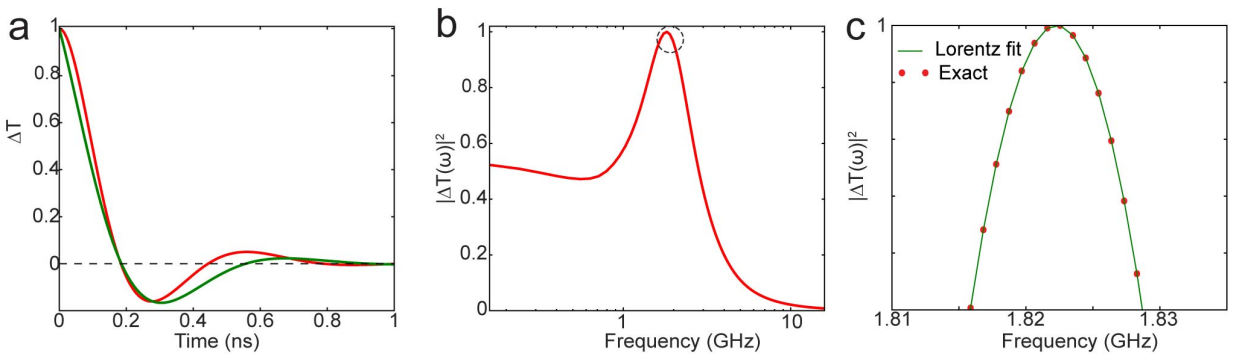

Figure 4-9 (a) Comparison of the damped temperature wave and exact signal (b)The Frequency spectrum (C) The Lorentz fitting to obtain the real part and imaginary part of the temperature wave.

4.4 Three-fluid model

Phonons participating in the transport are mixture of those experiencing N-scattering, ballistic transport, and R-scattering[135]. The observed thermal wave is a superposition of ballistic, diffusive and hydrodynamic phonons. The dispersion of the measured thermal waves and temperature-dependent characteristic can be understood with this "three-fluid" models, i.e. ballistic phonons, diffusive phonons and hydrodynamic phonons. To qualitatively describe how much ballistic/diffusive component are contributing to the measured thermal waves, we calculate the fraction of the initially excited phonons with traveling distance shorter/longer than the corresponding mean free path as:

$$f_b = \frac{< C_q \mathrm{v_x^2}\, f_b^q(\Lambda_o, d) >}{< C_q v_x^2 >} \tag{4-19}$$

$$f_d = \frac{< C_q \mathrm{v_x^2}\, f_d^q(\Lambda_R, d) >}{< C_q v_x^2 >} \tag{4-20}$$

where d is the traveling distance, and Λ_o and Λ_R are the total and resistive MFP, respectively. $f_{b/d}^q$ is the ballistic/diffusive contribution function for phonon mode q. The TTG

measure signal ΔT is proportional to the temperature difference between $T(0)$ and $T(l/2)$. All the TTG signals coming from the initial excited phonon, which has a spatial cosine distribution. For phonon with positive group velocity excited at x, the distance d it travels to reach $\frac{l}{2}$ is $\frac{l}{2} - x$. Whether the contribution is from ballistic or diffusive is determined by the relationship between d and the total MFP Λ_o and R-scattering Λ_R. If $\Lambda_R < d$, then it is diffusive transport. If $\Lambda_o > d$, then it is ballistic. Therefore, the ballistic/diffusive components contributing to the measured wave are proportional to the pink/green area in Fig. S8a respectively. The variation of the mode ballistic or diffusive contribution to the TTG signal with respect to MFP are shown in Figs. S8b and S8c. Sum over all the phonon modes with weights $c_q v_x^2$, we obtain Figure 4-10a and Figure 4-10b in the main text. It should be noticed that this is not a rigorous estimation of the ballistic/diffusive contribution, but it should be qualitative reliable. Figure 4-11a and Figure 4-11b shows the fractions of diffusive and ballistic phonons so defined at different grating periods and temperatures.

Figure 4-11c shows the TTG response when hydrodynamic and diffusive phonons co-exist. The diffusive transport leads to an exponentially decaying TTG signal. The superposition of dominantly hydrodynamic phonons with some diffusive phonons still look like a damped temperature waves but with slower effective propagation speed and smaller dip depth. On the other hand, Figure 4-11d shows that the existence of some ballistic phonons modifies the dominant second sound signal to higher speed and also smaller dip. These trends are summarized in Figure 4-11e for velocity changes and Figure 4-11f for the dip changes with changing mixing ratio. The dispersion of the measured wave property and its variation with temperature and isotope reported in the previous section could be interpreted with this three-fluid model.

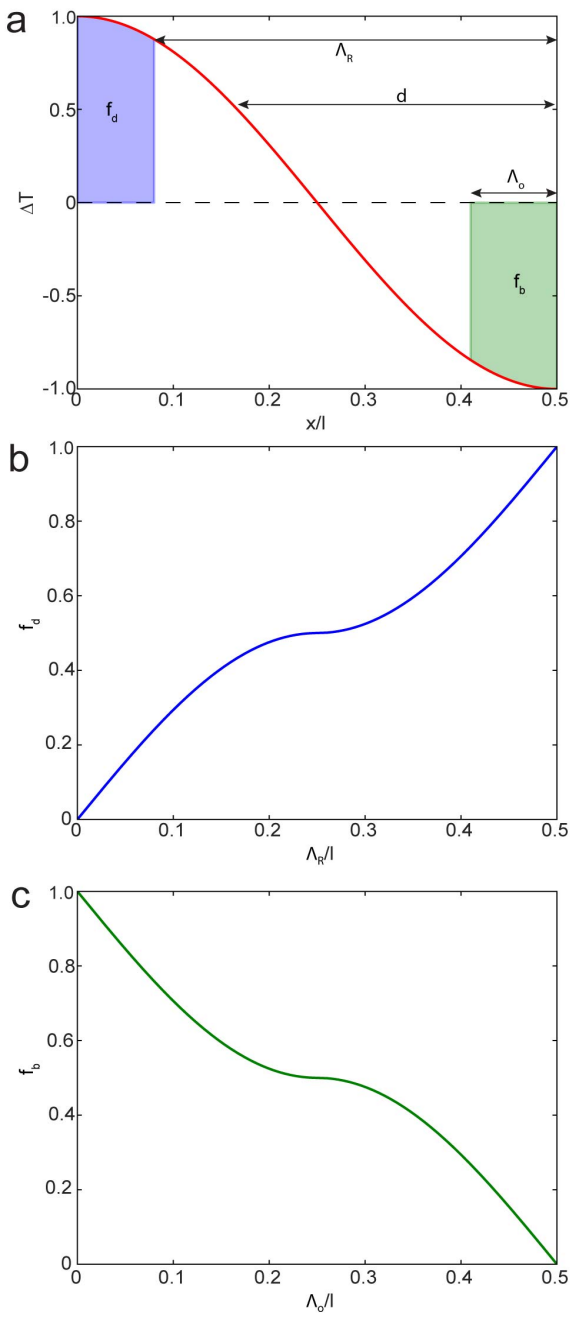

Figure 4-10 (a) Diffusive and ballistic contribution to the TTG signal of phonon mode with positive group velocity, (b) Variation of the mode diffusive contribution to the TTG signal with respect toR-scattering MFP to grating period l ratio, Λ_R/l, (c) Variation of the mode diffusive contribution to the TTG signal with respect to total MFP to grating period ratio, Λ_o/l.

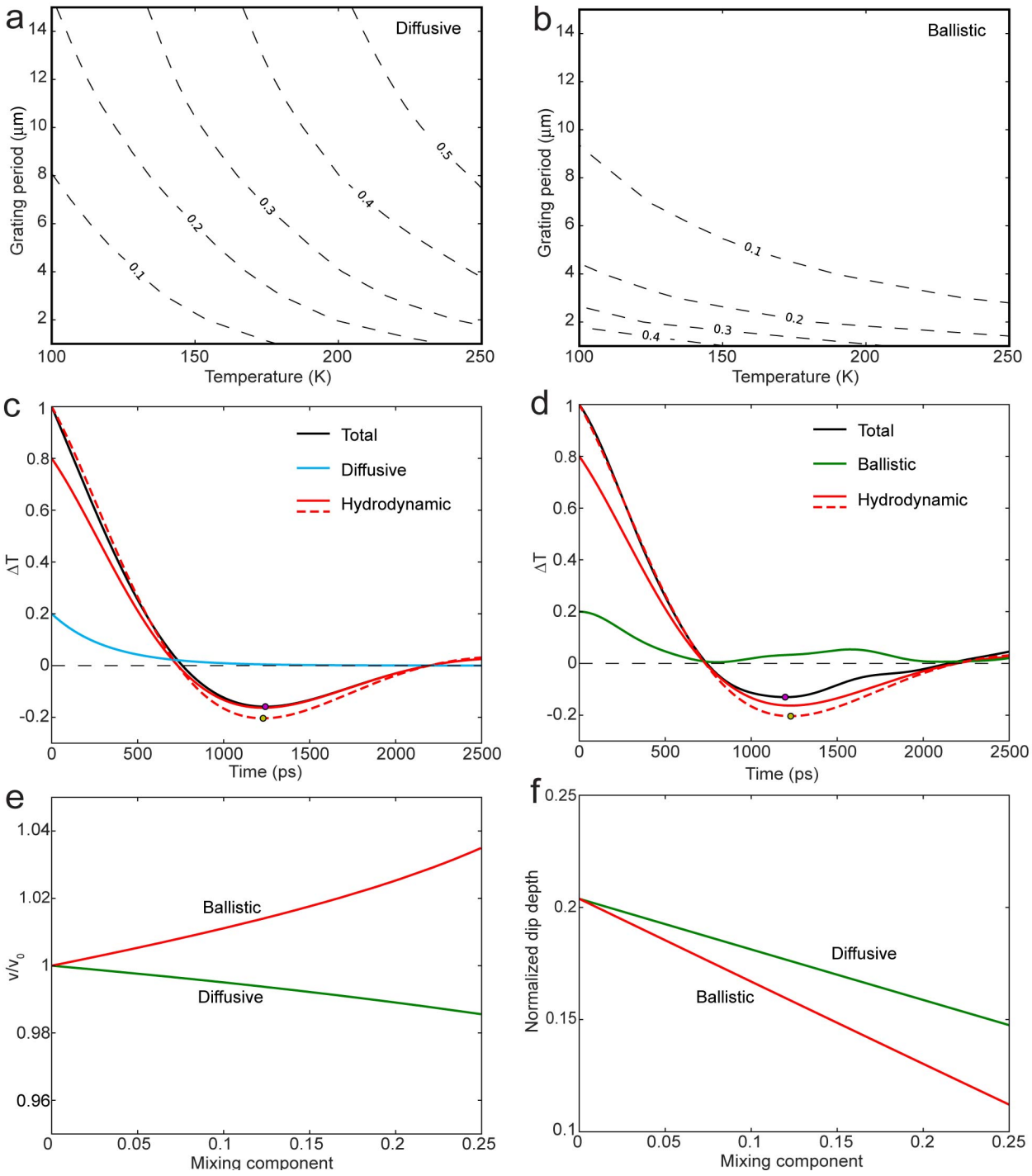

Figure 4-11 The "three-fluid" model. Fraction of excited phonons phonons in the (a) diffusion and (b) ballistic regime based on Eq. (4). (c) Superposition of contributions from hydrodynamic (80%) and diffusive phonons (20%). The dashed line is 100% hydrodynamic. Diffusion slows down the thermal wave and reduces its strength. (d) Superposition of hydrodynamic (80%) and ballistic phonons (20%). Ballistic phonons accelerate the thermal wave but also reduces its strength. The dots are the minima. (e) Wave propagation speed and (f) normalized dip depth for different fractions of diffusive and ballistic phonons. The TTG signals of diffusive, hydrodynamic, and ballistic phonons in (c)-(f) are all calculated for graphite at 125 K with a grating period of 10 μm

As the grating period decreases, more phonons go through the ballistic transport (Figure 4-11b), hence the wave propagation velocity increases from the bulk second sound velocity to the thermal zero sound velocity (Figure 4-6a). For the same reason, the second sound propagation length increases with longer grating period (Figure 4-6b), as more phonons participate in the second sound wave type of propagation rather than ballistic transport (Figure 4-11b). Velocity of the wavelike mode at fixed grating period monotonically decreases with increasing temperature (Figure 4-6a and Fig. S5a), as less phonons participate in ballistic transport at higher temperature due to increasing phonon scattering rates (Figure 4-11b). The second-sound strength, as measured by the normalized dip depth, is strongest at an intermediate grating spacing (Figure 4-6f). This can be understood as follows. When the spacing is large, R scattering dominates. The increased diffusive transport leads to smaller dip depth. When the spacing is small, ballistic phonons, which does not dip much below zero due to superposition of three different polarizations, mix with second sound waves and diminish the measured normalized dip depth. The thermal wave we observed on 200K mainly comes from second sound signals, which is supported by the large difference between the experimental signals and ballistic limit in Figure 4-2d.

4.5 Strong isotope effect

Large enhancements in the thermal conductivity via isotope enrichment has been reported in high-thermal conductivity materials[136]. Isotope scattering is a R-scattering process and can significantly influence second sound. Figure 4-12a and Figure 4-12b compares simulated wave propagation speed and propagation length in isotopically-enriched graphite with natural graphite. In isotopically enriched graphite, the propagation speed is more than 15% higher than natural graphite across all the grating period at 125 K and larger enhancement in the propagation length are observed. Moreover, in isotopically pure sample, our simulations indicate that we could observe second sound even at the room temperature at the grating period of 1.0 μm (Figure 4-12c) and 1.5 μm (Figure 4-12d). The smaller measured wave propagation speed (Figure 4-12a) in natural graphite than isotopically enriched graphite, could be understood as the increased contribution of diffusive phonons.

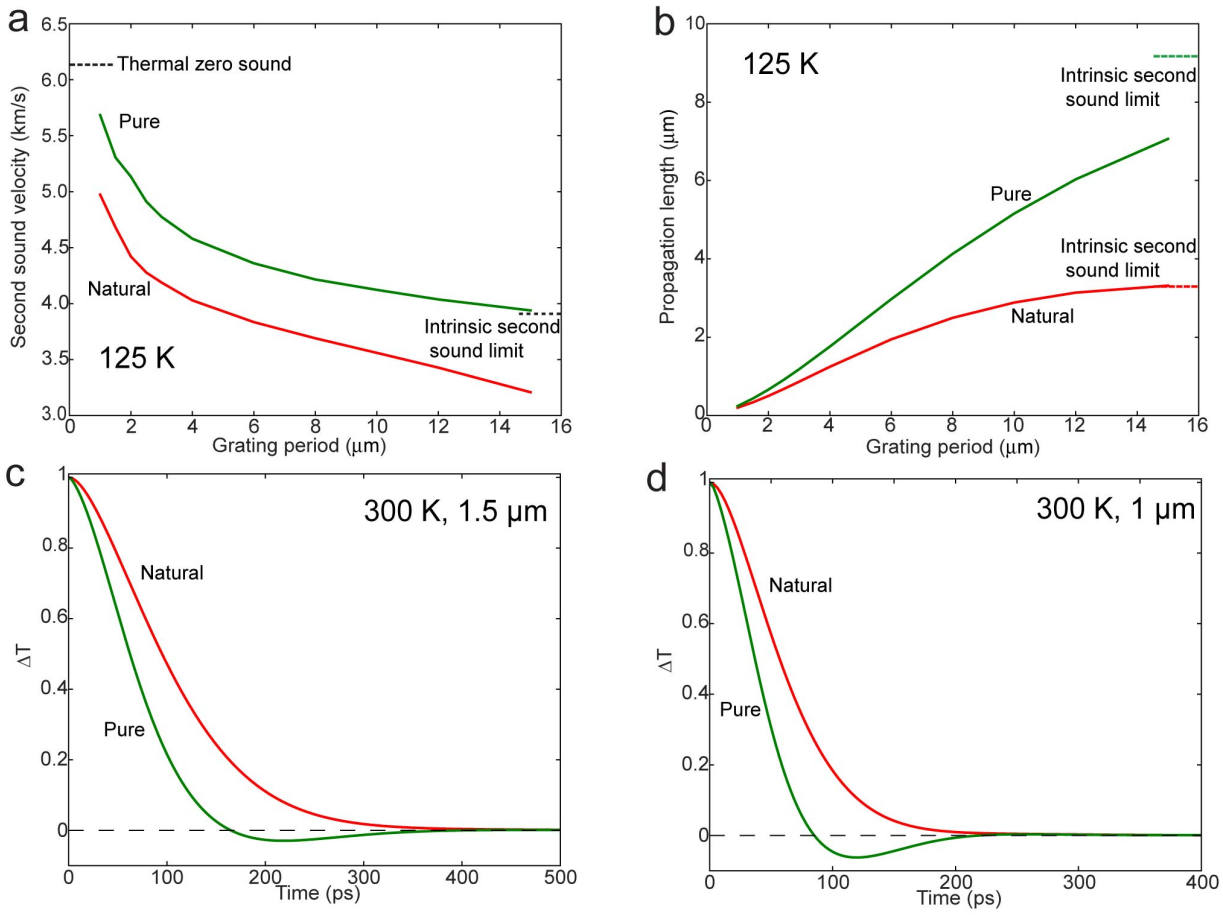

Figure 4-12 Isotope effect on second sound. Variation of (a) second sound velocity and (b) propagation length with grating period at 125 K in natural and isotopically pure graphite. TTG signal at 300 K with a grating period of (c) 1.5 μm and (d) 1 μm.

4.6 Discussion

The "three-fluids" picture degenerates into Fourier diffusion when diffusive phonons dominate. In the TTG experiment, thermal transport in the form the second sound when hydrodynamic phonons are dominant and in the thermal zero sound when the ballistic phonons are dominant. When the "three-fluids" co-exist, the wave propagation velocity increases with decreasing grating period because (1) the thermal zero sound makes more contribution at shorter grating period, and (2) the thermal zero sound velocity is faster than the intrinsic second sound velocity. The latter is guaranteed because second sound involves mixing of phonons via normal scattering process. For example, The TTG signal in the ballistic is given as Eq. (9). For a Debye material with sound

velocity v, where k is magnitude of wavevector. We replace the mode summation in Eq. (9) by integration, then the TTG signal can be written as:

$$\Delta T = sinc(qvt) \tag{4-21}$$

The time of the first dip t_d can be obtained the setting the derivative of the T to zeros, which gives:

$$qvt_d \approx 4.4934 \tag{4-22}$$

Substitute $q = \frac{2\pi}{l}$ into the above equation we obtain the thermal zero sound velocity as:

$$\mathrm{v_{tzs}} \approx 0.7\ v \tag{4-23}$$

Eq. 2a for a Debye material gives the intrinsic second sound velocity:

$$v_{ss} = \frac{v}{\sqrt{3}} \tag{4-24}$$

Therefore $\mathrm{v_{tzs}} > v_{ss}$ for a Debye material.

To summarize, we directly observe second sound in graphite above 200 K through TTG experiment. The TTG experiment signal also includes contributions of thermal zero sound: the propagation of ballistic phonon thermal waves. The experimental results can be explained by the

existence of “three-fluid” model: ballistic, diffusive, hydrodynamic phonons in solid. The measured wave propagation velocity increases with decreasing grating period due to increased influenced of the thermal zero sound. The experimental results in thermal wave dispersion and strength are in qualitative agreement with first-principles simulations. In isotopically pure graphite, we predict the observation of second sound even at room temperature, and largely enhanced measured wave propagation speed and propagation length.

Chapter 5 Summary and future directions

5.1 Summary and discussions

In this thesis, we have identified graphite as a good candidate material for phonon hydrodynamic transport by first-principles simulation. More specifically, we unambiguously revealed the Poiseuille heat flow and the existence of phonon Knudsen minimum in graphite by studying the variation of heat flow as the graphite ribbon width. A thorough microscopic explanation for the phonon Knudsen minimum is elaborated based on the concept of momentum-conserved scattering processes. In addition, by combining cutting-edge experiment with state-of-the-art theoretical framework, we confirmed the observation of second sound at a record-high temperature of over 200 K. In addition, with the enlarged grating-period window, we firstly reported the dispersion of thermal wave, whose velocity increases with decreasing grating period due to the increasing contribution of thermal zero sound—the thermal wave due to ballistic phonons.

The significant hydrodynamic nature of phonon transport in graphite is attributed to its strong intralayer sp^2 hybrid bonding and weak van der Waals interlayer interactions. The weak van der Waals interlayer interactions preserves the nearly diverging Grüneisen parameter and results in the strong scattering rates. On the other hand, the strong intralayer sp^2 hybrid bonding ensure high Debye temperature. As a result, most of the scattering process are N-scattering when studying in-plane transport.

5.2 Future directions

It is expected that our theory could be easily generalized to other layered system. The next system to explore is hexagonal Boron Nitride (hBN). Our preliminary calculation indicated the existence of second sound in hBN up to 125K, but it is hard to conduct experiments due to the weak absorption of hBN associated with the large bandgap. Similarly, it is expected that our analysis could be applied to 2D materials like graphene and 1D materials, like carbon nanotubes. However, it could be very challenging to do the measurements.

In addition to the layered system, our calculation also predicts the existence of the thermal waves in isotopically enriched diamond up to a temperature of 200K. Surprisingly, the gap between N-

scattering and U-scattering rate in diamond is not large. We suspected that this is another type of second sound as discussed by Hardy. [57] It is definitely a direction worth investigating.

Lastly, it remains unexplored how phonon hydrodynamic transport regime could be applied.

References

1. Peierls, R. E. *Quantum theory of solids*. (Oxford University Press, 1955).

2. Lee, S., Broido, D., Esfarjani, K. & Chen, G. Hydrodynamic phonon transport in suspended graphene. *Nat. Commun.* **6**, 6290 (2015).

3. Chen, G. *Nanoscale energy transport and conversion: a parallel treatment of electrons, molecules, phonons, and photons*. (Oxford University Press, 2005).

4. Lindsay, L., Broido, D. A. & Reinecke, T. L. Ab initio thermal transport in compound semiconductors. *Phys. Rev. B* **87**, 165201 (2013).

5. Esfarjani, K., Chen, G. & Stokes, H. T. Heat transport in silicon from first-principles calculations. *Phys. Rev. B* **84**, 085204 (2011).

6. Carrete, J. *et al.* almaBTE : A solver of the space–time dependent Boltzmann transport equation for phonons in structured materials. *Comput. Phys. Commun.* **220**, 351–362 (2017).

7. Ward, A., Broido, D. A., Stewart, D. A. & Deinzer, G. Ab initio theory of the lattice thermal conductivity in diamond. *Phys. Rev. B - Condens. Matter Mater. Phys.* **80**, 125203 (2009).

8. Callaway, J. Model for lattice thermal conductivity at low temperatures. *Phys. Rev.* **113**, 1046 (1959).

9. Krumhansl, J. A. Thermal conductivity of insulating crystals in the presence of normal processes. *Proc. Phys. Soc.* **85**, 921 (1965).

10. Cepellotti, A. *et al.* Phonon hydrodynamics in two-dimensional materials. *Nat. Commun.* **6**, 6400 (2015).

11. Lee, S. & Lindsay, L. Hydrodynamic phonon drift and second sound in a (20,20) single-wall carbon nanotube. *Phys. Rev. B* **95**, 184304 (2017).

12. Ding, Z. *et al.* Phonon Hydrodynamic Heat Conduction and Knudsen Minimum in Graphite. *Nano Lett.* **18**, 638–649 (2018).

13. Guo, Y. & Wang, M. Heat transport in two-dimensional materials by directly solving the

phonon Boltzmann equation under Callaway's dual relaxation model. *Phys. Rev. B* **96**, 134312 (2017).

14. Fugallo, G., Lazzeri, M., Paulatto, L. & Mauri, F. Ab initio variational approach for evaluating lattice thermal conductivity. *Phys. Rev. B* **88**, 045430 (2013).

15. Jones, R. O. Density functional theory: Its origins, rise to prominence, and future. *Rev. Mod. Phys.* **87**, 897 (2015).

16. Baroni, S., De Gironcoli, S., Corso, A. D. & Giannozzi, P. *Phonons and related crystal properties from density-functional perturbation theory*.

17. Li, W., Carrete, J., A. Katcho, N. & Mingo, N. ShengBTE: A solver of the Boltzmann transport equation for phonons. *Comput. Phys. Commun.* **185**, 1747–1758 (2014).

18. Kresse, G. & Furthmüller, J. Efficiency of ab-initio total energy calculations for metals and semiconductors using a plane-wave basis set. *Comput. Mater. Sci.* **6**, 15–50 (1996).

19. Kresse, G., Furthmüller, J. & Hafner, J. Ab initio force constant approach to phonon dispersion relations of diamond and graphite. *EPL (Europhysics Lett.* **32**, 729 (1995).

20. Kresse, G. & Joubert, D. From ultrasoft pseudopotentials to the projector augmented-wave method. *Phys. Rev. B* **59**, 1758 (1999).

21. Giannozzi, P. *et al.* QUANTUM ESPRESSO: a modular and open-source software project for quantum simulations of materials. *J. Phys. Condens. Matter* **21**, 395502 (2009).

22. Togo, A. & Tanaka, I. First principles phonon calculations in materials science. *Scr. Mater.* **108**, 1–5 (2015).

23. Parker, W. J., Jenkins, R. J., Butler, C. P. & Abbott, G. L. Flash method of determining thermal diffusivity, heat capacity, and thermal conductivity. *J. Appl. Phys.* **32**, 1679–1684 (1961).

24. Capinski, W. S. & Maris, H. J. Improved apparatus for picosecond pump-and-probe optical measurements. *Rev. Sci. Instrum.* **67**, 2720–2726 (1996).

25. Harata, A., Nishimura, H. & Sawada, T. Laser-induced surface acoustic waves and photothermal surface gratings generated by crossing two pulsed laser beams. *Appl. Phys.*

Lett. **57**, 132–134 (1990).

26. Pennington, D. M. & Harris, C. B. Dynamics of Photothermal Surface Expansion and Diffusivity Using Laser-Induced Holographic Gratings. *IEEE J. Quantum Electron.* **28**, 2523–2534 (1992).

27. Rogers, J. A., Yang, Y. & Nelson, K. A. Elastic modulus and in-plane thermal diffusivity measurements in thin polyimide films using symmetry-selective real-time impulsive stimulated thermal scattering. *Appl. Phys. A Solids Surfaces* **58**, 523–534 (1994).

28. Maznev, A. A., Nelson, K. A. & Rogers, J. A. Optical heterodyne detection of laser-induced gratings. *Opt. Lett.* **23**, 1319 (1998).

29. Goodno, G. D., Dadusc, G. & Miller, R. J. D. Ultrafast heterodyne-detected transient-grating spectroscopy using diffractive optics. *J. Opt. Soc. Am. B* **15**, 1791 (1998).

30. Johnson, J. A. *et al.* Phase-controlled, heterodyne laser-induced transient grating measurements of thermal transport properties in opaque material. *J. Appl. Phys.* **111**, (2012).

31. Peierls, V. R. Zur kinetischen Theorie der Warmerleitung in Kristallen. *Ann. Phys.* **395**, 1055–1101 (1929).

32. *Normal scattering process was named later by Callaway in Ref [8]*.

33. Maznev, A. A. & Wright, O. B. Demystifying umklapp vs normal scattering in lattice thermal conductivity. *Am. J. Phys.* **82**, 1062–1066 (2014).

34. Lou, L. *Introduction to phonons and electrons*. (World Scientific, 2003).

35. Zhang, Z. M. *Nano/microscale heat transfer*. (2007).

36. Ward, J. C. & Wilks, J. III. Second sound and the thermo-mechanical effect at very low temperatures. *London, Edinburgh, Dublin Philos. Mag. J. Sci.* **43**, 48–50 (1952).

37. Guyer, R. A. & Krumhansl, J. A. Thermal conductivity, second sound, and phonon hydrodynamic phenomena in nonmetallic crystals. *Phys. Rev.* **148**, 778–788 (1966).

38. Knudsen, M. Die Gesetze der Molekularstr??mung und der inneren Reibungsstr??mung der Gase durch R??hren. *Ann. Phys.* **333**, 75–130 (1909).

39. Mezhov-Deglin, L. P. Measurement of the thermal conductivity of crystalline He4. *Sov. Phys. JETP* **22**, 66–79 (1966).

40. Ranninger, J. Second sound in solids. *J. Phys. C Solid State Phys.* **2**, 929 (1969).

41. Jackson, H. E., Walker, C. T. & McNelly, T. F. Second sound in NaF. *Phys. Rev. Lett.* **25**, 26 (1970).

42. Ackerman, C. C., Bertman, B., Fairbank, H. A. & Guyer, R. A. Second sound in solid helium. *Phys. Rev. Lett.* **16**, 789–791 (1966).

43. Narayanamurti, V. & Dynes, R. C. Observation of second sound in bismuth. *Phys. Rev. Lett.* **28**, 1461–1465 (1972).

44. Pohl, D. W. & Irniger, V. Observation of Second Sound in NaF by Means of Light Scattering. *Phys. Rev. Lett.* **36**, 480–483 (1976).

45. Broido, D. A., Malorny, M., Birner, G., Mingo, N. & Stewart, D. A. Intrinsic lattice thermal conductivity of semiconductors from first principles. *Appl. Phys. Lett.* **91**, 1–3 (2007).

46. Klemens, P. G. Thermal conductivity of solids at low temperatures. *Handb. der Phys.* **14**, 198–281 (1956).

47. Bhatnagar, P. L., Gross, E. P. & Krook, M. A model for collision processes in gases. I. Small amplitude processes in charged and neutral one-component systems. *Phys. Rev.* **94**, 511–525 (1954).

48. Ma, J., Li, W. & Luo, X. Examining the Callaway model for lattice thermal conductivity. *Phys. Rev. B* **90**, 035203 (2014).

49. Martelli, V., Jiménez, J. L., Continentino, M., Baggio-Saitovitch, E. & Behnia, K. Thermal Transport and Phonon Hydrodynamics in Strontium Titanate. *Phys. Rev. Lett.* **120**, 125901 (2018).

50. Markov, M. *et al.* Hydrodynamic Heat Transport Regime in Bismuth: A Theoretical Viewpoint. *Phys. Rev. Lett.* **120**, 075901 (2018).

51. Shang, M.-Y. & Lü, J.-T. Nonlocal hydrodynamic phonon transport in two-dimensional materials. *arXiv:1803.08372* (2018).

52. Cepellotti, A. & Marzari, N. Transport Waves as Crystal Excitations. *Phys. Rev. Mater.* **1**, (2016).

53. Joseph, D. & Preziosi, L. Heat waves. *Rev. Mod. Phys.* **61**, 41–73 (1989).

54. Ackerman, C. C., Bertman, B., Fairbank, H. A. & Guyer, R. A. Second Sound in Solid Helium. *Phys. Rev. Lett.* **16**, 789–791 (1966).

55. McNelly, T. F. *et al.* Heat pulses in NaF: onset of second sound. *Phys. Rev. Lett.* **24**, 100 (1970).

56. Prohofsky, E. W. & Krumhansl, J. A. Second-Sound Propagation in Dielectric Solids. *Phys. Rev.* **133**, A1403 (1964).

57. Hardy, R. J. Phonon boltzmann equation and second sound in solids. *Phys. Rev. B* **2**, 1193–1207 (1970).

58. Hardy, R. J. Phonon boltzmann equation and second sound in solids. *Phys. Rev. B* **2**, 1193–1207 (1970).

59. Hardy, R. J. Phonon Boltzmann equation and second sound in solids. *Phys. Rev. B* **2**, 1193 (1970).

60. Li, W. & Mingo, N. Ultralow lattice thermal conductivity of the fully filled skutterudite YbFe 4 Sb 12 due to the flat avoided-crossing filler modes. *Phys. Rev. B* **91**, 144304 (2015) (2015).

61. Casimir, H. B. G. Note on the Conduction of Heat in Crystals. *Physica* **5**, 495–500 (1938).

62. Levitov, L. & Falkovich, G. Electron viscosity, current vortices and negative nonlocal resistance in graphene. *Nat Phys* **12**, 672–676 (2016).

63. Crossno, J. *et al.* Observation of the Dirac fluid and the breakdown of the Wiedemann-Franz law in graphene. *Science (80-.).* **10**, 1126 (2016).

64. Cao, C. *et al.* Universal Quantum Viscosity in a Unitary Fermi Gas. *Science (80-.).* **331**, 58–61 (2011).

65. Shuryak, E. Why does the quark-gluon plasma at RHIC behave as a nearly ideal fluid? *Prog.*

Part. Nucl. Phys. **53**, 273–303 (2004).

66. Dresselhaus, M. S. *et al.* New directions for low-dimensional thermoelectric materials. *Adv. Mater.* **19**, 1043–1053 (2007).

67. Cahill, D. G. *et al.* Nanoscale thermal transport. *J. Appl. Phys.* **93**, 793 (2003).

68. Cahill, D. G. *et al.* Nanoscale thermal transport. II. 2003–2012. *Appl. Phys. Rev.* **1**, 11305 (2014).

69. Hehlen, B., Pérou, A. L., Courtens, E. & Vacher, R. Observation of a doublet in the quasielastic central peak of quantum-paraelectric SrTiO3. *Phys. Rev. Lett.* **75**, 2416–2419 (1995).

70. Koreeda, A., Takano, R. & Saikan, S. Second sound in SrTiO3. *Phys. Rev. Lett.* **99**, (2007).

71. Khodusov, V. D. & Naumovets, A. S. Second sound waves in diamond. *Diam. Relat. Mater.* **21**, 92–98 (2012).

72. Zhou, Y., Zhang, X. & Hu, M. Nonmonotonic Diameter Dependence of Thermal Conductivity of Extremely Thin Si Nanowires: Competition between Hydrodynamic Phonon Flow and Boundary Scattering. *Nano Lett.* **17**, 1269–1276 (2017).

73. Guo, Y. & Wang, M. Phonon hydrodynamics and its applications in nanoscale heat transport. *Phys. Rep.* **595**, 1–44 (2015).

74. Cercignani, C. & Daneri, A. Flow of a rarefied gas between two parallel plates. *J. Appl. Phys.* **34**, 3509–3513 (1963).

75. Guo, H., Ilseven, E., Falkovich, G. & Levitov, L. S. Higher-Than-Ballistic Conduction of Viscous Electron Flows. *Proc. Natl. Acad. Sci.* **114**, 3068–3073 (2017).

76. Kumar, R. K. *et al.* Superballistic flow of viscous electron fluid through graphene constrictions. *Nat. Phys.* **10**, 1038 (2017).

77. Alam, M., Mahajan, A. & Shivanna, D. On Knudsen-minimum effect and temperature bimodality in a dilute granular Poiseuille flow. *J. Fluid Mech.* **782**, 99–126 (2015).

78. Gupta, R. & Alam, M. Hydrodynamics, wall-slip, and normal-stress differences in rarefied

granular Poiseuille flow. *Phys. Rev. E - Stat. Nonlinear, Soft Matter Phys.* **95**, 1–18 (2017).

79. Whitworth, R. W. Experiments on the Flow of Heat in Liquid Helium below 0.7K. *Proc. R. Soc. London A Math. Phys. Eng. Sci.* **246**, 390–405 (1958).

80. Moore, A. L. & Shi, L. Emerging challenges and materials for thermal management of electronics. *Mater. Today* **17**, 163–174 (2014).

81. Péraud, J.-P. M. *et al.* An alternative approach to efficient simulation of micro/nanoscale phonon transport. *Appl. Phys. Lett.* **101**, 153114 (2012).

82. Romano, G. & Grossman, J. C. Heat Conduction in Nanostructured Materials Predicted by Phonon Bulk Mean Free Path Distribution. *J. Heat Transfer* **137**, 071302 (2015).

83. Chiloyan, V. *et al.* Variational approach to solving the spectral Boltzmann transport equation in transient thermal grating for thin films. *J. Appl. Phys.* **120**, 1–19 (2016).

84. Jang, W., Chen, Z., Bao, W., Lau, C. N. & Dames, C. Thickness-Dependent Thermal Conductivity of Encased Graphene and Ultrathin Graphite. *Nano Lett.* **10**, 3909–3913 (2010).

85. Nika, D. L., Askerov, A. S. & Balandin, A. A. Anomalous Size Dependence of the Thermal Conductivity of Graphene Ribbons. *Nano Lett.* **12**, 3238–3244 (2012).

86. Allen, P. B. Improved Callaway model for lattice thermal conductivity. *Phys. Rev. B* **88**, (2013).

87. Fuchs, K. & Mott, N. F. The conductivity of thin metallic films according to the electron theory of metals. *Math. Proc. Cambridge Philos. Soc.* **34**, 100 (1938).

88. Sondheimer, E. H. The mean free path of electrons in metals. *Adv. Phys.* **1**, 1–42 (1952).

89. Cuffe, J. *et al.* Reconstructing phonon mean-free-path contributions to thermal conductivity using nanoscale membranes. *Phys. Rev. B* **91**, 245423 (2015).

90. Omini, M. & Sparavigna, a. An iterative approach to the phonon Boltzmann equation in the theory of thermal conductivity. *Phys. B Condens. Matter* **212**, 101–112 (1995).

91. Al Taleb, A. & Farías, D. Phonon dynamics of graphene on metals. *J. Phys. Condens.*

Matter **28**, 103005 (2016).

92. Ashcroft, N. W. & Mermin, N. D. *Solid state physics*. (Brooks Cole, 2005).

93. Ziman, J. M. *Electrons and phonons: the theory of transport phenomena in solids*. (Oxford University Press, 1960).

94. Gupta, A. K., Russin, T. J., Gutiérrez, H. R. & Eklund, P. C. Probing Graphene Edges. *ACS Nano* **3**, 45–52 (2009).

95. Kelly, K. F. & Billups, W. E. Synthesis of soluble graphite and graphene. *Acc. Chem. Res.* **46**, 4–13 (2013).

96. Mezhov-Deglin, L. P. Measurement of the thermal conductivity of crystalline He4. *J. Exp. Theor. Phys.* **49**, 66–79 (1965).

97. Gurzhi, R. N. & Shevchenko, S. I. CONTRIBUTION TO THE THEORY OF THE THERMAL CONDUCTIVITY OF DIELECTRIC. *Zh. Eksp. Teor. Fiz.* **27**, 863–864 (1968).

98. Gurzhi, R. N. Thermal conductivity of dielectrics and ferrodielectrics at low temperatures. *J. Exp. Theor. Phys.* **46**, 719–724 (1964).

99. Samsonov, G. V. *Handbook of the Physicochemical Properties of the Elements*. (2012).

100. Bae, M.-H. *et al.* Ballistic to diffusive crossover of heat flow in graphene ribbons. *Nat. Commun.* **4**, 1734 (2013).

101. Lindsay, L., Broido, D. A. & Reinecke, T. L. Phonon-isotope scattering and thermal conductivity in materials with a large isotope effect: A first-principles study. *Phys. Rev. B* **8815**, (2013).

102. Lindsay, L., Broido, D. A. & Mingo, N. Flexural phonons and thermal transport in multilayer graphene and graphite. *Phys. Rev. B - Condens. Matter Mater. Phys.* **83**, 1–5 (2011).

103. Maultzsch, J., Reich, S., Thomsen, C., Requardt, H. & Ordejón, P. Phonon Dispersion in Graphite. *Phys. Rev. Lett.* **92**, (2004).

104. Mohr, M. *et al.* Phonon dispersion of graphite by inelastic x-ray scattering. *Phys. Rev. B* **76**, (2007).

105. Nicklow, R., Wakabayashi, N. & Smith, H. G. Lattice dynamics of pyrolytic graphite. *Phys. Rev. B* **5**, 4951 (1972).

106. Pop, E. Energy dissipation and transport in nanoscale devices. *Nano Res.* **3**, 147–169 (2010).

107. Johnson, J. A. *et al.* Direct Measurement of Room-Temperature Nondiffusive Thermal Transport Over Micron Distances in a Silicon Membrane. doi:10.1103/PhysRevLett.110.025901

108. Sham, L. J. Equilibrium approach to second sound in solids. *Phys. Rev.* **156**, 494–500 (1967).

109. Guyer, R. A. & Krumhansl, J. A. *Dispersion relation for second sound in solids*. *Physical Review* **133**, (1964).

110. Enz, C. P. One-particle densities, thermal propagation, and second sound in dielectric crystals. *Ann. Phys. (N. Y).* **46**, 114–173 (1968).

111. Sulpizio, J. A. *et al.* Visualizing Poiseuille flow of hydrodynamic electrons. *Nature* **576**, 75 (2019).

112. Bandurin, D. A. *et al.* Negative local resistance caused by viscous electron backflow in graphene. *Science (80-.).* **351**, 1055–1058 (2016).

113. Moll, P. J. W., Kushwaha, P., Nandi, N., Schmidt, B. & Mackenzie, A. P. Evidence for hydrodynamic electron flow in PdCoO2. *Science (80-.).* **351**, 1061 LP – 1064 (2016).

114. Cepellotti, A. *et al.* Phonon hydrodynamics in two-dimensional materials. *Nat. Commun.* **6**, 1–7 (2015).

115. Scuracchio, P., Michel, K. H. & Peeters, F. M. Phonon hydrodynamics, thermal conductivity, and second sound in two-dimensional crystals. *Phys. Rev. B* **99**, 144303 (2019).

116. Huberman, S. *et al.* Observation of second sound in graphite at temperatures above 100 K. *Science (80-.).* **364**, 375–379 (2019).

117. Machida, Y. *et al.* Observation of poiseuille flow of phonons in black phosphorus. *Sci. Adv.* **4**, eaat3374 (2018).

118. Joseph, D. D. & Preziosi, L. Heat waves. *Rev. Mod. Phys.* **61**, 41–73 (1989).

119. Peshkov, V. 'Second sound' in Helium II. *J. Phys. Moscow* **8**, 131 (1944).

120. Landau, L. Theory of the superfluidity of helium II. *Phys. Rev.* **60**, 356–358 (1941).

121. Narayanamurti, V. & Dynes, R. C. Observation of second sound in bismuth. *Phys. Rev. Lett.* **28**, 1461–1465 (1972).

122. Jackson, H. E., Walker, C. T. & McNelly, T. F. Second sound in NaF. *Phys. Rev. Lett.* **25**, 26–28 (1970).

123. Sham, L. J. Temperature Propagation in Anharmonic Solids. *Phys. Rev.* **163**, 401 (1967).

124. Landau, L. & Rumer, G. Absorption of sound in solids. *Phys. Z. Sowjetunion* **11**, (1937).

125. Akhiezer, A. On the sound absorption in solids. *J. Phys. (USSR),* (1939).

126. Landau, L. D. Oscillations in a Fermi liquid. *Sov. Phys. JETP-USSR* **5**, 101–108 (1957).

127. Pethick, C. J. Attenuation of Zero Sound in a Normal Fermi Liquid. *Phys. Rev.* **185**, 384–392 (1969).

128. Beck, H., Meier, P. F. & Thellung, A. Phonon hydrodynamics in solids. *physica status solidi (a)* **24**, 11–63 (1974).

129. Cowley, R. A. *Zero sound, first sound and second sound of solids*. (1967).

130. Collins, K. C. *et al.* Non-diffusive relaxation of a transient thermal grating analyzed with the Boltzmann transport equation. *J. Appl. Phys* **114**, 104302 (2013).

131. Khalil, M., Golonzka, O., Demirdöven, N. & Tokmakoff, A. Phase-sensitive detection for polarization-selective femtosecond Raman spectroscopy. *Springer Ser. Chem. Phys.* **66**, 545–547 (2001).

132. Chen, K. *et al.* Measurement of Ambipolar Diffusion Coefficient of Photoexcited Carriers with Ultrafast Reflective Grating-Imaging Technique. *ACS Photonics* **4**, 1440–1446 (2017).

133. Chiloyan, V. *et al.* Micro/nanoscale thermal transport by phonons beyond the relaxation time approximation: Green's function with the full scattering matrix. *arXiv Prepr. arXiv1711.07151* (2017).

134. Ding, Z. *et al.* Umklapp scattering is not necessarily resistive. *Phys. Rev. B* **98**, 1–6 (2018).

135. Dreyer, W. & Struchtrup, H. Heat pulse experiments revisited. *Contin. Mech. Thermodyn.* **5**, 3–50 (1993).

136. Chen, K. *et al.* Ultrahigh thermal conductivity in isotope-enriched cubic boron nitride. *Science (80-.).* **367**, 555–559 (2020).